A Method for the Estimation of f- and p-Mode Parameters and Rotational Splitting Coefficients from Un-averaged Solar Oscillation Power Spectra

J. Reiter[1]

E. J. Rhodes, Jr.[2,3]

A. G. Kosovichev[4]

P. H. Scherrer,[5] T. P. Larson,[5] and S. F. Pinkerton II[2]

[1]*Zentrum Mathematik, M17*
Technische Universität München
D-85748 Garching bei München, Germany
[2]*Department of Physics and Astronomy*
University of Southern California
Los Angeles, CA 90089-1342, USA
[3]*Astrophysics and Space Sciences Section, Jet Propulsion Laboratory*
California Institute of Technology
4800 Oak Grove Dr.
Pasadena, CA 91109-8099, USA
[4]*New Jersey Institute of Technology*
Newark, NJ 07103, USA
[5]*W. W. Hansen Experimental Physics Laboratory*
Stanford University
Stanford, CA 94305-4085, USA

ABSTRACT

We present a new methodology for the fitting of the peaks in solar oscillation power spectra that is equally well-suited for the estimation of low-, medium, and high-degree f- and p-mode parameters and frequency-splitting coefficients. The method can provide accurate input data over a wide portion of the dispersion plane for both structural and rotational inversions. This method, which we call the Multiple-Peak, Tesseral-Spectrum (MPTS) method, operates directly upon of all the modes in a multiplet (n, l) of radial order n and degree l, and employs a fitting profile that consists of the sum of numerous individual overlapping profiles whose relative amplitudes are determined by the leakage matrix appropriate to the targeted mode. Hence, $2l + 1$ sets of modal parameters are

Corresponding author: J. Reiter
jreiter@lrz.tum.de

obtained simultaneously for each multiplet (n, l). By fitting an appropriate polynomial to the run of the fitted frequencies versus the azimuthal order, frequency-splitting coefficients are also obtained for the same multiplet. Using power spectra obtained from the 66-day long 2010 MDI Dynamics Run, we present sample structural and rotational inversions that employed frequencies and frequency-splitting coefficients from modes in the degree range of 0 to 1000 and the frequency range of 965 to 4600 μHz. The structural inversion confirms evidence for a pronounced departure of the sound speed in the outer solar convection zone from the radial sound speed profile contained in Model S of Christensen-Dalsgaard and his collaborators that we (Reiter et al. 2015) obtained previously using a different fitting method.

Keywords: Sun: helioseismology — Sun: oscillations — methods: data analysis — methods: numerical

1. INTRODUCTION

Since the discovery of the five-minute oscillations of the Sun by Leighton et al. (1962) and the advent of helioseismology with the first measurement of the depth of the solar convection zone by Gough (1977) and independently by Rhodes et al. (1977), our knowledge of the structure and dynamics of the solar interior has been virtually revolutionized. A major reason for this is the possibility of performing numerical inversions of different properties of the solar f- and p-mode oscillations. In terms of global helioseismology such inversions are of two types: 1) structural inversions employing tables of the frequencies of f- and p-mode oscillations and their associated uncertainties to infer the structure and dynamics of the solar interior; 2) rotational inversions employing tables of the frequency splittings of the modes of different azimuthal order to measure the internal angular velocity as functions of radius and latitude, and to provide the aspherical components of the solar structure.

Using observations over the visible solar disk individual modes cannot be uniquely isolated, because the spherical harmonics are only orthogonal over the full sphere. Hence, no spatial filtering will uniquely isolate a targeted mode, resulting in what is known as spatial leakage. In the frequency domain, at low and intermediate degrees, these spatial leaks are well separated from the targeted mode. Thus, individual modes can be identified and fitted, provided a sound theoretical profile is available. At high degrees, however, the spatial leaks get closer in frequency due to a smaller mode separation, and as the mode lifetimes get smaller, the resulting peaks get wider and eventually overlap. As a result, high-degree modes blend into broad ridges of power. Unfortunately, the properties of such ridges do not correspond to those of the underlying spectral peaks. This is because the amplitudes of the spatial leaks are asymmetrical with respect to the targeted mode, whereby the central frequency of the ridge is significantly shifted away from the true mode frequency. Therefore, the fitting of a ridge requires detailed knowledge of the amount of power which leaks into the sidelobes that are adjacent to the true spectral peak.

Libbrecht & Kaufman (1988) were the first to publish estimates of high-degree mode frequencies, using solar oscillation spectra that were averaged over their azimuthal order m. To recover the underlying mode frequency from fitting the ridge of power of a given mode, they used a multiple-linear-regression technique to correct the ridge-fit frequency for the inherent uncertainty in the image

scale of their observational equipment and for the variations in the observed power density as a function of degree l which were caused by both instrumental and solar effects.

Improving the method of Libbrecht & Kaufman (1988) but following the same idea, Korzennik (1990) and Rhodes et al. (1998) also estimated high-degree mode frequencies. Bachmann et al. (1995), however, calculated an approximation to the radial component of the m-averaged leakage matrix instead of using a Gaussian profile approximation to model the amplitude of the peaks that contribute to the ridge power distribution.

In the Global Oscillations Network Group (GONG) project (Harvey et al. 1996), one spectrum of given l and m is fitted at a time under the assumption that it is a superposition of Lorentzian peaks, in order to get a separate frequency for each n, l, m, where n is the radial order of the mode. However, this approach is not appropriate for the cases in which the observed power has the appearance of a broad ridge. Hence, this method has not been applied for modes with $l > 150$. For more details we refer to Hill et al. (1996).

In the mean-multiplet technique of Schou (1992) a maximum likelihood method is employed to simultaneously fit an asymmetrical profile to the power spectral peaks in all of the $2l + 1$ individual power spectra for each multiplet. Although this approach allows to take into account the effects of overlapping peaks, it is inappropriate for ridge fitting. The $2l + 1$ frequencies are then averaged to yield a single frequency, $\nu_{n,l}$, for that multiplet. For more details we refer to Section 5.2.

The basic idea of the fitting methodology of Korzennik et al. (2004) consists of correcting for the bias introduced when fitting a ridge of power at high degrees. For this purpose, a detailed model of the underlying modes that contribute to the distribution of power in a ridge was developed to generate synthetic ridges, which are then fitted using the same methodology employed to fit the observations. Hence, from fitting these synthetic data a measure of the bias between the ridge properties and those of the underlying targeted mode used in the modeling can be derived. By means of this measure the results from fitting an observed ridge can be corrected to yield the unbiased properties of the underlying targeted mode. For further details we refer to Section 5.3.

Our attempts to measure high-degree mode parameters have a long tradition dating back to the late 1980s with the development of our first-generation, or single-peak, averaged-spectrum fitting method (see Appendix A in Reiter et al. (2015)). This method, which used a similar approach as the method of Libbrecht & Kaufman (1988), had to be abandoned, however, because of insurmountable problems with the determination of unbiased ridge-fit frequencies. Therefore, we began to develop our second-generation, or Windowed, MuLTiple-Peak, averaged-spectrum fitting method, which we will refer to in the following as WMLTP method (Reiter et al. (2015), hereafter referred to as Paper I). In this method a theoretical fitting profile is used which is constructed by convolving the weighted sum of the profiles of the modes appearing in the fitting box with the power spectrum of the window function of the observing run, using weights from a suitable leakage matrix.

Soon after the beginning of the development of the WMLTP method, there were doubts as to whether it would be possible at all to calculate unbiased frequency-splitting coefficients for the conversion of the un-averaged spectra into sets of m-averaged power spectra which are an indispensable ingredient of the WMLTP method. Our doubts were based on the fact that the odd frequency-splitting coefficients appeared to undergo jumps or offsets in the intermediate-degree range. These discontinuities were first noticed by Korzennik (1990) and later by Rhodes et al. (1998) in attempts to generate frequency-splitting coefficients employing the cross-correlation method of Brown (1985)

and Tomczyk (1988). Most often, mode-blending effects were blamed for causing these jumps. This issue motivated us to develop our third-generation, or Multiple-Peak, Tesseral-Spectrum method, which is the topic of this paper, and which we will refer to in the following as MPTS method. In contrast to the WMLTP method, the MPTS method operates directly on the un-averaged spectra, so that the calculation of the m-averaged power spectra is no longer necessary.

Unfortunately, the results obtained from an early version of the MPTS method showed similar jumps in the frequency-splitting coefficients and, moreover, also in the mean-multiplet frequencies, for a range of intermediate degrees (cf. Figures 6 and 7 of Reiter et al. (2002)). On the other hand, in a preprint (later published as Korzennik et al. (2004)) which was first circulated during mid-2002, S. Korzennik, J. Schou, and C. Rabello-Soares called attention to the paper by Woodard (1989) in which he had pointed out that the latitudinal variation in the solar angular velocity known as differential rotation introduces distortions into the p-mode eigenfunctions which affect the frequency-splitting coefficients in the intermediate-degree range. Applying Woodard's theory, we found that taking into account this effect in the leakage matrix had a very dramatic impact upon the resulting frequency-splitting coefficients as well as upon the mean-multiplet frequencies (cf. Figures 1 and 2 in Reiter et al. (2003)).

The delay between the publication of our early WMLTP results in Rhodes et al. (2001) and the Reiter et al. (2015) paper which describes that method in detail, and the delay between the publication of the preliminary MPTS results in Reiter et al. (2002, 2003) and the publication of the present paper is explained by the fact that we spent much time implementing major improvements into both the WMLTP and the MPTS method. However, working on both methods in parallel seemed to be amply justified by the fact that both methods are complementary to each other. While the WMLTP method is particularly suited for the fitting of m-averaged power spectra derived from observing runs as short as three days as well as for the fitting of pseudo-mode ridges with frequencies up to $7000\,\mu$Hz, this is not the case for the MPTS method, because: 1) un-averaged power spectra that are derived from observational time series that are as short as three days will have a low S/N for all frequencies, and 2) un-averaged power spectra that are derived from longer time series, such as the 66-day duration of the 2010 Dynamics Run (Scherrer et al. 1995) of the Michelson Doppler Imager (MDI) (Scherrer et al. 1995) on-board the Solar and Heliospheric Observatory (SOHO) (Domingo et al. 1995) that we are using in this paper will have a low S/N for frequencies greater than $5000\,\mu$Hz. On the other hand, both the WMLTP and the MPTS method have the common property that they can be applied equally to low-, intermediate, and high-degree modes. Therefore, we are now in a position to process an observing run with one single method of our choice. In this way, systematic errors are avoided which usually arise if the results of two or more techniques are combined.

The present paper is organized as follows. After a description of the origin of the data used in Section 2, we discuss in Section 3 the details and the mode of operation of the MPTS method, before we show a wide range of sample results from the MPTS method in Section 4. Also in Section 4, we present an extensive analysis of the influence of the leakage matrices upon the multiplet structure of the f- and p-mode parameters. In Section 5 we present a detailed comparison of results obtained from the MPTS method, the WMLTP method, and from the fitting methodologies of Schou (1992) and Korzennik et al. (2004). In Sections 6 and 7 we present helioseismic inversions for solar structure and rotation, respectively, which are based upon results obtained from the MPTS method. Our concluding remarks are given in Section 8.

2. DATA

The results presented in this paper are based upon a set of un-averaged power spectra that were created from a 66-day time series of full-disk Dopplergrams which were acquired during the 2010 Dynamics Run of the MDI on-board the SOHO spacecraft. This run, which we will refer to in the following as the $\mathcal{R}2010\_66$ observing run, started May 7, 2010, and ended July 11, 2010. For the details of the conversion of the time series of Dopplergrams into a set of power spectra we refer to Section 2.1 of Paper I.

3. THE MULTIPLE-PEAK, TESSERAL SPECTRUM (MPTS) METHOD

The MPTS method operates directly upon of all the modes in a multiplet (n, l). As a result, $2l + 1$ sets of modal parameters are obtained simultaneously for that multiplet (n, l). By simply averaging all of the $2l + 1$ frequency estimates within a multiplet, we can then obtain an average frequency for that multiplet, which is called the "mean-multiplet frequency". In addition, by fitting an appropriate polynomial to the run of the fitted frequencies versus m, we are also able to estimate the frequency-splitting coefficients for that multiplet. Since the errors in the sectoral, tesseral, and zonal power spectra are not normally distributed as they are in the case of the m-averaged spectra (at least for $l \gg 1$), we have chosen to employ a maximum-likelihood fitting approach in the MPTS method.

3.1. *Theoretical fitting profile*

In the MPTS method the following fitting profile is employed to represent an oscillation peak of l, m, and n, viz.

$$
M_{n,l,m}(\nu, \boldsymbol{p}) = \underbrace{\sum_{l',m'} C^{\mathrm{(ps)}}_{n;l,m;l',m'} \Psi(A_{l',m'}, \nu_{l',m'}, w_{l',m'}, B_{l',m'}, \nu)}_{\text{targeted peak including } l\text{- and } m\text{-leaks}}
$$
$$
+ \underbrace{\sum_{i=1}^{N} \Psi(A_i, \nu_i, w_i, B_i, \nu)}_{n\text{-leaks}} + \underbrace{a + b\,\nu + c\,\nu^2}_{\text{background}} . \tag{1}
$$

Here, ν is frequency, $\boldsymbol{p}$ is the fitting vector (see below), $C^{\mathrm{(ps)}}_{n;l,m;l',m'}$ is the leakage matrix relevant to a power spectrum as defined in Equation (11) of Paper I, Ψ is the asymmetrical profile of Nigam & Kosovichev (1998), i.e.

$$
\Psi(A_{l,m}, \nu_{l,m}, w_{l,m}, B_{l,m}, \nu) = A_{l,m}\,\frac{(1 + B_{l,m}x)^2 + B_{l,m}^2}{1 + x^2}, \quad x = \frac{2\,(\nu - \nu_{l,m})}{w_{l,m}}, \tag{2}
$$

where $A_{l,m}$, $\nu_{l,m}$, $w_{l,m}$, $B_{l,m}$ denote, respectively, the amplitude, frequency, line width, and line asymmetry of a mode of degree l and azimuthal order m; N is the number of n-leaks that fall within a pre-determined range of frequencies that we refer to as the fitting box that surrounds the target mode; A_i, ν_i, w_i and B_i are, respectively, the amplitude, the frequency, the line width, and the line asymmetry of the i-th n-leak; and a, b, c are background noise parameters. We will discuss the procedure for determining the widths of the fitting boxes in Section 3.2. In Equation (1) the summation has been split into a sum over l', m' (for the l- and m-leaks) and over i (for the

n-leaks) because the n-leaks have by definition radial orders different from n, while the l- and m-leaks have radial order n throughout. We note that the leakage matrix $C^{(\mathrm{ps})}_{n;l,m;l',m'}$ in Equation (1) is corrected, according to the theory of Woodard (1989) (see Section 3.2.2 of Paper I), for the distortion that is caused by the solar differential rotation. The summation in Equation (1) over l', m' is performed in the ranges $|l - l'| \leq N_l$ and $|m - m'| \leq N_m$, respectively, where N_l and N_m are suitably chosen numbers. While in the summation for the f-modes all of the modes are included in order to improve the quality of the fits, it suffices for the p-modes to only include those modes for which $C^{(\mathrm{ps})}_{n;l,m;l',m'} > \tau_{\mathrm{TH}} \max_{l',m'} C^{(\mathrm{ps})}_{n;l,m;l',m'}$, where $\tau_{\mathrm{TH}} = 5 \cdot 10^{-5}$. In this way, the computational burden of the MPTS method is lowered considerably. Because for high-degree modes the leakage matrix is getting rather wide (see Figure 3 in Paper I), which is mainly due to the distortion of the oscillation eigenfunctions caused by the solar differential rotation, we have adopted for our applications $N_l = N_m = 30$ throughout.

So far, the temporal window function of the observing run is not included in the model profile, as given in Equation (1). Hence, with the current version of the MPTS code only observing runs having a sufficiently high duty cycle can be processed in a meaningful manner. For data obtained from either the MDI or the Helioseismic and Magnetic Imager (HMI) instrument (Scherrer et al. 2012) on-board the Solar Dynamics Observatory (SDO) (Pesnell et al. 2012) this is definitely the case.

Presuming that the leakage matrix $C^{(\mathrm{ps})}_{n;l,m;l',m'}$ is known, we see from Equation (1) that the fitting profile is characterized by the following unknown parameters:

$$A_{l',m'},\ \nu_{l',m'},\ w_{l',m'},\ B_{l',m'},\ A_i,\ \nu_i,\ w_i,\ B_i,\ a,\ b,\ c. \tag{3}$$

Here, the indices l', m', and i are allowed to vary in the following ranges:

$$l' = l - N_l,\ l - N_l + 1,\ \ldots l - 1,\ l,\ l + 1,\ \ldots l + N_l, \tag{4}$$

$$m' = m - N_m,\ m - N_m + 1,\ \ldots m - 1,\ m,\ m + 1,\ \ldots m + N_m, \tag{5}$$

$$i = 1,\ \ldots N. \tag{6}$$

Because in Equations (4) and (5) the restrictions $l' \geq 0$ and $|m'| \leq l'$ must be fulfilled, there are at most a total of

$$N_{\mathrm{tot}} = 4\,(2N_l + 1)\,(2N_m + 1) + 4N + 3 \tag{7}$$

unknowns.

For the determination of the N_{tot} unknown parameters we proceed as follows. Except for the targeted mode (l, m), we take in the sum over l', m' in Equation (1) the parameters $A_{l',m'}$, $\nu_{l',m'}$, $w_{l',m'}$, $B_{l',m'}$ from tables containing initial estimates (seeds) of them that were derived from previously computed modal parameters. These seed values were improved upon in a fixed-point iteration similar to that described in Reiter et al. (2015). We refer to the iterative compilation of such seed tables as the external fixed-point iteration (cf. Section 3.6). While the $4\,(2N_l + 1)\,(2N_m + 1) - 4$ parameters that are taken from seed tables can be assumed to be known in an iteration step of the external fixed-point iteration, we lump together the remaining $4N + 7$ unknown parameters in the fitting vector

$$\boldsymbol{p} = (A_{l,m}, \nu_{l,m}, w_{l,m}, B_{l,m}, A_1, \nu_1, w_1, B_1, \ldots, A_N, \nu_N, w_N, B_N, a, b, c)^{\mathrm{T}}, \tag{8}$$

which is determined in another fixed-point iteration that is, however, directly incorporated into the MPTS code, and which we refer to as the inner fixed-point iteration.

In the early version of the MPTS method (Reiter et al. 2002, 2003) the parameters $A_{l',m'}$, $\nu_{l',m'}$, $w_{l',m'}$, $B_{l',m'}$ were not taken from tables, but rather were expressed in the form of first-order Taylor series expansions in the two variables l' and m', centered at l and m of the targeted mode, by considering both the degree and the azimuthal order as continuous variables. The necessary derivatives with respect to l were determined in an external fixed-point iteration, while the derivatives with respect to m were determined in an inner fixed-point iteration. Moreover, variations of both line width and line asymmetry with l and m were ignored. This approach had to be abandoned, however, because higher-order Taylor series expansions would have been necessary in order to adequately deal with the wide leakage matrices for high-degree modes, while on the other hand it was unclear how the higher-order derivatives which are then required could be calculated.

3.2. *Selection of fitting box widths*

In principle, it would be desirable to fit all ridges simultaneously that are present in an un-averaged spectrum of given l and m. However, we believe that such an approach is difficult to implement on practical grounds, especially for the high-degree modes. Therefore, we are confronted with the problem of how to select a suitable fitting box around the targeted mode (n, l, m). Without having to emphasize it, the width of the selected fitting box is crucial for the successful determination of the fitting vector $\boldsymbol{p}$ defined in Equation (8). On the one hand, the fitting box must be sufficiently wide so that both the mode profile and the background power are well sampled. On the other hand, the fitting box must not be unduly wide in order to keep the computational burden low, which increases in a non-linear manner with the number of frequency bins comprising the fitting box.

We found it useful to choose the frequency boundaries of the fitting box for the zonal mode of radial order n and degree l according to

$$\nu_{n,l}^{\text{low}} = \nu_{n,l}^{\text{seed}} - h_{n,l}, \tag{9}$$

$$\nu_{n,l}^{\text{up}} = \nu_{n,l}^{\text{seed}} + h_{n,l}, \tag{10}$$

and to also use the so defined fitting box for the tesseral and sectoral spectra by shifting its boundaries appropriately to allow for solar rotation and asphericity. Here, $\nu_{n,l}^{\text{seed}}$ is the seed frequency of the targeted multiplet (n, l), $\nu_{n,l}^{\text{low}}$ and $\nu_{n,l}^{\text{up}}$ are the lower and upper frequency boundary, respectively, of the fitting box, and $h_{n,l}$ is half of the width of the fitting box, and is given by

$$h_{n,l} = h_n^{\text{left}} (1 - z) + h_n^{\text{right}} z, \quad z = C\big((l - l_0)/\Lambda_n\big). \tag{11}$$

Here, h_n^{left}, h_n^{right}, l_0, and Λ_n are predetermined parameters depending on n, and $C(x)$ is the standard normal cumulative distribution function, i.e.

$$C(x) = \frac{1}{\sqrt{2\pi}} \int_{-\infty}^{x} \exp\big(-u^2/2\big)\, \mathrm{d}u = \frac{1}{2}\left[1 + \operatorname{erf}\left(\frac{x}{\sqrt{2}}\right)\right], \tag{12}$$

where erf denotes the error function. The parameters h_n^{left}, h_n^{right}, l_0, and Λ_n were all determined in a trial-and-error process that consisted of the generation and inspection of a large number of power spectral plots that allowed us to ensure that all of the relevant peaks fell within each of the fitting boxes. The frequency shift required for the use of the zonal fitting box in the tesseral and

sectoral spectra is computed from the frequency-splitting coefficients (cf. Section 3.5) of the targeted multiplet (n, l) that are taken from a seed table. Because of the characteristics of the function $C(x)$, we have for degrees l

$$l \lesssim l_0 - 3.5\Lambda_n: \quad h_{n,l} \approx h_n^{\text{left}}, \tag{13}$$

$$l \gtrsim l_0 + 3.5\Lambda_n: \quad h_{n.l} \approx h_n^{\text{right}}, \tag{14}$$

and a smooth transition of $h_{n,l}$ from h_n^{left} to h_n^{right}. We note that this transition is symmetrical around degree l_0. In practice, we determine for a given radial order n the parameters h_n^{left}, h_n^{right}, l_0, and Λ_n by eyeball inspection, trying to meet the above given general criteria that a fitting box should comply with. For a selected set of radial orders n, we show in Figure 1 the half of the width of the respective fitting boxes measured in terms of the variation of the mode frequency with respect to n, $\Delta\nu/\Delta n$, as a function of degree.
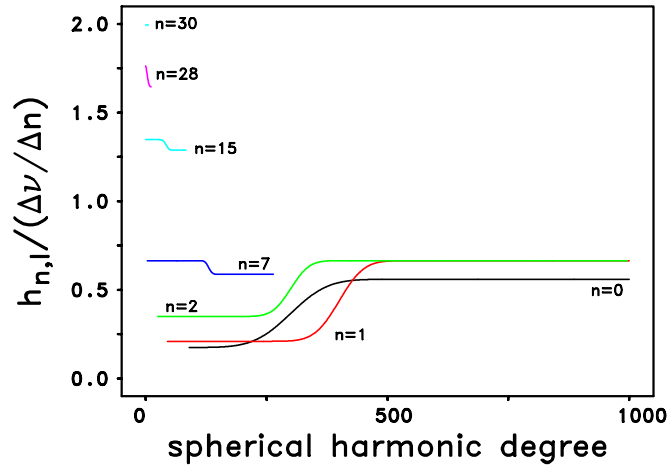
Figure 1. Half of the width, $h_{n,l}$, of the fitting box, measured in terms of $\Delta\nu/\Delta n$, versus degree for a selected set of radial orders n. Here, $\Delta\nu/\Delta n$ denotes the variation of the mode frequency with respect to n. Only for the higher-order ridges $n \geq 15$ are the n-leaks $(n \pm 1, l)$ included in the fitting box. We also note that the $n = 30$ ridge comprises the degrees from $l = 0$ to $l = 5$ only. The curves for the $n = 8$ through $n = 14$ ridges all fell just below and to the left of the $n = 7$ curve. They were very closely-spaced, and hence we have omitted them from this figure. Since none of those curves fell above the $n = 7$ curve, the gap shown between the $n = 7$ and $n = 15$ ridges is a true gap.

3.3. *Determination of the number of n-leaks to be included in the fitting model profile*

As we have already pointed out in Paper I, the number of n-leaks, N, to be included in the fitting model profile defined in Equation (1), cannot be determined from first principles. Therefore, we first choose a range

$$\max (l_0 - l_{\text{range}}, 0) \leq l \leq l_0 + l_{\text{range}}, \tag{15}$$

$$\max (n_0 - n_{\text{range}}, 0) \leq n \leq n_0 + n_{\text{range}}, \tag{16}$$

of l- and n-values around the targeted mode (n_0, l_0, m_0). Suitable values of both l_{range} and n_{range} are given in Table 1. These values were determined in a second trial-and-error process such that all of

Table 1. Values of l_{range} and n_{range} in dependence of degree l of the targeted multiplet (n, l).

	l_{range}	n_{range}
$0 \leq l \leq 2$	17	6
$3 \leq l \leq 6$	6	2
$l \geq 7$	3	1

the peaks that fell within a given multiplet in the zonal spectrum would also be fit in all of the other $2l$ un-averaged spectra.

Next, for every multiplet (n, l) that is included in the range as defined in Equations (15) and (16), and for which the radial order n is different from the radial order n_0 of the targeted mode, we compute from the respective frequency-splitting coefficients taken from a seed table the frequency $\nu_{n,l,m}^{n\text{-leak}}$ of the mode (n, l, m) for which the azimuthal order m is given by

$$m = \max \left[(\min (m_0, l), -l \right].\tag{17}$$

Here, m_0 is the azimuthal order of the targeted mode (n_0, l_0, m_0). Finally, if the frequency $\nu_{n,l,m}^{n\text{-leak}}$ is within the frequency range of the fitting box of the targeted mode (n_0, l_0, m_0) (cf. Section 3.2), we include the mode (n, l, m) as n-leak in Equation (1). Here, however, some care is necessary to avoid overlapping peaks in the fitting box, because the n-leak to be inserted could either interfere with the targeted peak or else blend with another n-leak that has already been inserted.

During our efforts to determine the values of both l_{range} and n_{range}, as given in Table 1, we noticed in the power spectra obtained from the $\mathcal{R}2010\_66$ observing run spurious peaks at the frequencies listed in Table 2 that we could not assign to any known mode. Specifically, these peaks occur in fitting boxes of targeted modes with low l- and high n-values. So far, we have been unable to come up with a reasonable explanation of these peaks. Nevertheless, for $l \leq 20$ we include them in our fits as so-called artificial n-leaks. To distinguish them from ordinary n-leaks, we label them with $m = 0$, and with negative values of both l and n, as is shown in Table 2.

3.4. *Determination of the fitting vector*

In the WMLTP method the modal parameters can be determined by means of a least-squares procedure (cf. Paper I). However, such an approach is inappropriate in the MPTS method because the power in a single frequency bin of a power spectrum obeys an exponential rather than a Gaussian distribution as in the case of an m-averaged spectrum for degrees $l \gg 1$. As a result, in order to estimate the fitting vector $\boldsymbol{p}$ given in Equation (8), in the MPTS method we need to resort to a maximum likelihood method. Specifically, following Anderson et al. (1990) we estimate the fitting vector $\boldsymbol{p}$ by minimizing the function

$$S(\boldsymbol{p}) = \sum_i \left(\ln M_{n,l,m}(\nu_i, \boldsymbol{p}) + \frac{d_i}{M_{n,l,m}(\nu_i, \boldsymbol{p})} \right) = -\ln L(\boldsymbol{p}) \overset{!}{=} \min \tag{18}$$

Table 2. Frequencies of spurious peaks detected in power spectra obtained from the $\mathcal{R}2010\_66$ observing run.

l	n	m	$\nu\ [\mu\mathrm{Hz}]$
-1	-1	0	1955.98 ± 0.41
-1	-2	0	2495.88 ± 0.47
-1	-3	0	2628.78 ± 0.37
-1	-4	0	3168.35 ± 0.23
-1	-5	0	3302.15 ± 0.24
-1	-6	0	3310.30 ± 0.25
-1	-7	0	3438.78 ± 0.33

in a fitting box (cf. Section 3.2) centered around the targeted peak (n, l, m). Here, d_i is the measured power in bin i at frequency ν_i, and $M_{n,l,m}(\nu, \boldsymbol{p})$ is the model profile as given in Equation (1). Obviously, minimizing the function $S(\boldsymbol{p})$ in a selected frequency range ν_i, $i_{\min} \leq i \leq i_{\max}$, centered around the targeted peak is equivalent to maximizing the likelihood function $L(\boldsymbol{p})$ in the same frequency range, and yields the maximum likelihood estimate of the fitting vector $\boldsymbol{p}$ for the mode (n, l, m). The $1\,\sigma$ confidence interval on each fit parameter $p_i \in \boldsymbol{p}$ is calculated from the inverse of the Hessian matrix at the minimum of $S(\boldsymbol{p})$. This approach seems to overestimate the errors of the fit parameters somewhat, particularly for the high-degree modes, as we have checked by comparing them with the corresponding intrinsic scatter.

In order to make the solution of the optimization problem formulated in Equation (18) as robust as possible various provisions are made. First, every fit parameter $p_i \in \boldsymbol{p}$ is scaled such as to make its value on the order of unity. This scaling greatly improves the numerical stability of the solution of the optimization problem. Second, every fit parameter $p_i \in \boldsymbol{p}$ is subject to bounds, i.e., it is constrained to lie within a prescribed interval. This is important in order to avoid unphysical values of any of these fit parameters, for example, negative amplitudes, frequencies too much off from their seed values, line widths much smaller than the spectral resolution, or line widths on the order of the width of the fitting box. Also, the magnitude of the line asymmetry parameters $B_{l,m}$ and B_i, $i = 1, \ldots, N$, of the targeted peak and the n-leak peaks, respectively, is constrained to values less than or equal to 0.20 (cf. Appendix A). Third, the fitting vector $\boldsymbol{p}$ is determined in several passes. In Table 3 it is shown which parameters are fitted in the individual passes. We note that the permutations given in Table 3 were chosen on purely heuristic grounds and are, therefore, somewhat arbitrary.

Because the fit parameters $p_i \in \boldsymbol{p}$ are subject to bounds, we actually have to solve for the determination of the fitting vector $\boldsymbol{p}$ the constrained non-linear optimization problem

$$\begin{aligned} &\underset{\boldsymbol{p}}{\text{minimize}}\ S(\boldsymbol{p}) \\ &\text{subject to}\ \ \pi_i^{\mathrm{low}} \leq p_i \leq \pi_i^{\mathrm{up}}. \end{aligned} \tag{19}$$

Here, $S(\boldsymbol{p})$ is given in Equation (18), and π_i^{low} and π_i^{up} are, respectively, the lower and upper bounds of the fit parameter $p_i \in \boldsymbol{p}$. As in the WMLTP method (cf. Paper I), we solve the constrained

Table 3. Fit parameters invoked in the individual passes used for determining the fitting vector $\boldsymbol{p}$.

pass	fit parameters main peak & background								fit parameters n-leaks $i = 1, \ldots, N$			
#1	$A_{l,m}$	$\nu_{l,m}$	$w_{l,m}$	$\cdots$	a	$\cdots$	$\cdots$		A_i	$\cdots$	$\cdots$	$\cdots$
#2	$A_{l,m}$	$\nu_{l,m}$	$w_{l,m}$	$\cdots$	a	$\cdots$	$\cdots$		A_i	ν_i	$\cdots$	$\cdots$
#3	$A_{l,m}$	$\nu_{l,m}$	$w_{l,m}$	$\cdots$	a	$\cdots$	$\cdots$		A_i	ν_i	$\cdots$	$\cdots$
#4	$A_{l,m}$	$\nu_{l,m}$	$w_{l,m}$	$\cdots$	a	b	$\cdots$		A_i	ν_i	$\cdots$	$\cdots$
#5	$A_{l,m}$	$\nu_{l,m}$	$w_{l,m}$	$B_{l,m}$	a	b	c		A_i	ν_i	w_i	$\cdots$
#6	$A_{l,m}$	$\nu_{l,m}$	$w_{l,m}$	$B_{l,m}$	a	b	c		A_i	ν_i	w_i	B_i

NOTE— The value of a parameter that is not invoked in a specific pass is set to either its initial guess or else to its value as determined in a previous pass. For the initial guess of the line asymmetry parameter we use $B_{l,m} = 0$ and $B_i = 0$, $i = 1, \ldots, N$. The initial guesses of the remaining fit parameters are taken from seed tables. If the symmetrical profile is used, both $B_{l,m}$ and B_i, $i = 1, \ldots, N$ are kept fixed to zero in all passes. To increase the numerical stability of the MPTS code rather tight constraints are applied to the fit parameters in passes #1 through #5, while they are relaxed as much as possible in the final pass #6. Pass #3 differs from pass #2 by the fact that in pass #2 both A_i and ν_i are fit consecutively from $i = 1$ to $i = N$ keeping both A_i and ν_i of the remaining n-leaks constant, while in pass #3 all of the listed parameters are fitted simultaneously.

optimization problem given in Equation (19) by using the FORTRAN code `NLPQL` which is a special implementation of a so-called sequential quadratic programming method (Schittkowski 1986). The method is based on solving a series of sub-problems designed to minimize a quadratic approximation to the Lagrangian function subject to a linearization of the constraints. Sequential quadratic programming is one of the most robust algorithms for the solution of non-linear continuous optimization problems.

3.5. *The internal fixed-point iteration*

Once all of the spectra of a given multiplet (n, l) have been fitted, we have available for each m the amplitudes $A_{n,l,m}$, the frequencies $\nu_{n,l,m}$, the line widths $w_{n,l,m}$, and the line asymmetries $B_{n,l,m}$, of the $2l+1$ modes comprising that multiplet. Typical examples are given in Section 4.3. We note, however, that for some values of m it may happen that the optimization problem given in Equation (19) fails to converge. As long as the number of failed cases is much smaller than $2l+1$, we proceed as follows, while otherwise we regard the multiplet (n, l) as a failed case.

We first fit the natural logarithm of the amplitudes $A_{n,l,m}$ as a function of m/L (cf. Section 4.3) where $L^2 = l(l + 1)$, using an ϖth degree Chebyshev polynomial $\Xi_\varpi(x)$ in x, $-1 \leq x \leq +1$, with

coefficients $\boldsymbol{c} = (c_0, c_1, \ldots, c_\varpi)$, which is defined as the solution of the constrained optimization problem

$$\operatorname*{minimize}_{\boldsymbol{c}} \int\limits_{x_{\mathrm{lw}}}^{x_{\mathrm{up}}} \left(\frac{\mathrm{d}^2 \varXi_\varpi(x)}{\mathrm{d}x^2} \right)^2 \mathrm{d}x$$

$$\text{subject to} \quad \sum_{m=-l}^{+l} \left[\ln A_{n,l,m} - \varXi_\varpi(m/L) \right]^2 \leq \chi^2_{\mathrm{aim}}$$

$$\left. \frac{\mathrm{d}\varXi_\varpi(x)}{\mathrm{d}x} \right|_{x=x_{\mathrm{lw}}} = s_{\mathrm{lhs}}$$

$$\left. \frac{\mathrm{d}\varXi_\varpi(x)}{\mathrm{d}x} \right|_{x=x_{\mathrm{up}}} = s_{\mathrm{rhs}}.$$

(20)

The rationale behind this ansatz is to find a smooth curve with the smallest total curvature which fits the data and avoids wiggles at both the left-hand and the right-hand side of the fitting interval. In Equation (20)

$$x_{\mathrm{lw}} = -l/L, \quad x_{\mathrm{up}} = +l/L,$$

(21)

are, respectively, the lower and upper bound of the fitting interval, χ^2_{aim} is a suitably chosen value of the sum of squares, and s_{lhs} and s_{rhs} are, respectively, prescribed values of the slopes of the Chebyshev polynomial $\varXi_\varpi(x)$ at the left-hand and the right-hand side, respectively, of the fitting interval. The slopes s_{lhs} and s_{rhs} are determined by fitting a straight line to $\ln A_{n,l,m}$ in the ranges $x_{\mathrm{lw}} \leq x \leq -0.5$ and $0.5 \leq x \leq x_{\mathrm{up}}$, respectively. We note that the choice of χ^2_{aim} is critical because for a too small value of χ^2_{aim} the optimization problem given in Equation (20) may not have a solution at all, and for a too large value of χ^2_{aim} the fit may become poor. The polynomial degree ϖ is determined by fitting in the range $x_{\mathrm{lw}} \leq x \leq x_{\mathrm{up}}$ in an unconstrained manner, for $\varkappa = 2, \ldots, \varkappa_{\mathrm{max}}$, the $\varkappa$th degree polynomial $\varXi_\varkappa(x)$ to $\ln A_{n,l,m}$. We use $\varkappa_{\mathrm{max}} = \min(75, N_{\mathrm{dat}} - 1)$, where N_{dat} is the number of given data points in the $\ln A_{n,l,m}$ array. Usually, $N_{\mathrm{dat}} = 2l + 1$, but may be less than this because of failed cases. For each polynomial degree $\varkappa$ we calculate both the resulting sum of squares $\chi^2_\varkappa$ and the probability $P_\varkappa^{(\chi^2)}(\chi^2 \leq \chi^2_\varkappa)$ to observe a sum of squares χ^2 less than or equal to $\chi^2_\varkappa$. For polynomial degrees $\varkappa > 2$ we additionally calculate the so-called R-statistic

$$R = \left(N_{\mathrm{dat}} - \varkappa - 1 \right) \frac{\chi^2_{\varkappa-1} - \chi^2_\varkappa}{\chi^2_\varkappa}$$

(22)

(Frieden 1983) as well as the probability $P_\varkappa^{(R)}(r \leq R)$ to observe a value r of the R-statistic that is less than or equal to R. Following Frieden (1983), the probability $P_\varkappa^{(R)}(r \leq R)$ can be calculated from Snedecor's $F(d_1, d_2)$-distribution with $d_1 = 1$ degrees of freedom for the numerator and $d_2 = N_{\mathrm{dat}} - \varkappa - 1$ degrees of freedom for the denominator. We increase the polynomial degree $\varkappa$ up to $\varkappa_{\mathrm{max}}$ until the following conditions are met

$$P_\varkappa^{(\chi^2)}(\chi^2 \leq \chi^2_\varkappa) < P_{\mathrm{crit}}^{(\chi^2)}, \quad P_{\varkappa-1}^{(R)}(r \leq R) < P_{\mathrm{crit}}^{(R)}, \quad P_\varkappa^{(R)}(r \leq R) < P_{\mathrm{crit}}^{(R)},$$

(23)

and take this value of $\varkappa$ as the polynomial degree ϖ to be used in the optimization problem given in Equation (20). In our applications we use $P_{\mathrm{crit}}^{(\chi^2)} = 0.995$ and $P_{\mathrm{crit}}^{(R)} = 0.999$. These values are uncritical

as long as they are close to one. We found that the such determined value of ϖ can become as high as 60. This shows in hindsight that it is essential to use Chebyshev rather than ordinary polynomials in order to avoid numerical issues. On average, we have $\varpi = 9$. Of course, it is meaningful to only solve the optimization problem given in Equation (20) if the number of data points N_{dat} is large enough. Hence, for $N_{\mathrm{dat}} < 20$ we simply fit to $\ln A_{n,l,m}$ in an unconstrained manner either a straight line or a parabola. We calculate the amplitude of the multiplet (n, l) from the value of the fitted polynomial $\Xi_\varpi(x)$ at $x = 0$, i.e.

$$A_{n,l} = \exp\left(\Xi_\varpi(0)\right), \tag{24}$$

and the $3.5\,\sigma$ confidence interval, $\Delta A_{n,l}$, thereof from the inverse of the Hessian matrix at the solution of the optimization problem given in Equation (20). We note that we solve this optimization problem by means of the FORTRAN code `NLPQL` of Schittkowski (1986).

Next, we expand the frequencies $\nu_{n,l,m}$, $m = -l, \ldots, +l$, (cf. Section 4.3) in the orthogonal polynomials $\mathcal{P}_k^{(l)}$ of Ritzwoller & Lavely (1991), viz.

$$\nu_{n,l,m} = \sum_{k=0}^{k_{\max}} a_k^{(n,l)} \mathcal{P}_k^{(l)}(m), \tag{25}$$

where the $a_k^{(n,l)}$ are the so-called frequency-splitting coefficients (a-coefficients) of the multiplet (n, l). The odd terms in this polynomial expansion represent the rotational splitting, while the even terms are due to the asphericity of the solar structure. A similar expansion of the frequency splittings using Legendre polynomials, however, was first suggested by Duvall et al. (1986). The a-coefficients $a_k^{(n,l)}$ are determined by fitting in a weighted fashion the right-hand side of Equation (25) in the least-squares sense to the frequencies $\nu_{n,l,m}$, using as weights the inverses of the frequency uncertainties $\Delta\nu_{n,l,m}$. The value of $k_{\max}$ in Equation (25) is determined by means of the R-statistic (cf. Equation (22)) in a similar manner as we have determined the polynomial degree ϖ to be employed in the fitting of the amplitudes $A_{n,l,m}$. In early versions of the MPTS code we used for the maximum order of the a-coefficients $k_{\max} = \min(24, 2l)$. However, we noticed that the convergence of the internal fixed-point iteration could be considerably improved by utilizing $k_{\max} = \min(5, 2l)$ instead. This means, on the other hand, that only the coefficients $a_1^{(n,l)}$ through $a_5^{(n,l)}$ can be determined at most. The mean-multiplet frequency $\nu_{n,l}$ of the multiplet (n, l) and the uncertainty thereof, $\Delta\nu_{n,l}$, are given by

$$\nu_{n,l} = l\, a_0^{(n,l)}, \quad \Delta\nu_{n,l} = l\, \Delta a_0^{(n,l)}, \tag{26}$$

where the $1\,\sigma$ uncertainty $\Delta a_0^{(n,l)}$ is determined as described in Appendix A of Paper I.

Next, we fit the natural logarithm of the line widths $w_{n,l,m}$ as a function of m/L. Initially, we found that the scatter of the line widths across many of the multiplets was quite large, but subsequent analysis that we will describe in Section 4.2.3 showed that polynomials could be fit to the line widths within each multiplet that had a characteristic shape to them, such as shown by the blue curves in both panels of Figure 11. Nevertheless, we found that for frequencies above $2500\,\mu$Hz the deviations of the minima of the polynomials from their average values were less than about 5 percent, and we therefore fit the line widths as a function of m/L with a horizontal straight line; that is, we used a constant $b_0 = \ln w_{n,l,m}$, which we determined by resorting to a so-called robust fitting technique (Press et al. 1992). Such techniques are well known for their characteristic of being less sensitive to

outliers than the traditional least-squares method. Specifically, we determine the constant b_0 as the solution of the optimization problem,

$$\underset{b_0}{\text{minimize}} \sum_{m=-l}^{+l} \ln\left[1 + \frac{g_m^2}{2}\left(\ln w_{n,l,m} - b_0\right)^2\right], \tag{27}$$

with $g_m = w_{n,l,m}/\Delta w_{n,l,m}$, where $\Delta w_{n,l,m}$ is the uncertainty of the line width $w_{n,l,m}$. We note that due to failed cases the sum in Equation (27) may include less than $2l+1$ summands. We solve the optimization problem given in Equation (27) by means of the FORTRAN code NLPQL of Schittkowski (1986) to get the solution $b_0^{(1)}$ and the 1σ uncertainty $\Delta b_0^{(1)}$ thereof, which we calculate from the inverse of the Hessian matrix at the solution. Because there could be lurking outliers in the weights g_m due to unreasonably small uncertainties $\Delta w_{n,l,m}$, we solve the optimization problem given in Equation (27) a second time, but use instead $g_m = 1$ throughout, to get $b_0^{(2)}$ and $\Delta b_0^{(2)}$. By averaging the two solutions $b_0^{(1)}$ and $b_0^{(2)}$, we finally get for the line width $w_{n,l}$ and its 1σ uncertainty $\Delta w_{n,l}$ of the multiplet (n,l),

$$w_{n,l} = \left(w^{(1)} + w^{(2)}\right)/2,$$

$$\Delta w_{n,l} = \frac{1}{2}\sqrt{\left(w^{(1)}\Delta b_0^{(1)}\right)^2 + \left(w^{(2)}\Delta b_0^{(2)}\right)^2}, \tag{28}$$

with

$$w^{(1)} = \exp\left(b_0^{(1)}\right), \quad w^{(2)} = \exp\left(b_0^{(2)}\right). \tag{29}$$

Finally, at the end of the first iteration step of the internal fixed-point iteration, we fit the line asymmetries $B_{n,l,m}$ as a function of m/L. Just as was the case with the line widths, our initial values of the line asymmetries within many of the individual multiplets showed little systematic variation. Subsequently, we found that we could fit polynomials to the sets of line asymmetries, as we will describe in Section 4.2.4, and we also found that the deviations of those polynomials from constant values only became sizeable for modes having higher frequencies and/or higher degrees, as shown in the right-hand panel of Figure 13. Therefore, fitting the line asymmetries in terms of m/L could have be done in exactly the same manner as we just described for the fitting of the line widths. However, our experiences with earlier versions of the MPTS code showed that it sufficed to simply calculate the weighted mean of the line asymmetries to get the line asymmetry $B_{n,l}$ of the multiplet (n,l), i.e.

$$B_{n,l} = \frac{\displaystyle\sum_{m=-l}^{+l} \alpha_m B_{n,l,m}}{\displaystyle\sum_{m=-l}^{+l} \alpha_m} \tag{30}$$

(Menzel 1960). Here, the weights α_m are given by $1/\Delta B_{n,l,m}$, with $\Delta B_{n,l,m}$ being the uncertainty of $B_{n,l,m}$. We note, however, that the weight is reduced by a factor of ten for those modes with $|B_{n,l,m}| = 0.20$ (cf. Appendix A). The statistical uncertainty $\Delta B_{n,l}$ of $B_{n,l}$ is given by

$$\Delta B_{n,l}^{\text{stat}} = \sigma\, t_{1-\gamma/2,2l+1} \frac{\sqrt{\displaystyle\sum_{m=-l}^{+l} \alpha_m^2}}{\displaystyle\sum_{m=-l}^{+l} \alpha_m}. \tag{31}$$

Here,

$$\sigma = \sqrt{\frac{1}{2l} \sum_{m=-l}^{+l} (B_{n,l,m} - \bar{B})}, \tag{32}$$

where $\bar{B}$ is the unweighted mean of the line asymmetries $B_{n,l,m}$ (Menzel 1960), and $t_{1-\gamma/2,2l+1}$ is the $100(1 - \gamma/2)$ percentage point of Student's t-distribution with $2l + 1$ degrees of freedom. For a $3.5\,\sigma$ confidence interval $\gamma = 4.65 \cdot 10^{-4}$. We note that all sums above may include less than $2l + 1$ terms because of failed cases. If so, the denominator in Equation (32) as well as the degrees of freedom of the t-distribution must be suitably adapted.

Because of the systematic variation of the line asymmetries across most of the individual multiplets of modes having higher frequencies and/or higher degrees, we found the statistical error estimate $\Delta B_{n,l}^{\mathrm{stat}}$, as given in Equation (31), as being unrealistically small. Therefore, we increased the statistical uncertainty by quadratically adding the systematic uncertainty $\Delta B_{n,l}^{\mathrm{sys}}$ to eventually get the uncertainty $\Delta B_{n,l}$ of the line asymmetry $B_{n,l}$, viz.

$$\Delta B_{n,l} = \sqrt{\left(\Delta B_{n,l}^{\mathrm{stat}}\right)^2 + \left(\Delta B_{n,l}^{\mathrm{sys}}\right)^2}. \tag{33}$$

We estimate the systematic uncertainty by first fitting the line asymmetries $B_{n,l,m}$ as a function of $x = m/L$ using an ϖth degree Chebyshev polynomial $\Phi_\varpi(x)$ in x, $-1 \leq x \leq +1$, with coefficients $\boldsymbol{d} = (d_0, d_1, \ldots, d_\varpi)$, which is defined as the solution of the constrained optimization problem

$$\underset{\boldsymbol{d}}{\text{minimize}} \int_{x_{\mathrm{lw}}}^{x_{\mathrm{up}}} \left(\frac{\mathrm{d}^2 \Phi_\varpi(x)}{\mathrm{d}x^2}\right)^2 \mathrm{d}x$$

$$\text{subject to} \sum_{m=-l}^{+l} \left[B_{n,l,m} - \Phi_\varpi(m/L)\right]^2 \leq \chi_{\mathrm{aim}}^2$$

$$\left.\frac{\mathrm{d}^2 \Phi_\varpi(x)}{\mathrm{d}x^2}\right|_{x=x_{\mathrm{lw}}} = 0$$

$$\left.\frac{\mathrm{d}^2 \Phi_\varpi(x)}{\mathrm{d}x^2}\right|_{x=x_{\mathrm{up}}} = 0. \tag{34}$$

This is exactly the same approach as the one we used for fitting the amplitudes $A_{n,l,m}$ as a function of m/L, except that we here are employing so-called natural boundary conditions $\mathrm{d}^2\Phi_\varpi(x)/\mathrm{d}x^2 = 0$ at both the left-hand and the right-hand side of the fitting interval $x_{\mathrm{lw}} \leq x \leq x_{\mathrm{up}}$ (cf. Equation (21)). All other aspects of this approach remain unchanged. In particular, the determination of the polynomial degree ϖ is handled in the same manner. Next, we define the systematic uncertainty $\Delta B_{n,l}^{\mathrm{sys}}$ to be the maximum absolute deviation of the fitted polynomial Φ_ϖ from the constant value $B_{n,l}$, as given in Equation (30), viz.

$$\Delta B_{n,l}^{\mathrm{sys}} = \max_m \left|\Phi_\varpi(m/L) - B_{n,l}\right|. \tag{35}$$

Once we have completed, for the multiplet (n, l), the fitting of $\ln A_{n,l,m}$, $\nu_{n,l,m}$, $\ln w_{n,l,m}$, and $B_{n,l,m}$ as functions of m/L, we use the results from these fits to update for this multiplet the seed frequency, the seed frequency-splitting coefficients, the seed line width, the seed amplitude fitting coefficients $\boldsymbol{c}$

(cf. Equation (20), and the seed line asymmetry, and start the next step of the internal fixed-point iteration. This procedure is repeated until the following conditions are met,

$$\left|\xi_j^{(\mathrm{act})} - \xi_j^{(\mathrm{prv})}\right| < \sqrt{\left(\Delta\xi_j^{(\mathrm{act})}\right)^2 + \left(\Delta\xi_j^{(\mathrm{prv})}\right)^2}, \quad j = 1,\dots,4, \tag{36}$$

with $\xi_1 \equiv A_{n,l}$, $\xi_2 \equiv \nu_{n,l}$, $\xi_3 \equiv w_{n,l}$, $\xi_4 \equiv B_{n,l}$, $\Delta\xi_1 \equiv \Delta A_{n,l}$, $\Delta\xi_2 \equiv \Delta\nu_{n,l}$, $\Delta\xi_3 \equiv \Delta w_{n,l}$, and $\Delta\xi_4 \equiv \Delta B_{n,l}$. Here, the superscripts (prv) and (act) refer to the previous and the actual iteration step, respectively. We note that at least 3 iteration steps are performed regardless of whether the convergence criteria given in Equation (36) are met, and that we regard the multiplet as a failed case if convergence is not reached within 15 iteration steps. We also note that the use of $3.5\,\sigma$ uncertainties for both $\Delta A_{n,l}$ and $\Delta B_{n,l}$ improves the performance of the internal fixed-point iteration considerably.

3.6. *The external fixed-point iteration*

Apart from the targeted mode, the fitting profile given in Equation (1) also depends on modes the parameters of which are not updated in the internal fixed-point iteration, but are rather fixed and are taken from seed tables. Therefore, it is essential to update those seed tables after all modes of a given observing run have been processed. Unfortunately, the generation of new seed tables is extremely time consuming as the amplitude, line width, frequency, line asymmetry and odd-order splittings must be fitted, as functions of l for each n, in order to get values free of outliers as input for the next external iteration step. We note that the even splitting coefficients a_0, a_2, a_4 should not be fitted because the internal fixed-point iteration always starts with $a_0 = a_2 = a_4 = 0$. Despite of intensive efforts we have not been able so far to fully automate those fitting tasks. Rather, many manual interventions are always required in order to achieve satisfactory results. Depending on the quality of the seed tables with which the processing of an observing run is started, three to four iterations of the external fixed-point iteration are required. A typical example of the performance of the external fixed-point iteration is shown here in Table 4. As can be seen, for all three variables shown, viz. frequency, line width, and a_1-splitting coefficient, the averages of the differences $\mathrm{p}_i - \mathrm{p}_{i-1}$ either decrease or else remain small in the course of the iteration. The same is true for the averages of the differences $\mathrm{p}_i - \mathrm{s}_i$. As a result, we can be fairly confident that the external fixed-point iteration performs in a satisfactory way.

In order to avoid any confusion, we point out the following. The basic principle of the external fixed-point iteration is to use the results p_i from iteration step i as seed values s_{i+1} in step $i+1$. Therefore, one might think that $p_{i+1} - p_i = p_{i+1} - s_{i+1}$. As can be seen from Table 4, however, this assumption is not confirmed, and indeed for the following reasons. First, because of possible outliers the results are smoothed before they are used as seeds. Therefore, we have $s_{i+1} \approx p_i$. Second, because of inter-dependencies between the fit variables, and because seed tables are used for many of them, p_{i+1} depends not only on s_{i+1} but also on seed values for other variables. As a result, in general we have $p_{i+1} - p_i \neq p_{i+1} - s_{i+1}$.

4. SAMPLE RESULTS FROM MPTS METHOD

In this section we present some results of our method applied to the $\mathcal{R}2010\_66$ observing run. The current version of the MPTS code allows us to obtain estimates of the frequency-splitting coefficients, the frequencies, the amplitudes (power densities), the line widths, and the line asymmetries of f- and p-modes in the degree range of 0 to 1000, the radial order range of 0 to 30, and the frequency range

Table 4. Performance of the external fixed-point iteration in terms of averages over the multiplets.

diff	frequency			line width			a_1-splitting coefficient			
	avg	std	n_{out}	avg	std	n_{out}	avg	std	n_{out}	n_{c}
p_2-p_1	4.015	6.054	1	-0.016	0.495	204	0.171	2.131	23	6677
p_3-p_2	0.170	0.828	22	0.012	0.178	539	-0.181	2.049	40	6677
p_4-p_3	0.059	0.710	29	-0.020	0.149	496	0.159	1.332	40	6677
p_1-s_1	8.214	17.874	4	0.607	2.057	156	-1.848	5.621	22	6679
p_2-s_2	5.267	8.364	0	-0.057	0.926	251	0.239	3.010	22	6678
p_3-s_3	0.195	1.694	9	0.015	0.357	291	-0.239	2.796	31	6677
p_4-s_4	0.104	1.327	18	-0.083	0.540	223	0.209	2.464	23	6677

NOTE— In the first column the kind of difference is indicated for which in the corresponding row the average, avg, the standard deviation, std, and the number of rejected outliers, n_{out}, is listed for the fit parameters frequency, line width, and splitting coefficient, a_1, respectively. The difference p_i-p_{i-1} measures the change of the parameter p from iteration $i-1$ to i in units of the uncertainty of this difference, and is given by $\left(\xi_{n,l}^{(\mathrm{fit},i)} - \xi_{n,l}^{(\mathrm{fit},i-1)}\right) / \sqrt{\left(\Delta\xi_{n,l}^{(\mathrm{fit},i)}\right)^2 + \left(\Delta\xi_{n,l}^{(\mathrm{fit},i-1)}\right)^2}$, where $\xi_{n,l}$ can be any of the parameters frequency, line width, or a_1-splitting coefficient, respectively, that characterize the multiplet (n, l), and where $\Delta\xi_{n,l}$ denotes the uncertainty of $\xi_{n,l}$. The difference p_i-s_i, given by $\left(\xi_{n,l}^{(\mathrm{fit},i)} - \xi_{n,l}^{(\mathrm{seed},i)}\right) / \Delta\xi_{n,l}^{(\mathrm{fit},i)}$, measures in iteration i the deviation of the fitted value from the corresponding seed value in units of the uncertainty of the fitted value. The last column contains the number of cases considered, n_{c}, for the difference, diff, as indicated in the corresponding row in the first column.

of ≈ 1000 to $4600\,\mu$Hz. In the midterm, we plan to fit the f-modes up to $l = 1500$, and the p-modes of the $n = 1$ ridge up to $l \approx 1350$. For the ridges $n \geq 2$ the p-mode frequencies already hit the upper frequency limit of $4600\,\mu$Hz for $l < 1000$. The boundaries of both the frequency and the radial order range are given by the requirement that the signal-to-noise ratio of the spectra must be large enough to ensure the convergence of the internal fixed-point iteration implemented into the MPTS code (cf. Section 3.5). Incidentally, the upper frequency limit of $4600\,\mu$Hz is well below the acoustic cut-off frequency of the Sun so that the problems with the asymmetrical profile of Nigam & Kosovichev (1998), as discussed in Section 4.6 of Paper I, are avoided.

4.1. *Sample fitted profiles produced by the MPTS Method*

A major feature of the MPTS method is its generation of a separate numerical profile for each individual mode that the method fits in each of the un-averaged power spectra. Since the slopes, $d\nu/dl$, of each of the f- and p-mode ridges systematically decrease with increasing degree, l, while the line widths, w, of the modes are increasing with increasing degrees, the nature of these fitted profiles also differs systematically across the l-ν plane. For those cases in which the line widths are substantially less than the slopes, the fitted profiles appear to consist of a series of narrow, well-

separated peaks that correspond to the target mode and to both spatial and temporal sidelobes. For those cases for which the line widths are roughly equal to the ridge slopes, the fitted profiles appear to be broader ridges of power that contain two or three narrow peaks near their centers, and for the cases for which the line widths are substantially larger than the ridge slopes, the fitted profiles take on the appearance of broad, single-peaked ridges of power. In all three types of fitted profiles, the frequency dependence of the modal amplitudes and the variations in the strengths of the various spatial and temporal leaks influence the overall shapes of these profiles. In Figures 2 through 4 we will show examples of all three types of fitted profiles.

4.1.1. *Sample profiles for low- and moderate-degree modes*

In Figure 2 we show observed spectra and fits for $n = 20$, $l = 10$ and selected values of m. In all examples shown, the l-leaks $l \pm 1$, $l \pm 2$ can be identified, and are well separated from the main peak by about $\pm 41.9\,\mu$Hz and $\pm 83.9\,\mu$Hz, respectively. The remaining peaks are n-leaks from ridges $n \pm 1$ with degrees ranging from $l = 7$ to $l = 13$. The mean line width of the multiplet is $2.4\,\mu$Hz.
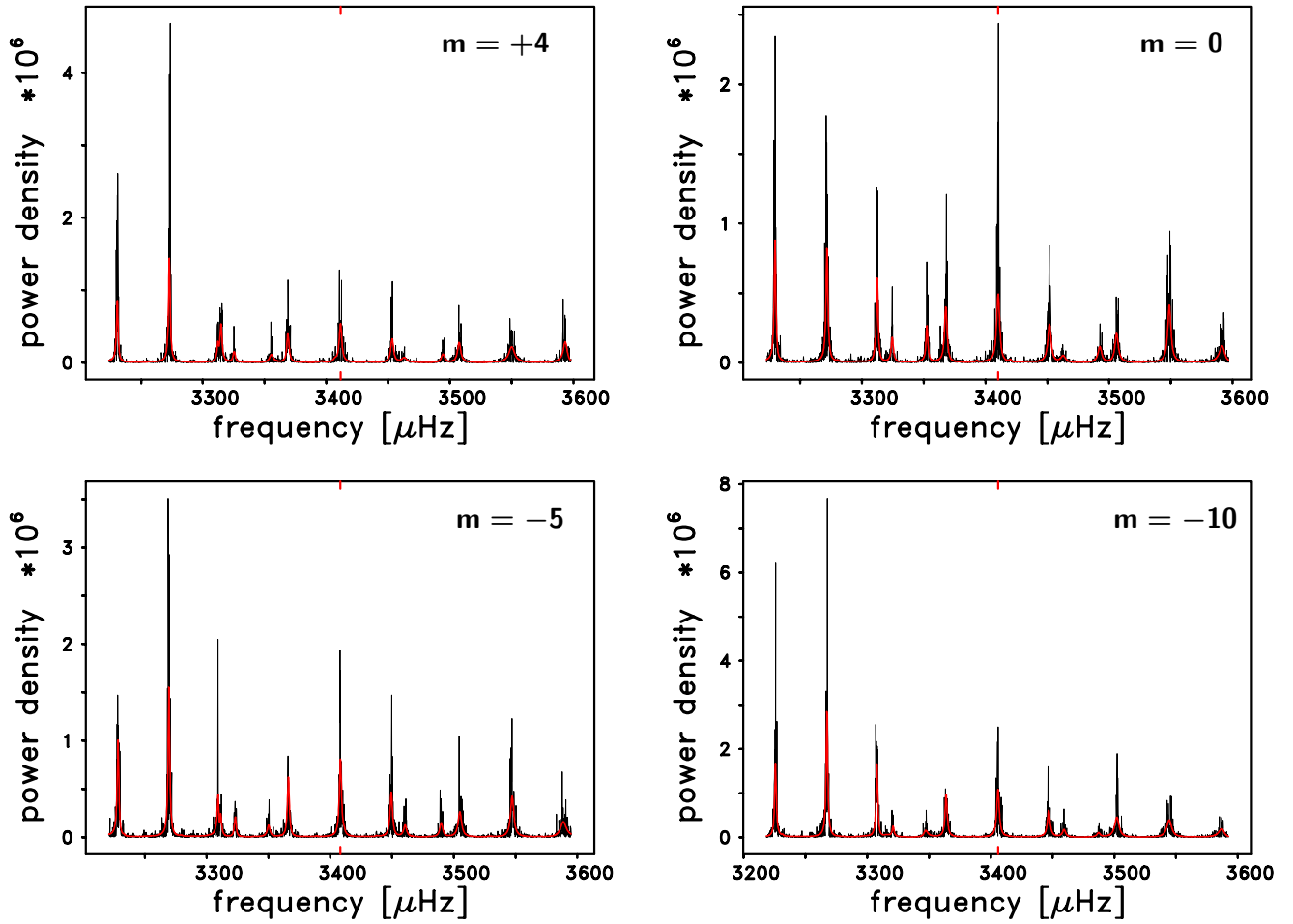
Figure 2. Observed (thin black) and fitted (thick red) spectra for various values of m for $n = 20$, $l = 10$. The power density is measured in uncalibrated units. The fitted frequencies of the targeted modes are indicated in each panel by tick marks at both the top and bottom axis. The two peaks at the far left side of the panels are n-leaks from the modes $n = 19$, $l = 9$ and $n = 19$, $l = 10$, respectively. We note the different scales of the ordinates.

4.1.2. *Sample profiles for intermediate-degree modes*

In Figure 3 we show four similar plots for the $(1, 200)$ multiplet. In contrast to the situation shown in Figure 2, here there are no n-leaks that are present in any of the panels. On the other hand, the much smaller separations of the $l \pm 1$ and $l \pm 2$ sidelobes, which have dropped to only ± 3.7 and $\pm 7.3 \, \mu$Hz, respectively, mean that the fitted profiles for both the zonal and sectoral spectra have largely merged with the targeted peaks into broad, multi-peaked ridges of observed power. For example, for both the zonal and sectoral spectra in Figure 3 the fitted profiles show two closely-spaced peaks spanning about $4 \, \mu$Hz near their centers, while for the two tesseral spectra the fitted profiles each show a total of three closely-spaced peaks located within a span of $8 \, \mu$Hz near their centers. By contrast, the mean line width of the $(1, 200)$ multiplet is $2.3 \, \mu$Hz.

4.1.3. *Sample profiles for high-degree modes*

Because of the decreasing slopes of the p-mode ridges with increasing degree above $l = 200$, the spacing of the $l \pm 1$ and $l \pm 2$ sidelobes continues to decrease while the intrinsic line width of each peak in a given multiplet increases since the frequency of each ridge is increasing as the degree increases. The combination of the decreasing sidelobe separations and the increasing line widths means that the broad, multi-peaked ridges of power that are shown in Figure 3 quickly become even broader,
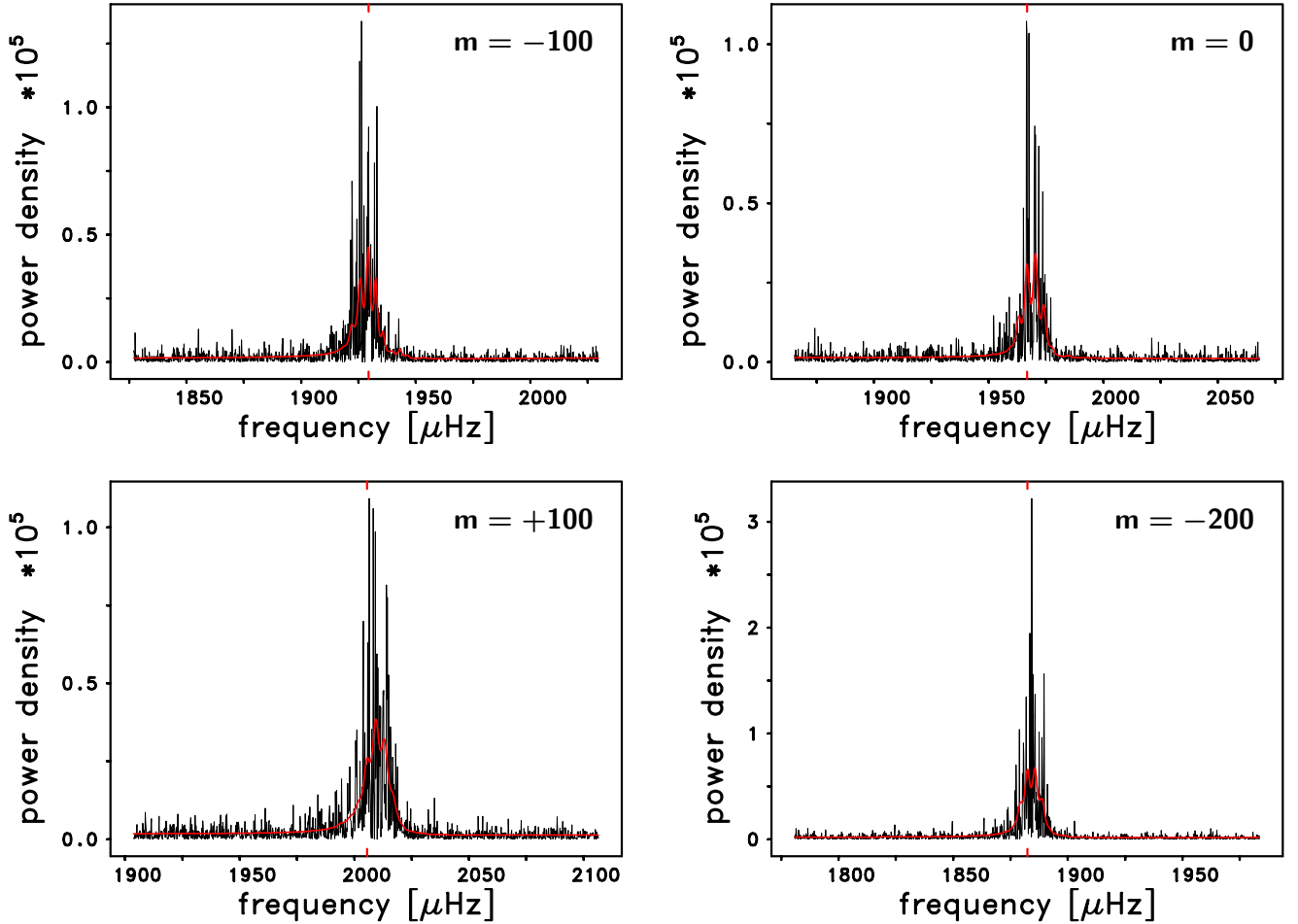
Figure 3. As for Figure 2, but for $n = 1$, $l = 200$.

single-peaked ridges, as we show in Figure 4 for the $(2, 600)$ multiplet. The sidelobes have now merged with the target peak and the fitted profile shows only a smooth ridge with a single peak at its center. As in Figure 3, there are no n-leaks that are present. The separations of the l-leaks from the targeted peak are multiples of $\pm 2.6\,\mu$Hz, while the mean line width of the multiplet is $28.6\,\mu$Hz.

In all four panels of Figure 4 the fitted profiles are asymmetric in shape and show higher levels of power on their low-frequency ends. Conversely, these four profiles show less power on their high-frequency ends because, as we will show shortly in Figure 18, the amplitudes along the $n = 2$ ridge are rapidly decreasing with increasing degree for degrees above $l = 345$. Since the lower frequency side of a given fitted profile comes from the power that leaks into the $l = 600$ spectrum from the spectra of lower degrees, those leaked peaks will have higher amplitudes than the target peaks. Conversely, the higher frequency side of a given ridge comes from sidelobes that have leaked into the target spectrum from higher degrees; hence, their amplitudes are lower than either the target peak or the low-frequency sidelobes.
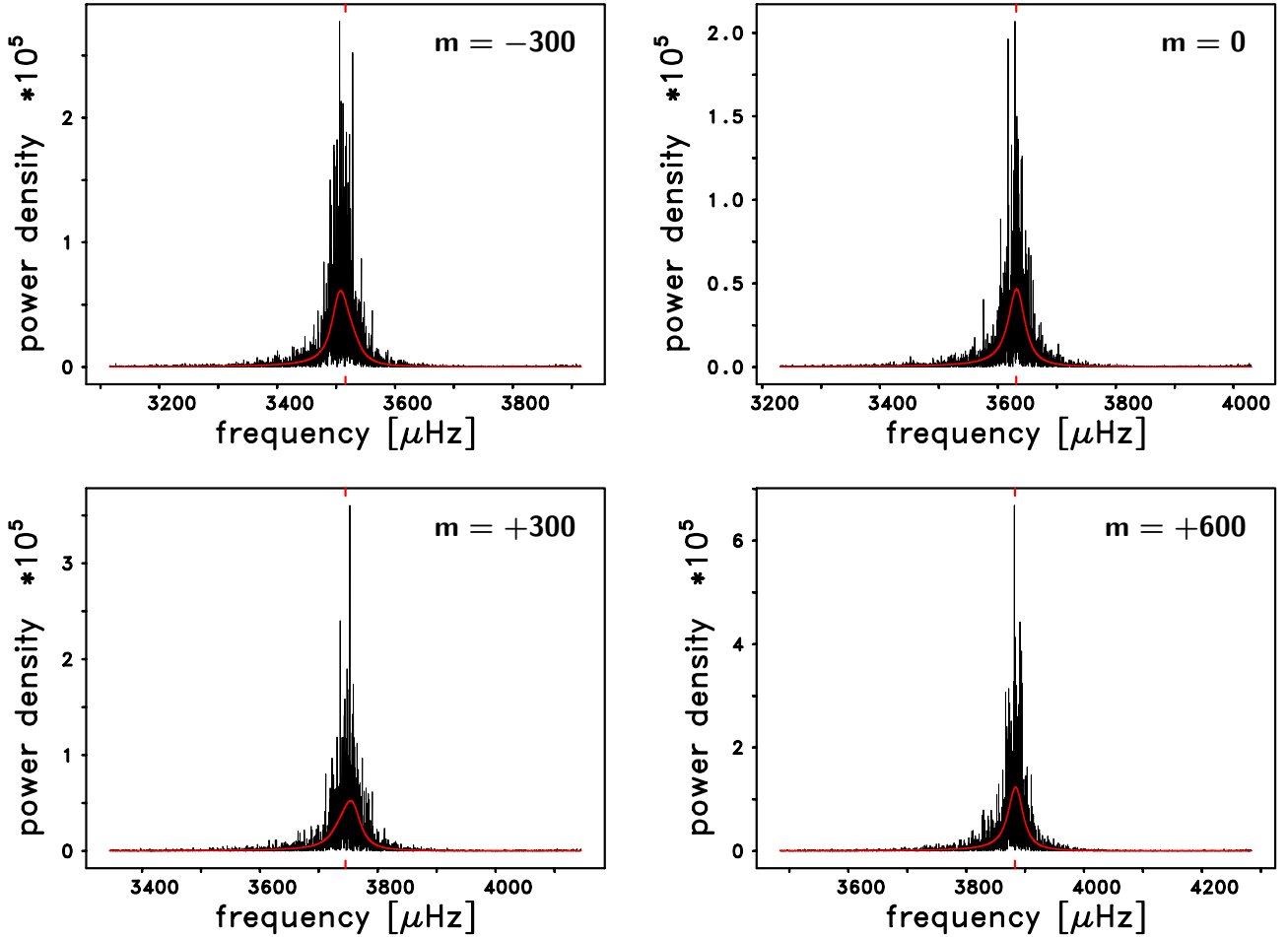
Figure 4. As for Figure 2, but for $n = 2$, $l = 600$.

4.2. *The influence of the leakage matrices upon the multiplet structure of the f- and p-mode parameters*

4.2.1. *Effects of leakage matrices on ridge frequencies*

A visual inspection of the two left-hand panels of Figure 4 shows that the peaks of the fits are shifted horizontally in opposite directions relative to the tick marks which show the fitted frequencies that the MPTS method produced for those two tesseral spectra. These apparently systematic differences in the fitted frequencies and in the peaks of the profiles led us to compute similar frequency differences for all of the 1201 individual spectra in the $(2, 600)$ multiplet. In each case, the peak frequency was simply determined by finding the maximum value of the fitted profile over all of the frequency bins within the fitting box. When we plotted all 1201 of these frequency differences, which we define as $\delta\nu = \nu_{\mathrm{peak}} - \nu_{\mathrm{fit}}$, we found the pattern that is shown as the set of black symbols in the lower-left panel of Figure 5. This panel clearly shows that the minimum and maximum frequency offsets between the peaks of the fitted profiles and the fitted frequencies given by the MPTS program occurred for values of m/L that were close to ± 0.5, respectively. The set of 1201 black symbols that are shown in this panel of Figure 5 constitute an example of what has been called "frequency pulling" in the literature of solar oscillation frequency estimation (Duvall et al. 1988; Libbrecht & Kaufman 1988; Libbrecht et al. 1990).

The systematic variation of the differences between the peak frequencies and the fitted frequencies for the entire $(2, 600)$ multiplet suggested that there might be a single property of the relevant leakage matrices that could explain this pattern. Since, as we have already mentioned, the largest absolute values of the frequency differences shown in the lower-left panel of Figure 5 occurred for m-values near -300 and +300, we initially concentrated on the leakage matrices for the modes $(n, l, m) = (2, 600, -300)$ and $(2, 600, +300)$. We found that the two corresponding m-averaged leakage matrices appeared to be mirror images on each other, as shown in the upper-left panel of Figure 5. Both of these two m-averaged leakage matrices were dominated by a single large sidelobe. The near-mirror symmetry of these two m-averaged leakage matrices appeared to be correlated with the signs of the two extreme frequency differences shown in the lower-left panel of Figure 5. To quantify this idea, we numerically integrated each m-averaged leakage matrix and computed the value of $\Delta l_{\mathrm{bis}} = l_{\mathrm{bis}} - l$ that bisected the area of that leakage matrix. We defined Δl_{bis} to be the location of the "area bisector" of that leakage matrix. In contrast to the integral values taken by l, the values of l_{bis} are generally real numbers. We computed the area bisectors for all 1201 of the m-averaged leakage matrices for the $(2, 600)$ multiplet and compared those area bisectors with the measured frequency differences. These area bisectors are shown as the green curve in the lower-left panel of Figure 5.

We repeated all of the above steps for both the $(2, 300)$ and $(2, 900)$ multiplets, and we found very similar shapes for $\delta\nu$ and for Δl_{bis}, with minima for $m/L < 0$ and maxima for $m/L > 0$, as we have shown in the two right-hand panels of Figure 5. The strong correlations between $\delta\nu$ and Δl_{bis} for all three multiplets are evident. In fact, the correlation coefficient for the $(2, 600)$ multiplet was 0.9977, while the correlation coefficients for the $(2, 300)$ and $(2, 900)$ multiplets were 0.9888 and 0.9856, respectively. The slightly smaller correlation coefficients for the latter two multiplets came about because the maximum and minimum Δl_{bis} values of the area bisectors were systematically shifted to nearby values of m/L in comparison with the extreme values of the measured frequency differences. These shifts in the locations of the maximum and minimum values of Δl_{bis} relative to the locations of the extreme values of $\delta\nu$ can be seen in the upper-right and the two lower panels
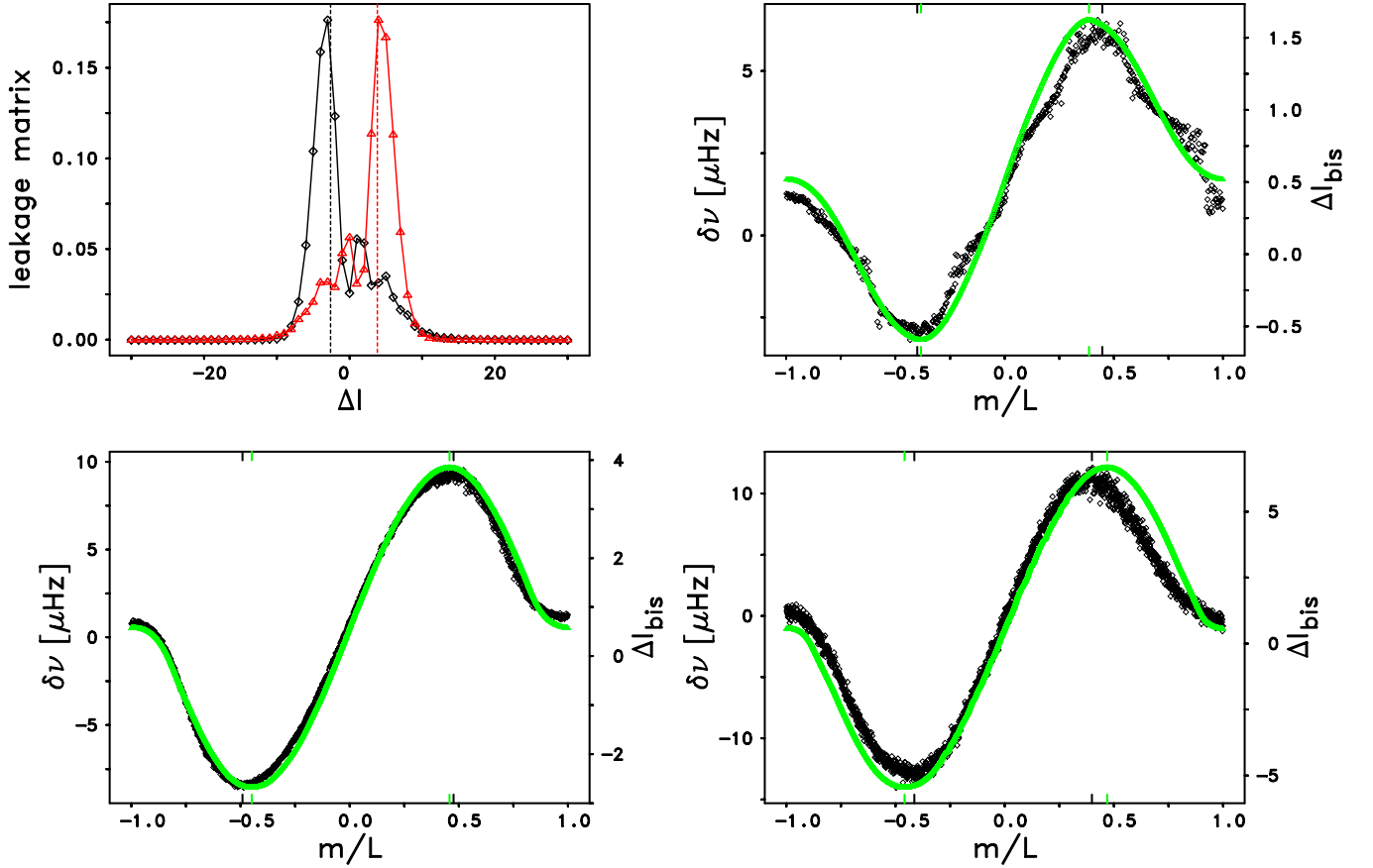
Figure 5. (Upper-left) Dependence of m-averaged leakage matrices for the modes $(n, l, m) = (2, 600, -300)$, shown in black, and $(2, 600, +300)$, shown in red, on the difference $\Delta l = l' - l$, where l' is the degree of the spatial side lobes. The vertical dashed lines indicate the locations $\Delta l_{\rm bis} = l_{\rm bis} - l$ of the corresponding area bisectors. (Upper-right) The black diamonds are for the frequency differences $\delta\nu = \nu_{\rm peak} - \nu_{\rm fit}$ as function of m/L for the $(2, 300)$ multiplet. Here, $\nu_{\rm peak}$ is the frequency for which the fitted profile takes its maximum value across the multiplet, $\nu_{\rm fit}$ is the fitted frequency, and $L^2 = l(l+1)$. The green triangles, which appear as a green line at the scale of the figure, give the locations $\Delta l_{\rm bis}$ of the area bisectors as a function of m/L. The left-hand pair of black tick marks located along the top and bottom axes shows the value of m/L at which the minimum value of the frequency difference, $\delta\nu_{\rm min}$, occurred, while the right-hand pairs of the black tick marks shows the value of m/L where the maximum frequency difference, $\delta\nu_{\rm max}$, occurred. The left-hand pair of green tick marks shows the value of m/L where the location of the area bisector reached its minimum value, $\Delta l_{\rm bis}^{\rm min} = l_{\rm bis}^{\rm min} - l$. The right-hand pair of green tick marks shows the value of m/L where the location of the area bisector reached its maximum value, $\Delta l_{\rm bis}^{\rm max} = l_{\rm bis}^{\rm max} - l$. The bottom panels are the same as the upper-right panel, but for the multiplets $(2, 600)$ (bottom-left) and $(2, 900)$ (bottom-right), respectively.

of Figure 5 as the shifts in the locations of the green tick marks relative to the black tick marks. For example, the locations of $\Delta l_{\rm bis}^{\rm min}$ shifted leftward relative to the black curve as the degree of the multiplets increased, while the locations of $\Delta l_{\rm bis}^{\rm max}$ shifted rightward as the degree increased.

In addition to the $(2, 300)$, $(2, 600)$, and $(2, 900)$ modes, we computed all $2l + 1$ values of both $\delta\nu$ and $\Delta l_{\rm bis}$ for seven more modes along the $n = 0$ ridge ranging between $l = 400$ and $l = 1000$, for eight more modes along the $n = 1$ ridge ranging between $l = 300$ and $l = 1000$, for five additional modes along the $n = 2$ ridge ranging between $l = 400$ and $l = 996$, for six more modes along the

$n = 3$ ridge ranging between $l = 300$ and $l = 729$, and for five additional modes along the $n = 4$ ridge ranging between $l = 250$ and $l = 530$. These 34 modes define our set of sample multiplets of which we will make ample use in the remainder of Section 4.2.

After generating the $2l + 1$ values of $\delta\nu$ and Δl_{bis} for all of our 34 sample multiplets, we next identified the m-values that corresponded to the minimum and maximum values of $\delta\nu$ within each multiplet, which we defined to be $m_{\delta\nu}^{\min}$ and $m_{\delta\nu}^{\max}$, respectively. We also identified the m-values that corresponded to the minimum and maximum values of the area bisectors within each multiplet, which we defined as $m_{\mathrm{bis}}^{\min}$ and $m_{\mathrm{bis}}^{\max}$, respectively. As soon as we had identified all 34 pairs of $m_{\delta\nu}^{\min}$, $m_{\delta\nu}^{\max}$ and $m_{\mathrm{bis}}^{\min}$, $m_{\mathrm{bis}}^{\max}$, respectively, for each multiplet, we finally identified $\Delta m_{\delta\nu} = m_{\delta\nu}^{\max} - m_{\delta\nu}^{\min}$ and $\Delta m_{\mathrm{bis}} = m_{\mathrm{bis}}^{\max} - m_{\mathrm{bis}}^{\min}$.

In the left-hand panel of Figure 6 we show the dependence of Δm_{bis} on the degree, l. The values of Δm_{bis} for each of the five f- and p-mode ridges are shown with different colors, as described in the caption to this figure, but the n-dependence of these five curves was so small that the colors are nearly indistinguishable. The degree dependence of each of the five curves is nearly linear. In fact, the nearly identical degree dependencies of the five curves indicates that the separations of the m-values that correspond to the maximum and minimum values of the area bisectors is governed solely by the structure of the leakage matrices themselves. Ignoring the tiny differences between portions of some of the five curves, we fit a least-squares straight line to all 34 pairs of Δm_{bis} and l. The equation of the fit that resulted was simply $\Delta m_{\mathrm{bis}} = -71.107 + 1.0075\, l$ and the correlation coefficient was equal to 0.9987.
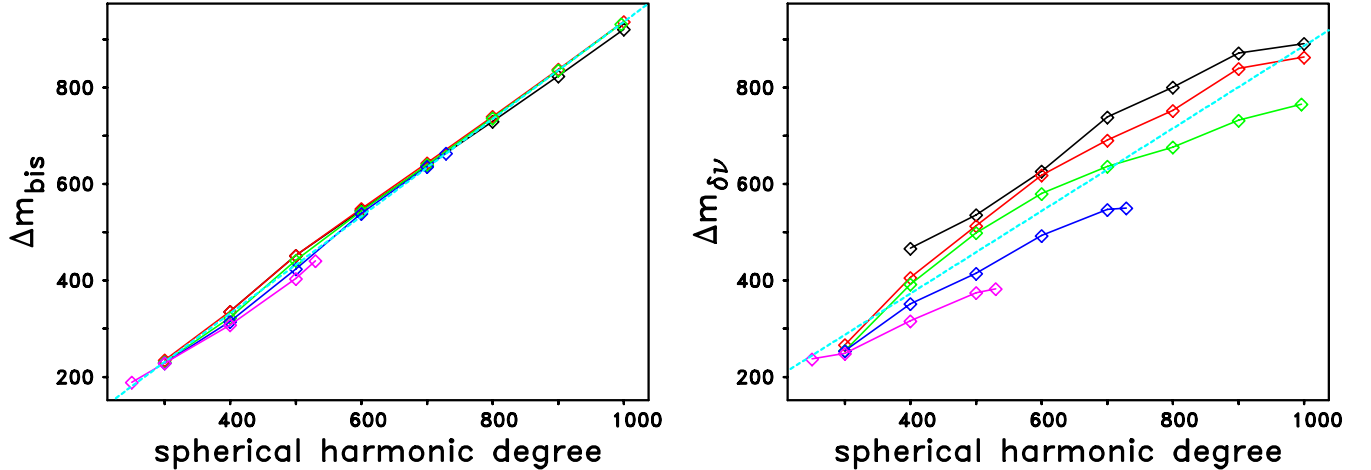
Figure 6. (Left) Dependence of Δm_{bis} on degree for the ridges $n = 0$ (black), $n = 1$ (red), $n = 2$ (green), $n = 3$ (blue), and $n = 4$ (pink). Also shown as the dashed turquoise line (even though it is nearly invisible) is the linear regression fit to all 34 pairs of points, the equation of which is given in the text. (Right) Dependence of $\Delta m_{\delta\nu}$ on degree for the same five ridges using the same color style as in the left-hand panel. Also shown as the dashed turquoise line is the linear regression fit to all 34 pairs of points. The equation of this line is given in the text.

In the right-hand panel of Figure 6 we show the dependence of $\Delta m_{\delta\nu}$ on the degree, l. While Δm_{bis} was primarily a function of l, the behavior of $\Delta m_{\delta\nu}$ is slightly more complicated in the sense that the five curves are not as linear as were the curves in the left-hand panel. Also, there is a definite difference in shape between each of the five curves. Clearly, something other than merely the

separations of the two extreme area bisectors is influencing the precise m-values where the $\delta\nu$-values exhibit their two extremes within each multiplet. This behavior is the reason for the systematic shifts in the locations of the green tick marks relative to the black tick marks in the upper-right and two lower panels of Figure 5. In spite of these systematic shifts in the values of $\Delta m_{\rm bis}$ and $\Delta m_{\delta\nu}$, the shifts are all small enough that they cause only minor differences in the values of the correlation coefficients that resulted from the 34 different regressions of $\delta\nu$ upon $\Delta l_{\rm bis}$. In only three of the 34 regression analyses was the value of the correlation coefficient less than 0.975.

When we carried out a linear regression analysis of $\Delta m_{\delta\nu}$ upon l, we obtained a linear fit that had a smaller slope than the fit that we showed in the left-hand panel of Figure 6, viz. $\Delta m_{\delta\nu} = 30.696 + 0.85589\, l$. The correlation coefficient for this fit was equal to 0.9493. Moreover, we realized that, because of the extremely tight dependence of $\Delta m_{\rm bis}$ on l that we showed in the left-hand panel of Figure 6, we could replace l as the independent variable with $\Delta m_{\rm bis}$. In fact, the regression of $\Delta m_{\delta\nu}$ upon $\Delta m_{\rm bis}$ gave practically identical regression coefficients and correlation coefficients.

Thus far, we have concentrated on the m-value separations of the two extreme values of $\delta\nu$ and $\Delta l_{\rm bis}$ within each multiplet. We also realized that the peak-to-peak frequency differences of the two extreme values of $\delta\nu$ within the multiplets was of great interest. We defined these peak-to-peak frequency differences as follows: $\Delta(\delta\nu) = \delta\nu_{\rm max} - \delta\nu_{\rm min}$, where $\delta\nu_{\rm min}$ and $\delta\nu_{\rm max}$ are the frequencies for which $\delta\nu = \nu_{\rm peak} - \nu_{\rm fit}$ takes its minimum and maximum value, respectively, across the multiplet. We illustrate the dependence of $\Delta(\delta\nu)$ on l in the upper-left panel of Figure 7. This panel shows that $\Delta(\delta\nu)$ increased nearly linearly with increasing degree, but it also shows a weak dependence on n as well. In order to see if we could find a single parameter that would remove this weak dependence on n, we also computed the degree separations of the two extreme area bisectors for each multiplet. We defined this separation to be $\Delta(\Delta l_{\rm bis}) = \Delta l_{\rm bis}^{\rm max} - \Delta l_{\rm bis}^{\rm min} = (l_{\rm bis}^{\rm max} - l) - (l_{\rm bis}^{\rm min} - l) = l_{\rm bis}^{\rm max} - l_{\rm bis}^{\rm min}$. Here, $\Delta l_{\rm bis}^{\rm min}$ and $\Delta l_{\rm bis}^{\rm max}$ are the minimum and maximum locations of the area bisectors, respectively, across the multiplet.

We show the dependence of $\Delta(\Delta l_{\rm bis})$ on l in the upper-right panel of Figure 7. This panel shows that $\Delta(\Delta l_{\rm bis})$ varied in roughly a quadratic manner with increasing l. This panel also shows that there was a systematic dependence of $\Delta(\Delta l_{\rm bis})$ on the n-value of the ridge. The fact that the degree dependencies of both $\Delta(\delta\nu)$ and $\Delta(\Delta l_{\rm bis})$ were substantially larger than were the differences between the five curves suggested to us that the separation in the locations of the two extreme area bisectors within each multiplet was the primary cause of the measured frequency differences. We found this to be the case, as we illustrate in the lower-left panel of Figure 7, in which we have plotted $\Delta(\delta\nu)$ as a function of $\Delta(\Delta l_{\rm bis})$. This panel shows a very tight distribution of points for $\Delta(\Delta l_{\rm bis}) \leq 12$. Furthermore, all but three of the points appeared to demonstrate a parabolic variation with $\Delta(\Delta l_{\rm bis})$. We then carried out a least-squares polynomial fit to the 34 data points, and we obtained a parabolic fit that had only three substantial outliers, as is shown in the lower-right panel of Figure 7. A comparison of the two panels of Figure 6 and the lower-right panel of Figure 7 shows that, while some aspect of the leakage matrices other than the locations of the area bisectors determines the $\Delta m_{\delta\nu}$ values of the two extreme values of $\delta\nu$, these bisector separations do explain the peak-to-peak amplitudes of the frequency differences quite well by themselves.

4.2.2. *Effects of leakage matrices on ridge shapes*

We have already pointed out that all four of the fitted profiles that we included in Figure 4 for the $(2, 600)$ multiplet showed lower levels of power on their high-frequency ends. In order to determine if
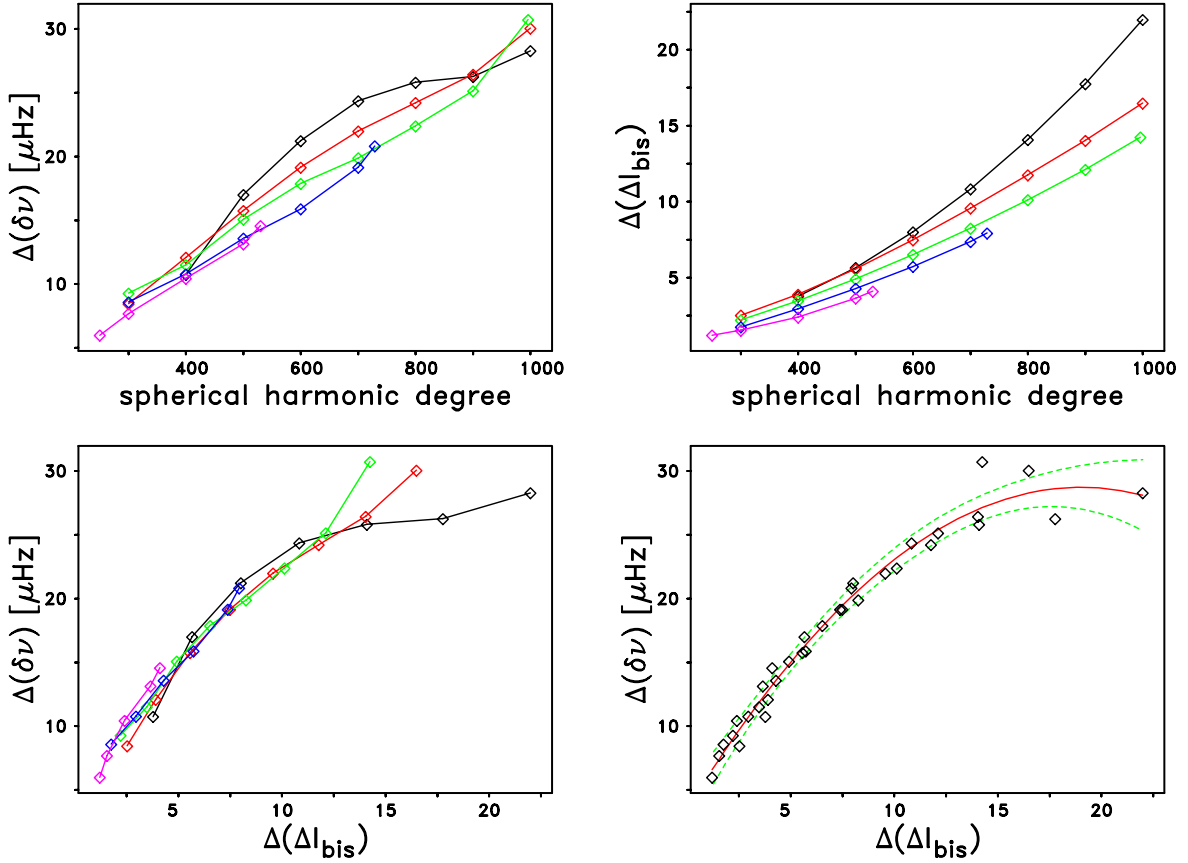
Figure 7. (Upper-left) Frequency differences $\Delta(\delta\nu)$ as function of degree for the ridges $n = 0$ through $n = 4$ using the same color style as in Figure 6. (Upper-right) Dependence of $\Delta(\Delta l_{\mathrm{bis}})$ on degree for the ridges $n = 0$ through $n = 4$ using the same color style as in the upper-left panel. (Lower-left) Dependence of $\Delta(\delta\nu)$ on $\Delta(\Delta l_{\mathrm{bis}})$ for all five ridges using the same color style as in both upper panels. The five curves overlap closely for $\Delta(\Delta l_{\mathrm{bis}}) \leq 12$. (Lower-right) The same 34 data points are repeated in this panel but without any differentiation between the ridges that each group of points corresponded to. Also shown as the red curve is the unweighted least-squares parabolic fit to all 34 data points. The two dashed green curves are the $\pm 3\,\sigma$ confidence limits to this fit. Only a few of the 34 points lie outside these limits.

these sample profile shapes were representative of the remaining 1197 profiles in this multiplet, and to see how the shapes of all of the profiles for this multiplet compared with the shapes of the fitted profiles for our 33 other sample multiplets, we chose to employ a standard statistical measure of asymmetry of a distribution, which is the skewness. The skewness, $\mathcal{S}$, of the fitting profile $M_{n,l,m}(\nu, \boldsymbol{p})$, as given in Equation (1), is given by

$$\mathcal{S} = -\frac{\mathcal{I}_3}{\mathcal{I}_2^{3/2}}. \tag{37}$$

Here,

$$\mathcal{I}_2 = \int\limits_{-\infty}^{\infty} (\nu - \nu_{\mathrm{ave}})^2\, \tilde{M}(\nu)\, \mathrm{d}\nu, \quad \mathcal{I}_3 = \int\limits_{-\infty}^{\infty} (\nu - \nu_{\mathrm{ave}})^3\, \tilde{M}(\nu)\, \mathrm{d}\nu, \quad \nu_{\mathrm{ave}} = \int\limits_{-\infty}^{\infty} \nu\, \tilde{M}(\nu)\, \mathrm{d}\nu, \tag{38}$$

and

$$\tilde{M}(\nu) = \frac{M_{n,l,m}(\nu, \boldsymbol{p})}{\int\limits_{-\infty}^{\infty} M_{n,l,m}(\nu, \boldsymbol{p})\, \mathrm{d}\nu} \tag{39}$$

is the normalized fitting profile. The infinite integrals in Equations (38) and (39) are approximated by integrations over the corresponding fitting boxes using the trapezoidal rule. For brevity we omitted in $\tilde{M}(\nu)$ both the subscripts as well as the fitting vector $\boldsymbol{p}$. We note that for reasons that will become evident below, we have chosen to define the skewness of the fitted profiles in Equation (37) as the negative of the commonly-used definition.

When we computed the skewnesses for all 1201 of the fitted profiles for the $(2, 600)$ multiplet, we found that they were all positive, and hence we confirmed that the four profiles shown in Figure 4 were indeed representative of this entire multiplet. We also found that the skewnesses of these fitted profiles varied in a systematic manner as a function of the m-value of the profile. In particular, the skewnesses were strongly correlated with the 1201 frequency differences, $\delta\nu$, for this multiplet. These skewnesses are shown as the set of blue triangles in the left-hand panel of Figure 8. We have also included in this panel the same set of frequency differences that we illustrated for this multiplet in the bottom-left panel of Figure 5 as the set of black diamonds. Clearly, the skewnesses, as we have defined them, were correlated with the frequency differences. On the other hand, had we adopted the standard definition of the skewness in Equation (37), the skewnesses would have been anti-correlated with the frequency differences in both panels of Figure 8, and the relationships between the maxima and minima of both the skewnesses and the frequency differences would have been more difficult to demonstrate. It is also clear that the skewnesses were noisier than were the frequency differences for this multiplet. Furthermore, the two extreme values of the skewnesses were shifted to different values of m than were the two extreme values of $\delta\nu$. We have highlighted these shifts within the $(2, 600)$ multiplet by including the two pairs of black and red tick marks along the top and bottom axes of this panel. The black tick marks are located at exactly the same values of m/L as were the black tick marks in the bottom-left panel of Figure 5. In order to compare the m-values of the maxima and minima of the skewnesses with the m-values of the extreme values of $\delta\nu$, we first fit statistically-significant polynomials to each of the 1201 sets of skewness for this multiplet. The degree of these polynomials was determined in each case by means of the R-statistic, as given in Equation (22). We chose to fit each of these distributions of points with polynomials because of the noisier nature of the skewnesses. The fitted polynomial for the $(2, 600)$ multiplet is shown as the red curve in this same left-hand panel of Figure 8. The two m-values where this polynomial exhibited its maximum and minimum are shown as the two pairs of red tick marks. This panel shows that the two extreme values of the skewness were shifted toward smaller values of m (i.e., toward $m/L = 0$) in comparison with the extreme values of the frequency differences. Similarly, by comparing the locations of the red tick marks in this panel with the locations of the green tick marks in the bottom-left panel of Figure 5, it is also clear that the two extreme values of the skewnesses were shifted with respect to the locations of the maxima and minima of the locations of the area bisectors.

To illustrate that the correlation of the skewnesses and the frequency differences was a common occurrence for the other multiplets, we show the frequency differences, the skewnesses, and the fitted polynomial for the $(2, 900)$ multiplet in the right-hand panel of Figure 8. It is clear that for this particular multiplet, the skewnesses and the frequency differences were even more tightly correlated
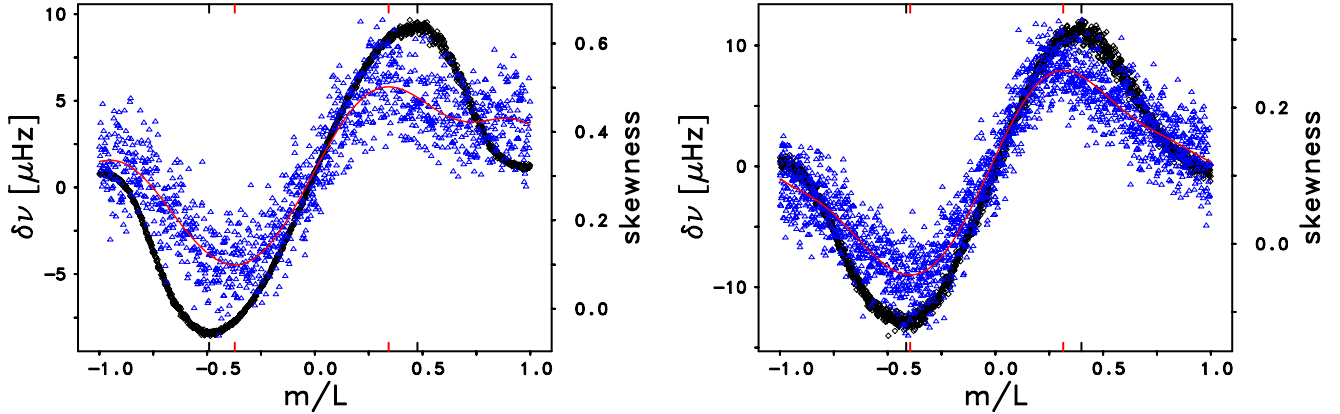
Figure 8. (Left) Dependence of the frequency differences $\delta\nu$, shown as the black diamonds, on m/L for the $(2, 600)$ multiplet. The blue triangles give the locations of the skewness of the profiles fitted to the 1201 modes comprising this multiplet. The red line represents a statistically-significant polynomial fitted to the skewnesses. The left-hand pair of black tick marks located along the top and bottom axes shows the value of m/L at which the minimum value of $\delta\nu$ occurred, while the right-hand pairs of the black tick marks shows the value of m/L where the maximum value of $\delta\nu$ occurred. The left-hand pair of red tick marks shows the location of the rightmost minimum of the fitted polynomial that occurred for $m/L < 0$. The right-hand pair of red tick marks shows the location of the leftmost maximum of the fitted polynomial that occurred for $m/L > 0$. (Right) Same as the left panel, but for the $(2, 900)$ multiplet.

than in the case of the $(2, 600)$ multiplet. This can be seen in this panel by looking at the locations of the red and black tick marks. To study the extent to which the leakage matrices might govern the shapes of the fitted profiles, we computed the separations of the m-values for the two extreme values of the skewness for each of our other 33 sample multiplets. We defined these m-value separations as $\Delta m_{\mathrm{skew}} = m_{\mathrm{skew}}^{\max} - m_{\mathrm{skew}}^{\min}$, where $m_{\mathrm{skew}}^{\max}$ represents the m-value where the skewness reached its maximum value in this multiplet and where $m_{\mathrm{skew}}^{\min}$ represents the m-value where the skewness reached its minimum value. We then compared all 34 values of Δm_{skew} with the 34 corresponding values of Δm_{bis}. The results of this comparison are shown in the left-hand panel of Figure 9, which shows a very tight correlation in the two sets of Δm. We have also included the least-squares linear regression fit to all 34 pairs of points as the dashed turquoise line. The equation of this regression fit was $\Delta m_{\mathrm{skew}} = 27.727 + 0.74012\,\Delta m_{\mathrm{bis}}$, and the correlation coefficient was 0.9932. The high value of the correlation coefficient for this fit shows clearly that the separation of the two extreme m-values of the area bisectors within each multiplet was the primary cause of the m-separations of extreme values of the skewness of the fitted profiles. The leakage matrices had the dominant influence on the shapes of the fitted profiles, just as they were the dominant cause of the differences between the frequencies of the peaks of those profiles and the fitted frequencies that the MPTS method computed for each of those multiplets.

We have already noted that the skewnesses were somewhat noisier than were the differences between the frequencies of the peaks of the fitted profiles and the fitted frequencies that the MPTS method produced, and we have also pointed out that the m-values of the extreme values of those skewnesses were shifted relative to the m-values of the extreme values of the frequency differences. Both of these effects weakened the strength of the correlation between the skewnesses and the separations in the locations of the extreme area bisectors, Δl_{bis}, as we show in the right-hand panel of Figure 9. In this panel we are showing the degree dependence of these 34 correlation coefficients as the five
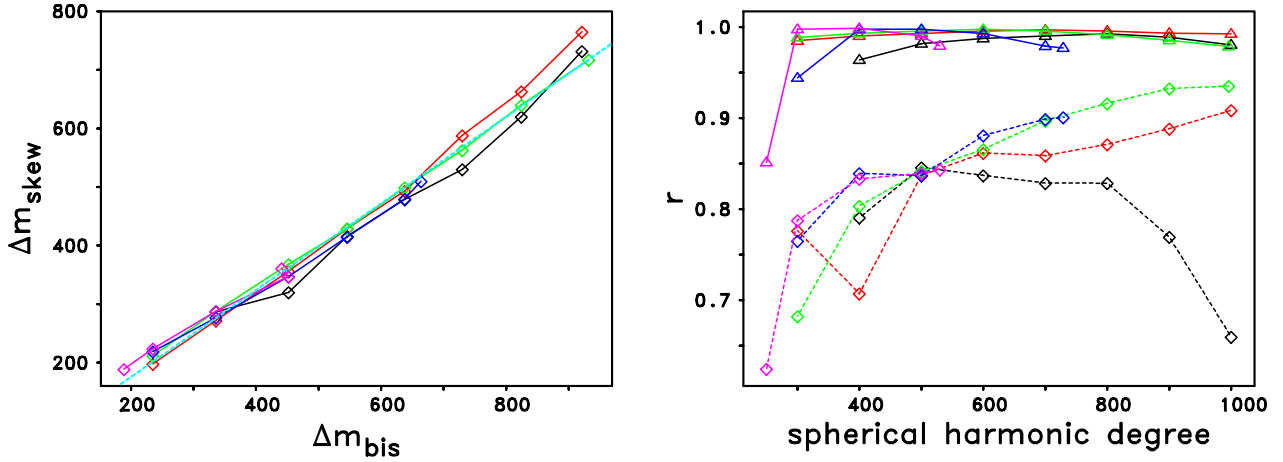
Figure 9. (Left) Dependence of $\Delta m_{\rm skew}$ on $\Delta m_{\rm bis}$ for the ridges $n = 0$ through $n = 4$ using the same color style as in Figure 6. Also shown as the dashed turquoise line is the linear regression fit to all 34 pairs of points. The equation of this line is given in the text. (Right) The triangles connected with full lines represent the correlation coefficient, r, between the frequency differences $\delta\nu$ and the separations in the locations of the two extreme area bisectors $\Delta l_{\rm bis}$ for the ridges $n = 0$ through $n = 4$ as function of the spherical harmonic degree. The diamonds connected with dashed lines represent the correlation coefficient, r, between the skewnesses and $\Delta l_{\rm bis}$ for the same set of ridges as function of the spherical harmonic degree. The color style used in this panel is the same as in the left panel.

sets of diamonds. While these correlation coefficients ranged from 0.6245 to 0.9353, they were all systematically smaller than were the 34 corresponding correlation coefficients that resulted from the regressions of the frequency differences upon $\Delta l_{\rm bis}$. Those 34 correlation coefficients are shown in the same panel as the five sets of triangles. With the exception of the $n = 0$ ridge, the correlation coefficients from the regressions of the skewnesses upon $\Delta l_{\rm bis}$ were increasing with increasing degree, l, just as we previously showed in the two panels of Figure 8, where the skewnesses (the blue triangles) could be seen to correlate more closely with the frequency differences (the black diamonds) for the higher-degree $(2, 900)$ multiplet that we showed in the right-hand panel than they did for the lower-degree $(2, 600)$ multiplet that we showed in the left-hand panel. By contrast, most of the correlation coefficients from the $\delta\nu$ versus $\Delta m_{\rm bis}$ regressions were so close to unity that they showed little variation with l.

In addition to studying the influence that the separations of the area bisectors had on the separations in the m-values of the maximum and minimum values of the skewness within each of our 34 sample multiplets, we also wanted to learn what parameter most influenced the extreme values of the skewnesses themselves. To do so, we defined the difference in the two extreme values of the skewness as follows: $\Delta\,{\rm skew} = {\rm skew}_{\rm max} - {\rm skew}_{\rm min}$, where ${\rm skew}_{\rm max}$ represents the maximum value of the skewness within a given multiplet and ${\rm skew}_{\rm min}$ represents the minimum value of the skewness in that multiplet. We next analyzed the 34 values of $\Delta\,{\rm skew}$ as functions of l, $\Delta(\Delta l_{\rm bis})$, and ν, and we found that the tightest relationship was the one between $\Delta\,{\rm skew}$ and ν. We show the results of this comparison for all 34 multiplets in Figure 10. With the exception of the discordant point at the low-frequency end of the $n = 1$ ridge, all of the other 33 values of $\Delta\,{\rm skew}$ showed a well-defined variation with the frequency of the multiplet. This variation is similar to that of the p-mode amplitudes, and
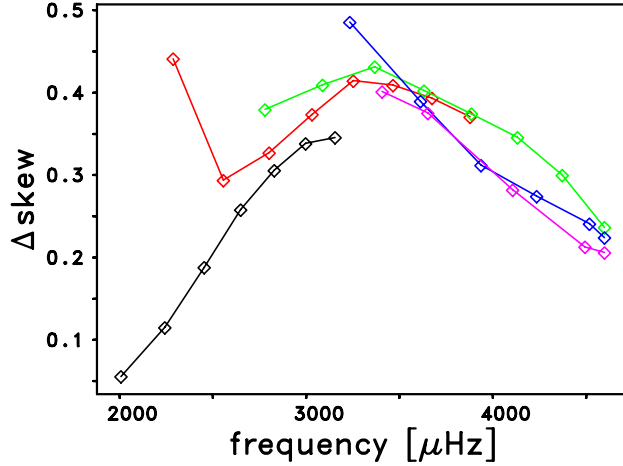
Figure 10. Frequency dependence of the peak-to-peak difference in the skewness, Δ skew, for each of our 34 multiplets. The color style is the same as in both panels of Figure 9.

hence the modal amplitudes may be influencing the maximum and minimum values of the skewness within each multiplet.

4.2.3. *Effects of leakage matrices on ridge widths and line widths*

In addition to allowing us to improve our understanding of the frequency pulling effects of the wide ridges of observed power of the higher-degree f- and p-modes, the fitted profiles that the MPTS method generated also allowed us to investigate the variation in the widths of the fitted profiles across each of our 34 sample multiplets. In order to study these variations, we first had to define the full-width-at-half-maximum of each of the fitted profiles. We began this process by first identifying the two frequencies located on either side of the peak of each profile at which that profile had dropped to one-half of its peak amplitude, which we defined to be $\nu_{0.5}^{\text{high}}$ and $\nu_{0.5}^{\text{low}}$, respectively. Because of the asymmetry of the fitted profiles, as we discussed earlier, these two frequencies were not symmetrically located about the peak frequency of the ridge, ν_{peak}. We then identified the full-width-at-half-maximum for each ridge, which we designated by $\text{FWHM}_{\text{ridge}}$, by simply subtracting these two frequencies, so that $\text{FWHM}_{\text{ridge}} = \nu_{0.5}^{\text{high}} - \nu_{0.5}^{\text{low}}$. We then plotted all $2l + 1$ values of $\text{FWHM}_{\text{ridge}}$ for all 34 multiplets.

After creating these 34 plots, we quickly determined that $\text{FWHM}_{\text{ridge}}$ exhibited a systematic variation across each multiplet in which local minima of the ridge widths occurred at, or close to, both sectoral modes and also for modes close to the zonal mode. In between these three local minima, we found that the ridge widths exhibited local maxima near m/L values that ranged from roughly ± 0.55 to ± 0.75. We show two different sets of ridge widths as the green symbols in the two panels of Figure 11 for the $(2, 300)$ and $(2, 600)$ multiplets, respectively. In each panel of this figure we have included the statistically-significant polynomial fit to all $2l + 1$ values as the magenta curve. In each case the degree of the fitted polynomial was determined by means of the R-statistic, as given in Equation (22). These polynomial fits allowed us to compare the average value of the two peaks in the ridge widths with the overall average values of the ridge widths over each of the 34 multiplets. They also allowed us to determine the values of m at which the extreme widths were located for each multiplet.

We have previously defined the line width, w, in Equation (2) in Section 3.1. The two sets of line widths for the $(2, 300)$ and $(2, 600)$ multiplets are shown as the two sets of black diamonds in the two panels of Figure 11. The most obvious differences that we found between the two sets of line and ridge widths at moderate degrees, such as that of the $(2, 300)$ multiplet shown in the left-hand panel of Figure 11, was that the ridge widths were considerably larger than were the line widths. For example, for the $(2, 300)$ multiplet the average ridge width was equal to $14.7\,\mu$Hz, while the average line width was only equal to $7.0\,\mu$Hz. As the degree of the multiplets was increased, we found that, while both the ridge widths and the line widths increased, the line widths increased more rapidly than did the ridge widths, so that by $l = 600$ the average ridge width had increased to $36.2\,\mu$Hz, while the average line width had increased to $28.6\,\mu$Hz, as shown in the right-hand panel of Figure 11. For even higher degrees, the systematic differences in the two sets of widths had decreased to a few percent.

Even though the sets of the line widths looked approximately constant across the lower-degree multiplets, we found that, as the degree increased, the line widths also began to show some systematic variation, albeit at a much-reduced level than for the corresponding ridge widths. Hence, we also fit polynomials to all 34 sets of $2l + 1$ line widths, the degrees of which were determined by means of the R-statistic, as given in Equation (22). Two sample polynomial fits to the line widths are shown as the blue curves in both panels of Figure 11. When we examined these two polynomials closely, we found that both of them appeared to be roughly inverted in comparison to the fits to the corresponding ridge widths. Where the ridge widths exhibited minima, the line widths exhibited weak maxima and vice versa. The local minima in the line widths were not located at exactly the same values of m as were the local maxima in the ridge widths, but they were located close to those values of m.
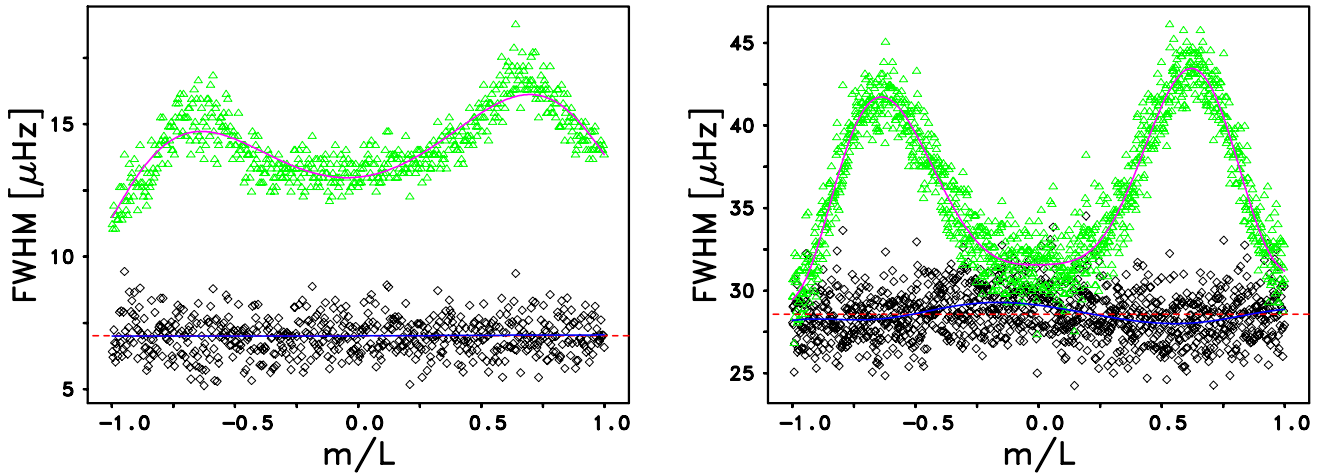

Figure 11. (Left) The green triangles represent the full-width-at-half-maximum, FWHM$_{\text{ridge}}$, of each of the $2l + 1$ fitted profiles for the $(2, 300)$ multiplet. A statistically-significant polynomial fit to all 601 values is shown as the magenta curve. The black diamonds represent the set of line widths that the MPTS method produced for this multiplet. The statistically-significant polynomial fit to this set of line widths is shown as the blue curve, which obviously is nearly identical to the line width of this multiplet, as computed from Equation (28) by the MPTS method and shown as the dashed horizontal red line. (Right) Same as left panel, but for the $(2, 600)$ multiplet. The variation of both the line width and the ridge width across this multiplet is much larger than across the $(2, 300)$ multiplet shown in the left panel.

In order to evaluate the statistical significance of the apparent anti-correlation of the pair of poly-nomials shown in the right-hand panel of Figure 11, we carried out a total of 34 linear regression analyses in which we regressed the ridge-width polynomial fits upon the line-width fits for all of our sample multiplets. We found that, for 29 of our 34 multiplets, the correlation coefficients were negative, and hence the anti-correlation shown in the right-hand panel of Figure 11 was indeed rep-resentative of the vast majority of the multiplets. Also, all of the negative correlation coefficients were significant at better than the 99 percent confidence limit.

In order to study the influence of the leakage matrices on the separations in the m-values of the maximum values of the ridge widths, we defined these separations as follows: $\Delta m_{\mathrm{FWHM}}^{\mathrm{ridge}} = m_{\mathrm{FWHM}}^{\mathrm{ridge}}(\mathrm{max,right}) - m_{\mathrm{FWHM}}^{\mathrm{ridge}}(\mathrm{max,left})$, where, $m_{\mathrm{FWHM}}^{\mathrm{ridge}}(\mathrm{max,left})$ and $m_{\mathrm{FWHM}}^{\mathrm{ridge}}(\mathrm{max,right})$ refer to the m-values of the left-hand and right-hand peaks of the polynomial fit to each set of ridge widths, respectively. For only two of the 34 sample multiplets were we unable to fit a significant polynomial to the distribution of ridge widths. These two exceptions were the $(0, 400)$ and the $(4, 250)$ multiplets. In both cases $\mathrm{FWHM}_{\mathrm{ridge}}$ did not show pronounced maxima within each multiplet. When we compared all 32 values of $\Delta m_{\mathrm{FWHM}}^{\mathrm{ridge}}$ with their corresponding values of Δm_{bis}, we found yet another example of a tight correlation between these two m-value separations, as shown for all five of the f- and p-mode ridges in the left-hand panel of Figure 12. The correlation between these two m-value separations was strong enough that we computed the least-square linear regression fit to all 32 pairs of points. The equation of this fit was $\Delta m_{\mathrm{FWHM}}^{\mathrm{ridge}} = 67.371 + 1.1219\,\Delta m_{\mathrm{bis}}$, and the correlation coefficient was equal to 0.9849.

In order to study the influence of the leakage matrices on the separations in the m-values of the minimum values of the line widths, we defined these separations as follows: $\Delta m_{\mathrm{FWHM}}^{\mathrm{line}} = m_{\mathrm{FWHM}}^{\mathrm{line}}(\mathrm{min,right}) - m_{\mathrm{FWHM}}^{\mathrm{line}}(\mathrm{min,left})$, where $m_{\mathrm{FWHM}}^{\mathrm{line}}(\mathrm{min,left})$ and $m_{\mathrm{FWHM}}^{\mathrm{line}}(\mathrm{min,right})$ refer to the m-values of the left-hand and right-hand minimum of the polynomial fit to each set of line widths, respectively. In the case of the line widths there were six multiplets which did not show definable minima when we fit the polynomials to those sets of line widths. When we compared all 28 of the re-
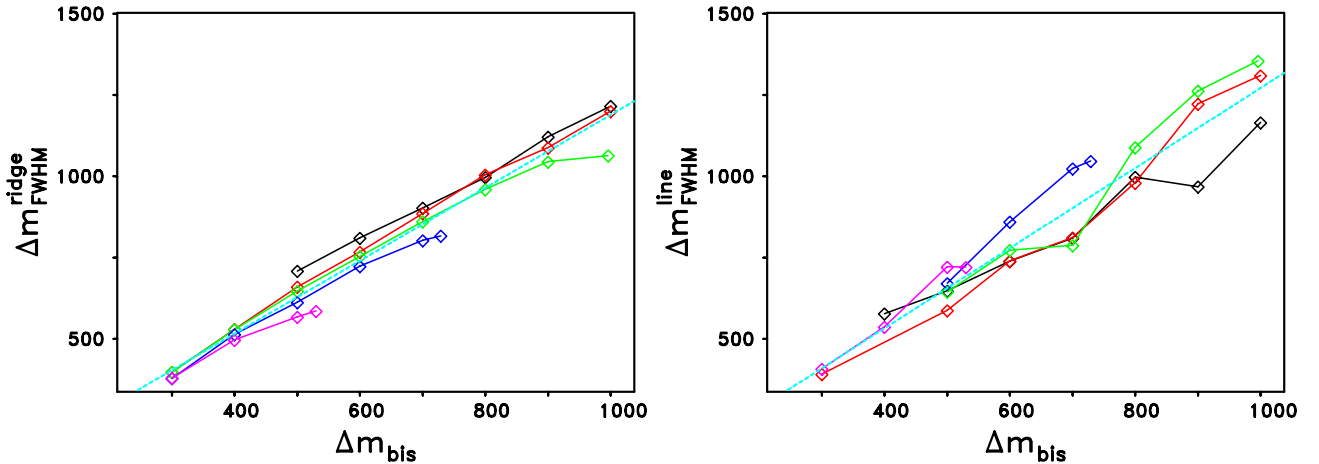

Figure 12. (Left) Dependence of $\Delta m_{\mathrm{FWHM}}^{\mathrm{ridge}}$ on Δm_{bis} for the ridges $n = 0$ through $n = 4$ using the same color style as in Figure 6. Also shown as the dashed turquoise line is the linear regression fit to all 32 pairs of points. The equation of this line is given in the text. (Right) Dependence of $\Delta m_{\mathrm{FWHM}}^{\mathrm{line}}$ on Δm_{bis} for the same five ridges using the same color style as in the left-hand panel. Also shown as the dashed turquoise line is the linear regression fit to all 28 pairs of points. The equation of this line is given in the text.

maining values of $\Delta m^{\text{line}}_{\text{FWHM}}$ with their corresponding values of Δm_{bis}, we found yet another example of a tight correlation between these two m-value separations, as shown for all five of the f- and p-mode ridges in the right-hand panel of Figure 12. The correlation between these two m-value separations was strong enough that we computed the least-square linear regression fit to all 28 pairs of points. The equation of this fit was $\Delta m^{\text{line}}_{\text{FWHM}} = 40.503 + 1.2312\,\Delta m_{\text{bis}}$, and the correlation coefficient was equal to 0.9574. The similarity of both slopes of these two linear regression fits to the slopes of the fits shown in Figures 6 and 9 clearly demonstrates that the leakage matrices governed the m-value separations of both the ridge widths and the line widths.

4.2.4. *Effects of leakage matrices on asymmetries*

In order to determine whether the leakage matrices had any effects on the line asymmetries that are computed by the MPTS method within our sample multiplets, we first plotted all $2l+1$ values of $B_{n,l,m}$ within each multiplet as a function of m/L. We show two of these 34 plots in Figure 13. In the left-hand panel of Figure 13 we show the line asymmetries for the $(0, 600)$ multiplet. We also show the statistically-significant polynomial that we fit to the values of $B_{n,l,m}$ as the nearly horizontal red curve, the degree of which was determined by means of the R-statistic (cf. Equation (22)). For this low-order multiplet the noise in the asymmetries dominated over any systematic effects of the leakage matrices. This situation changed as the n-value of the multiplets increased, as we show in the right-hand panel of Figure 13 for the $(4, 500)$ multiplet. In this case the statistically-significant polynomial fit that is shown by the red curve shows a two-peaked structure very similar to the structure of the polynomials that we fit to the ridge widths in Figure 11. In addition to the double-peaked nature of the curve, this fit also shows an overall slope that is downward toward positive values of m/L. Such an overall slope is a feature that was shared by many of the other multiplets including the $(2, 900)$ multiplet that is shown in the bottom-right panel of Figure 17.
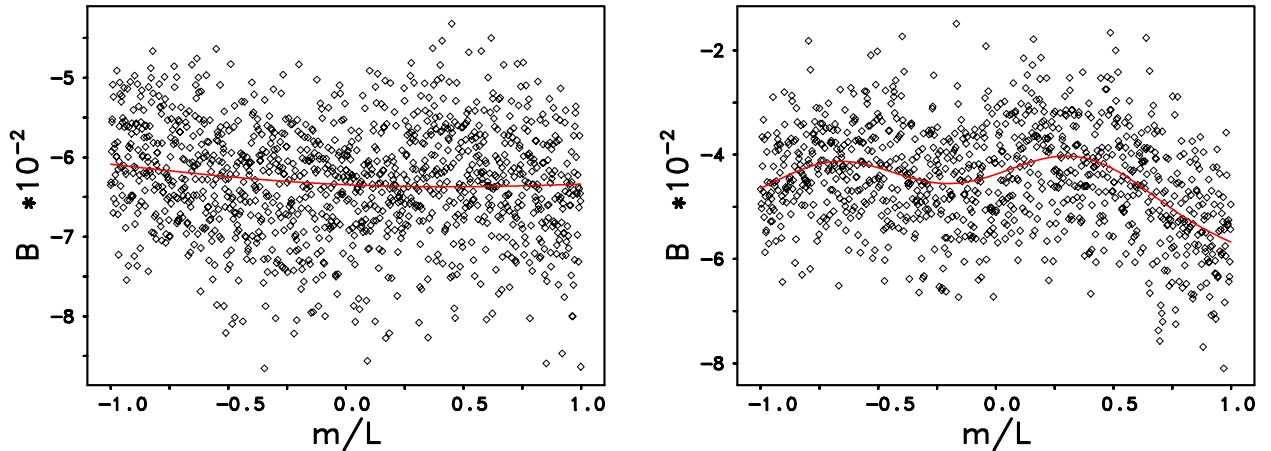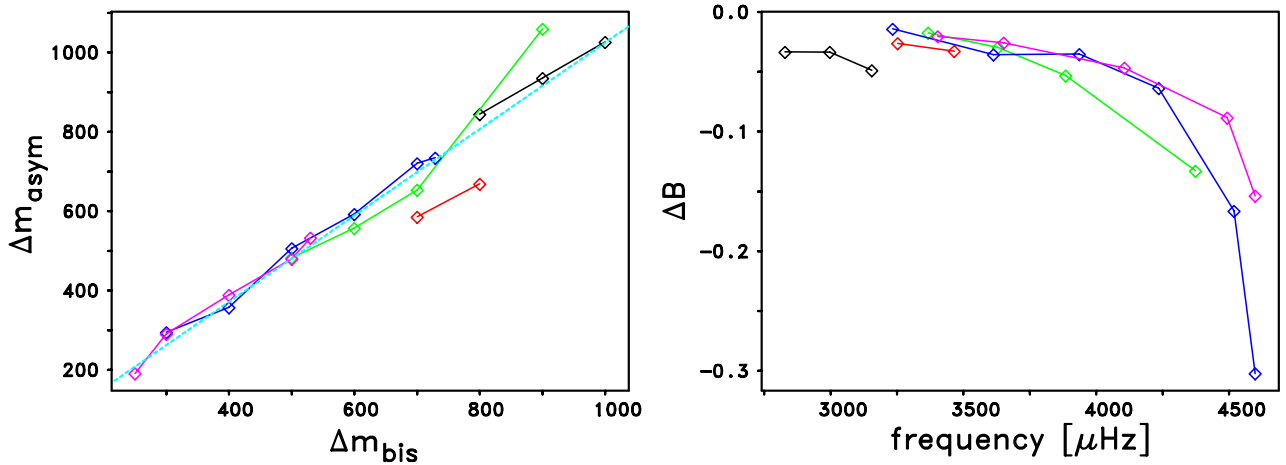

Figure 13. (Left) Dependence of the line asymmetries $B_{n,l,m}$, shown as the black diamonds, on m/L for the $(0, 600)$ multiplet. The red line represents a statistically-significant, nearly horizontal polynomial. (Right) Same as the left panel, but for the $(4, 500)$ multiplet. For this multiplet the fitted polynomial exhibits a double-peaked structure with a decline towards the right edge.

The two polynomial fits that are shown in Figure 13 are clearly quite different. When we computed similar polynomials for the other 32 multiplets, we found that we could see a two-peaked structure

similar to that shown for the $(4, 500)$ multiplet in the right-hand panel of Figure 13 for only 19 other multiplets. The other 14 multiplets had fits that showed only a single peak for $m/L > 0$ or else they showed no obvious peaks at all like the fit to the $(0, 600)$ multiplet shown in the left-hand panel of Figure 13. For the 20 multiplets which did show a double-peaked structure of the fitted polynomials, we identified the m-values that corresponded to both of these peaks and we then defined the separation in these two m-values as $\Delta m_{\rm asym} = m_{\rm asym}({\rm max, right}) - m_{\rm asym}({\rm max, left})$, where $m_{\rm asym}({\rm max, left})$ represents the m-value of the left-hand peak and $m_{\rm asym}({\rm max, right})$ represents the m-value of the right-hand peak. We show the dependence of $\Delta m_{\rm asym}$ on $\Delta m_{\rm bis}$ in the left-hand panel of Figure 14. We have also shown the least-squares fit that we computed for the 20 multiplets that had a double-peaked structure of their polynomial fits as the turquoise straight line. The equation for this linear fit was $\Delta m_{\rm asym} = -63.762 + 1.0890\,\Delta m_{\rm bis}$ and the correlation coefficient for this fit was 0.9719. As was the case with the frequency differences, the skewnesses, the ridge widths and the line widths, this rather tight linear fit demonstrates that the leakage matrices also dominated the separations of the m-values of the local peaks of the asymmetries in 20 of our sample multiplets.

Figure 14. (Left) Dependence of $\Delta m_{\rm asym}$ on $\Delta m_{\rm bis}$ for the ridges $n = 0$ through $n = 4$ using the same color style as in Figure 6. Also shown as the dashed turquoise line is the linear regression fit to all 20 pairs of points. (Right) Frequency dependence of ΔB. The color style is the same as in the left-hand panel.

To determine the amount of variation that the leakage matrices introduced into the line asymmetries themselves, we first determined the values of the two peaks of the fitted polynomials for the 20 multiplets which demonstrated a two-peaked structure, and we defined those two values as $B({\rm max, left})$ and $B({\rm max, right})$, where we have suppressed the subscripts n, l, and m for clarity. We next defined the normalized ratio $\Delta B = \delta B/\langle B \rangle$, where $\delta B = (1/2) * \left[B({\rm max, left}) + B({\rm max, right})\right] - \langle B \rangle$, where $\langle B \rangle$ represents the average of the $2l + 1$ line asymmetries in the multiplet. We show the frequency dependence of ΔB in the right-hand panel of Figure 14. This panel illustrates that ΔB decreased as a function of frequency to around 30 percent for the highest frequency multiplet that we studied. This panel confirms the differences in the structure of the two polynomial fits that were shown in Figure 13.

4.2.5. *Comparison of leakage matrix effects on multiplet parameters*

In this section, we will compare the results of the four previous Sections 4.2.1 through 4.2.4. In Figures 5, 8, 11, and 13, we plotted the frequency differences, the area bisectors, the skewnesses, the ridge widths, the line widths, and the asymmetries, respectively, as functions of m/L. Here, in Figure 15, we will instead show the same six variables as functions of m alone for the $(2, 600)$ multiplet. The ordering in which we plotted the six curves is described in the caption of Figure 15 and is chosen so that the systematic decrease in the m-separation, Δm, of the two extreme values of each curve is emphasized as we go downward from panel to panel. For the two sets of widths and for the asymmetries, the two extreme values are both local maxima, while for $\delta \nu$, Δl_{bis}, and for the skewnesses, the left-hand extrema (i.e., the ones for which $m < 0$), were all local minima and the right-hand extrema (i.e., the ones for $m > 0$), were all local maxima. We have also inserted the two sloping dashed lines as guides to highlight the systematic changes in the different values of Δm as we go from the top panel to the bottom one. The left-hand dashed line was drawn to pass through the m-value of the left-hand peak of the inverted line-width polynomial, and also through the m-value of the left-hand peak of the fit to the skewnesses, without any adjustments. This line can be seen to pass very closely to the m-value of the left-hand maximum of the fit to the asymmetries and also very close to the left-hand minimum of $\delta \nu$. The right-hand dashed line was drawn so that it would pass through the m-value of the right-hand peak of the inverted line-width polynomial fit and through the m-value of the right-hand peak of the polynomial fit to the skewnesses. In contrast to the situation for the left-hand line, this line does not pass as closely to the peak in $\delta \nu$ and it misses the right-hand peak of the fit to the asymmetries by an even larger amount. Other than these relatively minor shifts in the locations of a few of the extrema, the two sloping straight lines demonstrate quite well the systematic decrease in Δm that occurred when going from the upper to the bottom panel of Figure 15. This figure clearly demonstrates that the locations of the area bisectors have the dominant influence on the multiplet structure of the different parameters for the $(2, 600)$ multiplet.

The similarity of the five different least-squares linear regression fits that we listed in Sections 4.2.1 through 4.2.4 as functions of Δm_{bis} demonstrates that the pattern shown in Figure 15, for which Δm was the largest for the ridge widths and was smallest for the skewnesses, persists for all of the multiplets for which l is greater than 600. However, since the slopes of the five linear fits are not identical, the differences in the values of Δm for the line widths and for the skewnesses gradually increase with increasing l.

4.3. *Sample f- and p-mode parameters*

In Figures 16 and 17 we show the run of the natural logarithm of the amplitudes $A_{n,l,m}$ (upper-left), the run of the frequencies $\nu_{n,l,m}$ (upper-right), the run of the natural logarithm of the line widths $w_{n,l,m}$ (lower-left), and the run of the line asymmetries $B_{n,l,m}$ (lower-right) versus m/L for the $(5, 150)$ and the $(2, 900)$ multiplet, respectively. In each panel, the black diamonds represent the respective variable drawn, while the red line is for the corresponding smooth fit, the calculation of which is described in detail in Section 3.5. Black triangles mark outlying cases. While in both figures the run of the frequencies versus m/L looks smooth, there is for both multiplets a rather large scatter to be noted in the runs of amplitude, line width, and line asymmetry versus m/L. We note that there are no obvious trends to be seen in the runs of either the line widths or the line asymmetries versus m/L in the two bottom panels of Figure 16. These results are consistent with the fact that the fitted
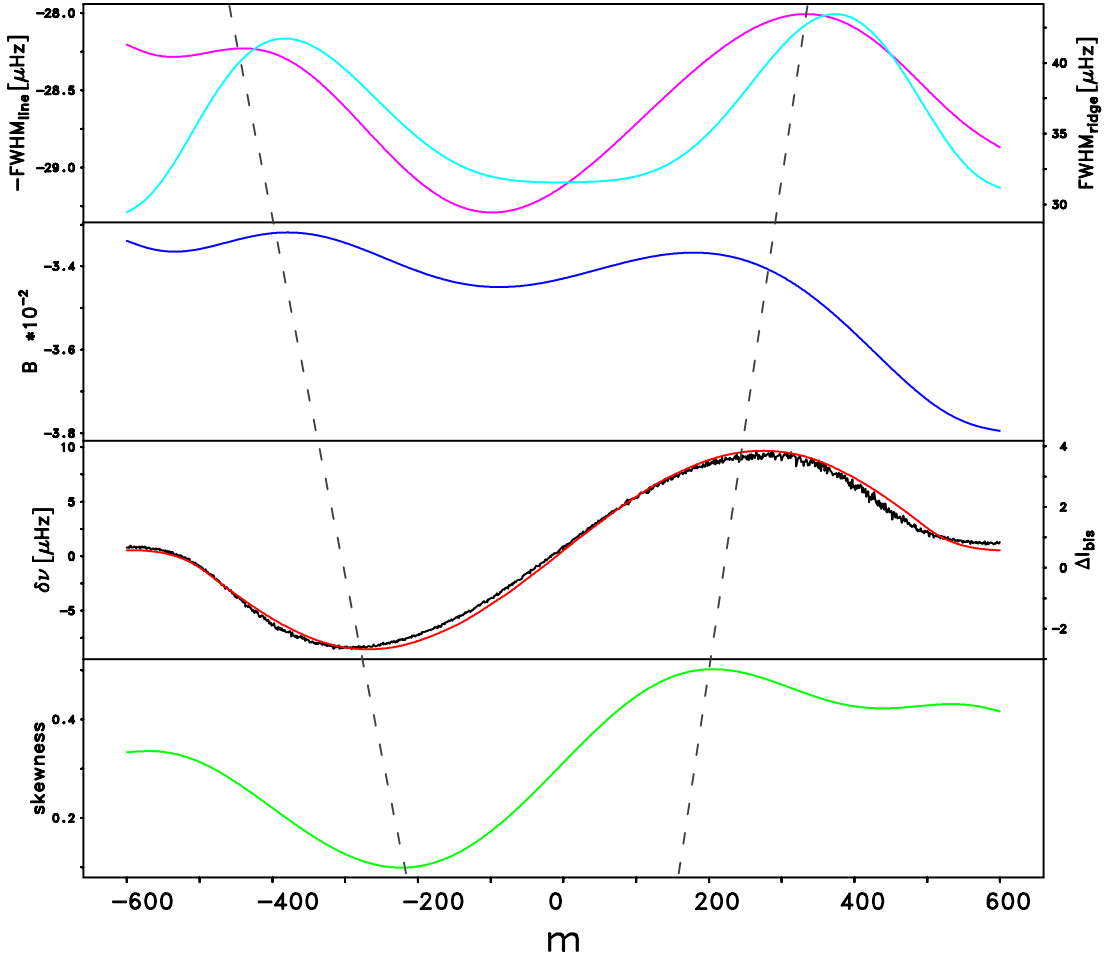
Figure 15. (Upper panel) Dependence of the polynomial fits to the ridge widths (turquoise curve) and to the line widths (magenta curve) on m for the $(2, 600)$ multiplet. The fit to the line widths has been inverted, as indicated by the left-hand label, since these two polynomials were shown to be anti-correlated in Figure 11. The label for the ridge fits is shown at the right. (Second panel) Dependence on m of the polynomial fit to the asymmetries is shown as the blue curve. (Third panel) Dependence of $\delta\nu$ (black points) and of Δl_{bis} (red curve) on m. The label for $\delta\nu$ is shown at the left, while the label for Δl_{bis} is shown at the right. (Bottom panel) Dependence of the polynomial fit to the skewnesses (green curve) on m. The left-hand dashed straight line was drawn to pass through the left-hand peak of the inverted line width curve and through the left-hand minimum of the fit to the skewnesses. The right-hand dashed line was drawn to pass through the right-hand peak of the magenta curve and through the right-hand peak of the fit to the skewnesses. The upper separation of these two dashed lines is equal to Δm_{line}, while the lower separation of them is equal to Δm_{skew} for this multiplet.

profile for the $(5, 150)$ multiplet looked more like the sample profiles shown earlier in Figure 2 than the fitted profiles shown in either Figures 3 or 4. Specifically, the fitted profile for this multiplet consisted of a single narrow peak at the location of the target mode and four well-separated peaks for the $l \pm 1$ and $l \pm 2$ sidelobes. In contrast, for the $(2, 900)$ multiplet, the variations in the runs of both the line widths and the line asymmetries with m/L that are visible in the two bottom panels of Figure 17 are consistent with the variation in those parameters that we previously showed in the right-hand panels of Figures 11 and 13 for the $(2, 600)$ and $(4, 500)$ multiplets, respectively. For both
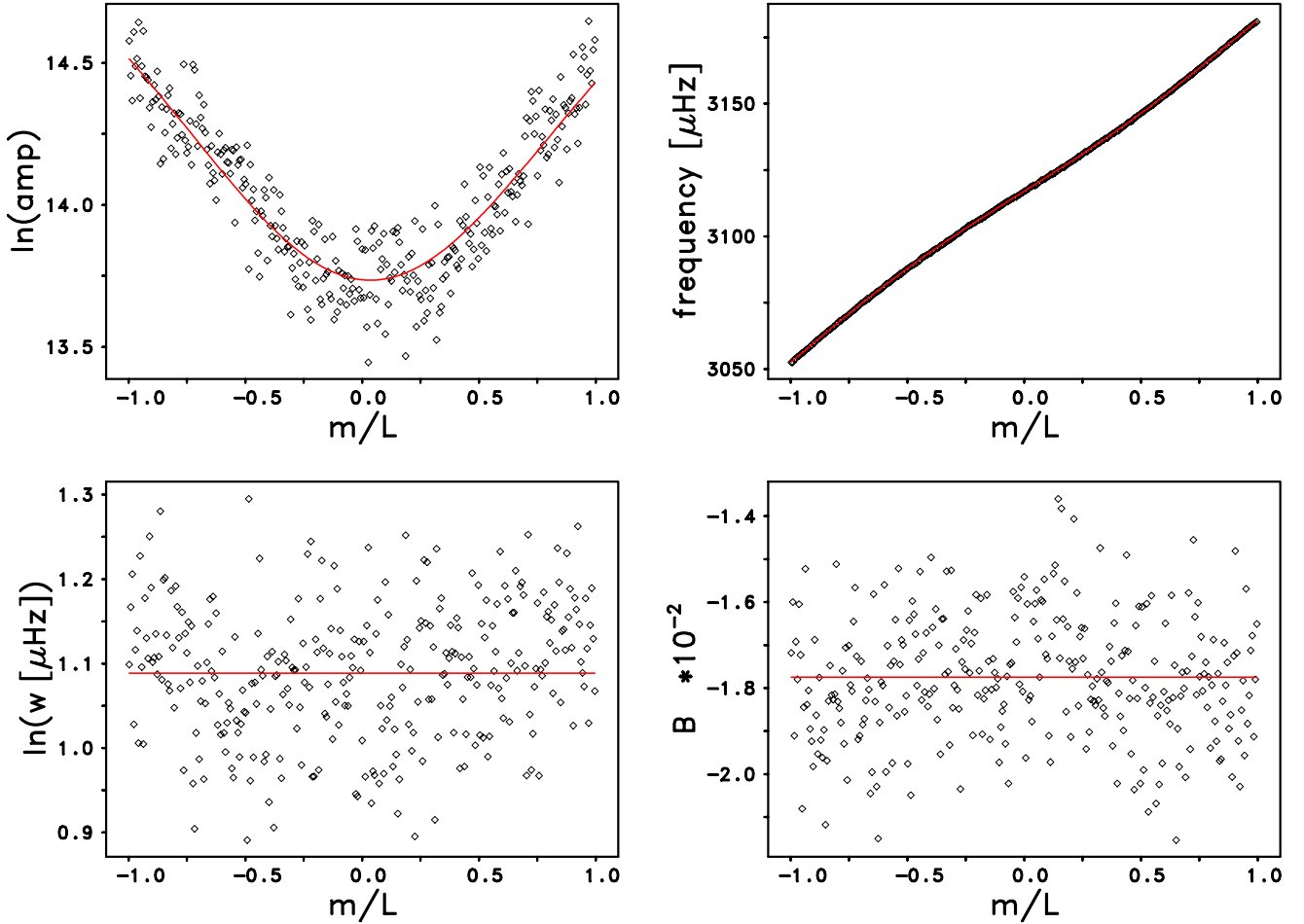
Figure 16. Runs of the natural logarithm of the amplitudes $A_{n,l,m}$ (upper-left), the frequencies $\nu_{n,l,m}$ (upper-right), the natural logarithm of the line widths $w_{n,l,m}$ (lower-left), and the line asymmetries $B_{n,l,m}$ (lower-right) versus m/L for the $(5, 150)$ multiplet. In each panel, the black diamonds represent the respective variable drawn, while the red line is for the corresponding smooth fit. For the upper-left panel the red curve is the ϖth order Chebyshev polynomial, Ξ_ϖ, that was described in Section 3.5, while for the upper-right panel the red curve is given by Equation (25). We note that both the line width and the line asymmetry are fitted as functions of m/L by a horizontal straight line (cf. Section 3.5). For this multiplet we determined the frequency to $\nu_{\mathrm{fit}} = 3117.100 \pm 0.009\,\mu\mathrm{Hz}$.

of those multiplets, their fitted profiles were single-peaked ridges of power as was the case for the $(2, 900)$ multiplet. We have already shown the runs of the differences between the fitted frequencies and the ridge frequencies and of the skewnesses for this $(2, 900)$ multiplet as functions of m/L in the right-hand panel of Figure 8, and so it is clear that the different appearances of the line widths and the asymmetries in the bottom panels of both Figures 16 and 17 were due entirely to the different shapes of their fitted profiles.

In Figure 18 we show in the upper-left panel the degree dependence of the set of frequencies obtained with the MPTS method when applied to the power spectra obtained from the $\mathcal{R}2010\_66$ observing run. In the upper-right panel the degree dependency of the line widths, w, is shown. The degree dependency of the amplitudes, or power densities, and the line asymmetries, B, is shown in the lower-left and lower-right panel, respectively. We note the noisy appearance of the $n = 0$ ridge for
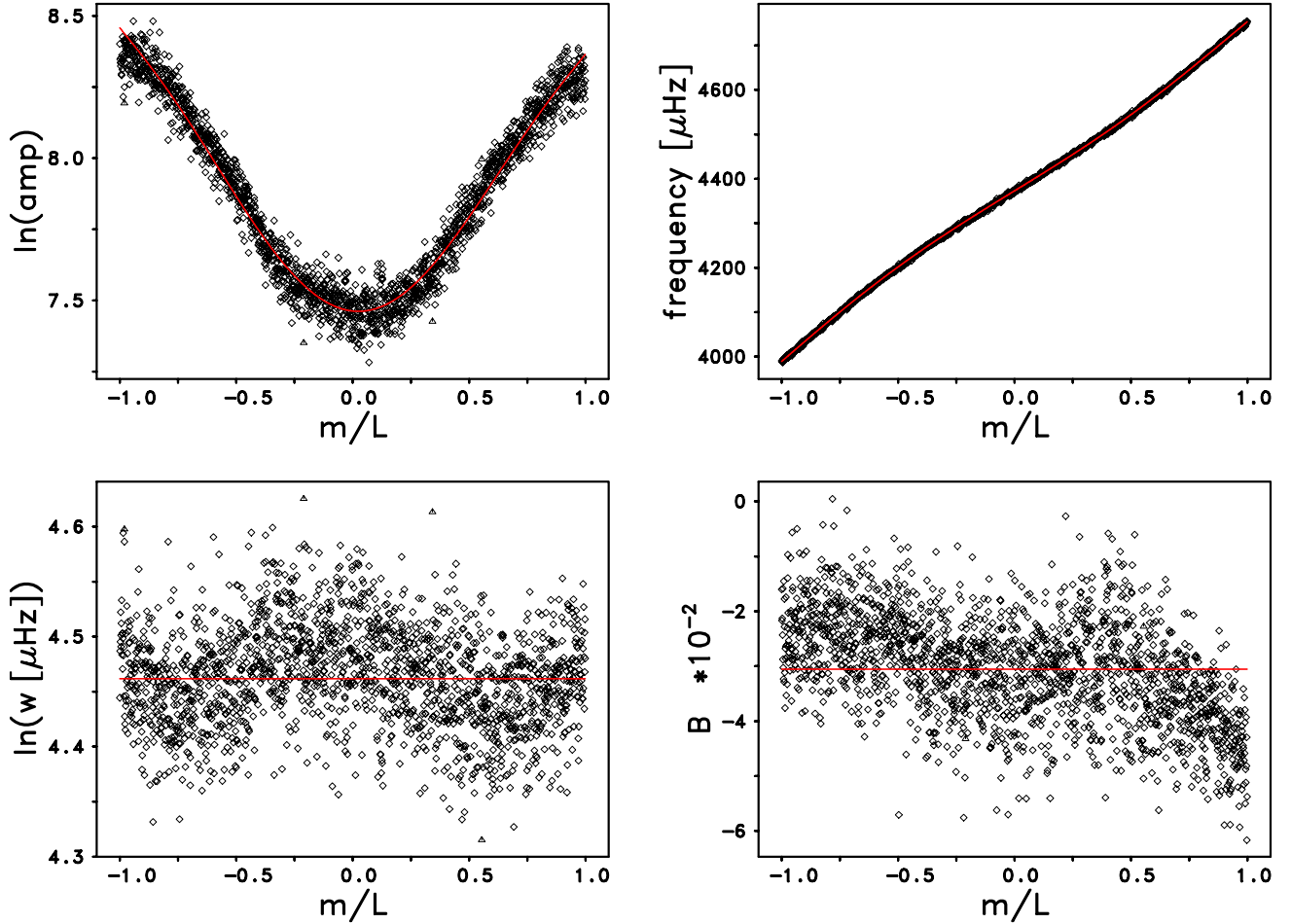
Figure 17. Same as Figure 16, but for the $(2, 900)$ multiplet. Black triangles mark outliers. In the bottom-left panel there is a variation that is similar in shape to the blue polynomial that is shown in the right-hand panel of Figure 11. In the bottom-right panel there is a variation that is similar in shape to the red polynomial that is shown in the right-hand panel of Figure 13. Nevertheless, as we have explained in Sections 3.5, 4.2.3, and 4.2.4 both the line width and the line asymmetry are fitted as functions of m/L by the two different straight red lines. For this multiplet we determined the frequency to $\nu_{\rm fit} = 4372.679 \pm 0.059\,\mu{\rm Hz}$.

higher degrees for both the line width and the line asymmetry. We also note that the positive values of the line asymmetry are all statistically insignificant. In the ranges $0 \le l \le 1000$, $0 \le n \le 30$, $965 \le \nu \le 4600\,\mu{\rm Hz}$ we were able to successfully fit a total of 6,677 multiplets, which corresponds to a total of 4,342,164 individual modes.

5. COMPARISON OF RESULTS FROM MPTS METHOD, WMLTP METHOD, AND ESTABLISHED FITTING METHODOLOGIES

Before we will present the results from our comparative study, we comment briefly on the various methods involved.

5.1. *WMLTP method*

In Paper I the rev6 version of the WMLTP method was described. However, shortly after the publication of Paper I, we made improvements to that version and replaced it with a new rev7
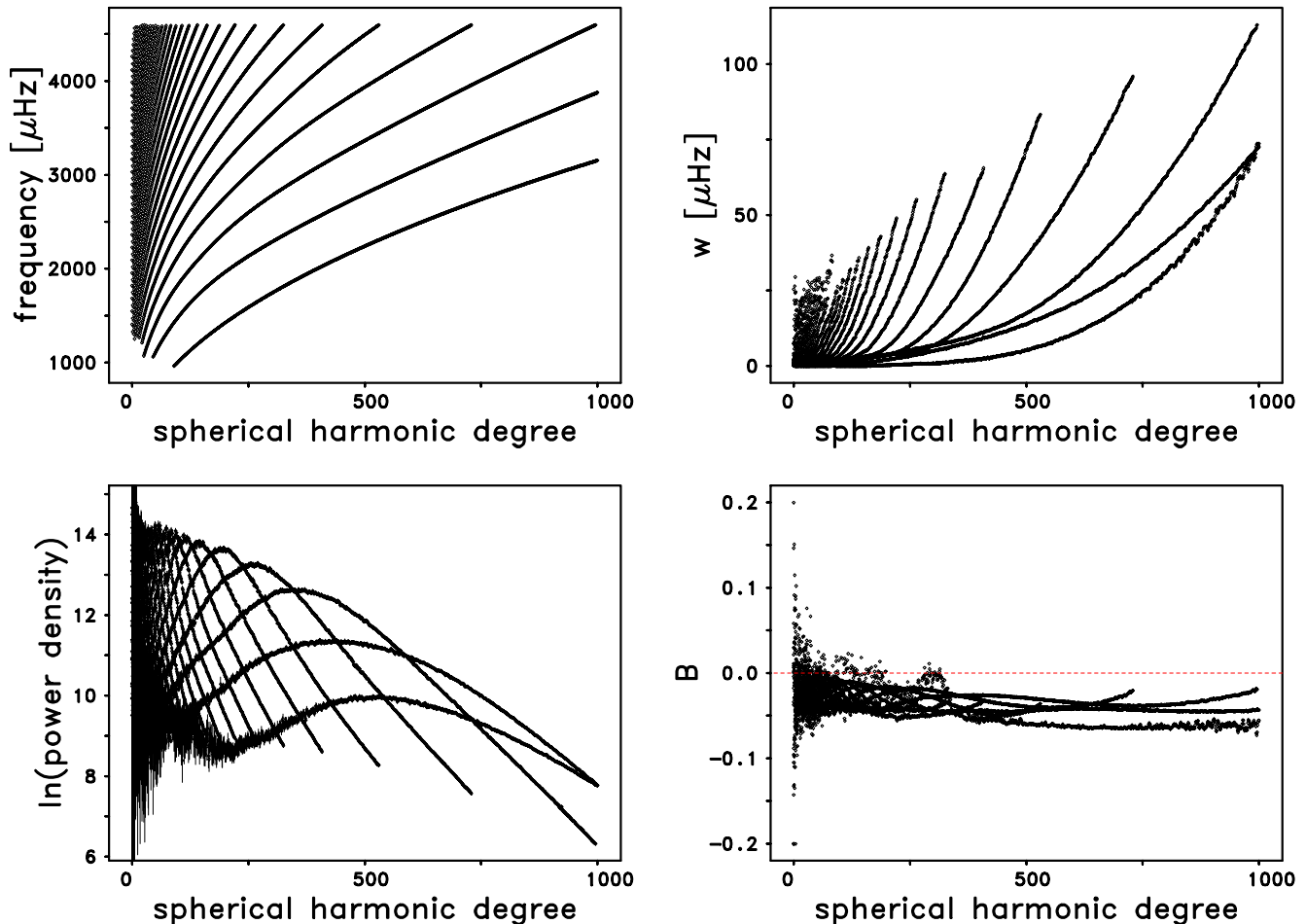
Figure 18. (Upper-left) Dispersion plane coverage of the set of frequencies obtained with the MPTS method when applied to the power spectra obtained from the $\mathcal{R}2010\_66$ observing run. (Upper-right) Degree dependency of the line widths, w. (Lower-left) Degree dependency of the amplitudes, or power densities. (Lower-right) Degree dependency of the line asymmetries, B. The dashed red line is a reference line for $B = 0$ to illustrate how few values of the line asymmetry were close to zero.

version. The details of these revisions have not yet been published but are presented in Appendix B. As was the case for the rev6 version, the rev7 version has two different options for handling the m-averaged power spectra that it employs. In the first option, a set of previously-generated m-averaged spectra is input, while in the second option a set of un-averaged zonal, tesseral, and sectoral power spectra are input along with a set of frequency-splitting coefficients. In the second option, this set of splitting coefficients is used by the program to generate a separate section of the m-averaged spectrum for a given degree l within the fitting box for each (n, l) multiplet.

One set of our rev7 WMLTP modal parameters was generated using the first option. In this case the very same set of 2010 MDI m-averaged power spectra that we used to obtain the rev6 WMLTP parameters in Paper I and in Appendix B was employed. As we pointed out in Paper I, this set of m-averaged spectra, which was the set $\mathcal{S}2010\_66a$ of Table 2 of that paper, was generated using a set of frequency-splitting coefficients that were computed using a cross-correlation technique on the set of un-averaged power spectra obtained during the 1996 MDI Dynamics Run. The second set of rev7 WMLTP results that we will be presenting was computed using the second option. In contrast to our

first set of WMLTP results, this set was obtained from the same set of frequency-splitting coefficients that were generated from the 2010 MDI Dynamics Run by our MPTS method. So, while the same set of un-averaged MDI power spectra was employed in the generation of both rev7 WMLTP tables, two different sets of non-n-averaged frequency-splitting coefficients computed from two different epochs were employed.

In order to avoid any confusion, we note that the term "WMLTP" will refer to the rev7 version of this method. We will use the term "WMLTP_ac" when we refer to the rev7 version that uses the option of calculating the m-averaged spectra internally in the code.

5.2. *Mean-multiplet technique*

In the mean-multiplet technique of Schou (1992) the Fourier transforms of the gap-filled time series of the spherical harmonic coefficients, which result from the spatial decomposition of the individual Dopplergrams in an observing run, are fit using a maximum likelihood approach, taking into account leakage between the modes (Larson & Schou 2015). Rather than fitting, however, for the individual $2l+1$ mode frequencies within a multiplet (n, l), this technique includes a fitting algorithm that yields the mean-multiplet frequency $\nu_{n,l}$ and the set of frequency-splitting coefficients $a_k^{(n,l)}$ for each multiplet directly, assuming that the line width and the amplitude of the $2l + 1$ modes are independent of the azimuthal order m. Initially, the algorithm fits for a total of 6 frequency-splitting coefficients, then for 18 and 36 once the 6-term fits have converged. Leaks from multiplets other than (n, l) are taken into account. The asymmetry of the line profiles is taken into account by using an asymmetrical profile that is derived by a generalization of the profile of Nigam & Kosovichev (1998). This way undesirable properties of the profile of Nigam & Kosovichev (1998) are avoided, viz. its invalidity far from the mode frequency and the non-boundedness of its integral over all frequencies (Larson & Schou 2015). The data obtained from the mean-multiplet technique, which we used in our comparisons and which correspond to our data set $\mathcal{R}2010\_66$, can be downloaded from `jsoc.stanford.edu` using the data-set specification `mdi.fd_V_sht_modes_asym[6335d]`. For the details of their generation we refer to Larson & Schou (2015). In the following we will use the term "JS" when we are referring to the mean-multiplet technique.

5.3. *Fitting methodology of Korzennik*

The fitting methodology of Korzennik et al. (2004) is applicable to high-degree modes with degrees $l \gtrsim 100$ (p-modes) to $l \gtrsim 200$ (f-modes). Its basic idea consists of correcting for the bias introduced when fitting a ridge of power at high degrees. For this purpose, a detailed model of the underlying modes that contribute to the distribution of power in a ridge was developed to generate synthetic ridges, which are then fitted using the same methodology employed to fit the observations. Hence, the results of fitting these synthetic data allow the user to derive a measure of the bias between the ridge properties and those of the underlying targeted mode used in the modeling. By means of this measure the results from fitting an observed ridge can be corrected to derive the unbiased properties of the underlying targeted mode. The data obtained from the fitting methodology of Korzennik, which we used in our comparisons and which correspond to our data set $\mathcal{R}2010\_66$, are located in `www.cfa.harvard.edu/~sylvain/research/tables/HiL/MDI/2010/`. For the details of their generation we refer to Korzennik et al. (2013). In the following we will use the term "SK" when we are referring to the fitting methodology of Korzennik.

5.4. *Results from comparative study*

Before we will present the results from our comparative study, we list in Table 5 the degree ranges, the radial order ranges, the frequency ranges, and the number of fitted frequencies, line widths, and a_1 frequency-splitting coefficients for all five methods involved in our study. Since not all of the modes in each table are present in all of them, the actual numbers of frequency differences, line-width differences and a_1 differences will not necessarily be equal to the smaller of the pairs of numbers in Table 5.

5.4.1. *Raw comparisons*

In Figure 19 we show a comparison of the MPTS, WMLTP, JS, and SK methods in terms of the frequencies, the natural logarithm of the line widths, and the a_1-splitting coefficients for both the $n = 0$ and $n = 8$ ridge. The upper-left panel of Figure 19 shows that in the degree range $90 \le l \le 300$ the frequencies from the MPTS method and the frequencies produced by both the WMLTP and JS methods agree within plotting accuracy, aside from some scatter in the MPTS frequencies at the low-frequency end of the $n = 0$ ridge. However, for $185 \le l \le 600$ the frequencies from the SK method are systematically offset above the other sets of frequencies and also show considerably more scatter. For $l > 300$ the WMLTP frequencies can be seen to fall between the MPTS frequencies and the SK frequencies. The upper-right panel of Figure 19 shows that for the $n = 8$ ridge the agreement in frequencies from the MPTS, WMLTP, and JS methods for $9 \le l \le 112$ was so good that only the green symbols of the JS frequencies are visible. For $113 \le l \le 221$ the MPTS frequencies are seen to fall slightly above both the WMLTP and the SK frequencies.

Table 5. Comparison of the *l*-*n* coverages, the frequency ranges, and numbers of fits in the tables of the frequencies, line widths, and a_1 frequency-splitting coefficients computed by the MPTS, WMLTP, and WMLPT_ac methods, as well as the JS method, and the SK method.

method	n-range	l-range	ν-range	n_{ff}	n_{fw}	n_{fa}
MPTS	0 - 30	0 - 1000	964.95 - 4599.82	6677	6677	6655
WMLTP	0 - 29	0 - 1000	964.96 - 4599.89	6685	6685	$\cdots$
WMLTP_ac	0 - 29	0 - 1000	964.93 - 4598.68	6663	6663	$\cdots$
JS	0 - 28	0 - 300	964.76 - 4475.54	1946	1946	1945
SK	0 - 14	100 - 1000	1378.12 - 4599.96	4724	3306	4725

NOTE— The frequency range, ν-range, is measured in μHz, n_{ff} denotes the number of fitted frequencies, n_{fw} the number of fitted line widths, and n_{fa} the number of fitted a_1 frequency-splitting coefficients in the corresponding frequency range. Instead of applying the usual upper frequency limit of $7000\,\mu$Hz for both the WMLTP and the WMLTP_ac methods, this limit has been artificially set to $4600\,\mu$Hz, because above this limit no MPTS mode parameters are available for comparison, for the reason given in Section 4. The fitting table provided by the SK method actually contains frequencies up to $5636\,\mu$Hz. The upper boundary of the frequency range listed for the SK method is the highest frequency in the fitting table just below $4600\,\mu$Hz.
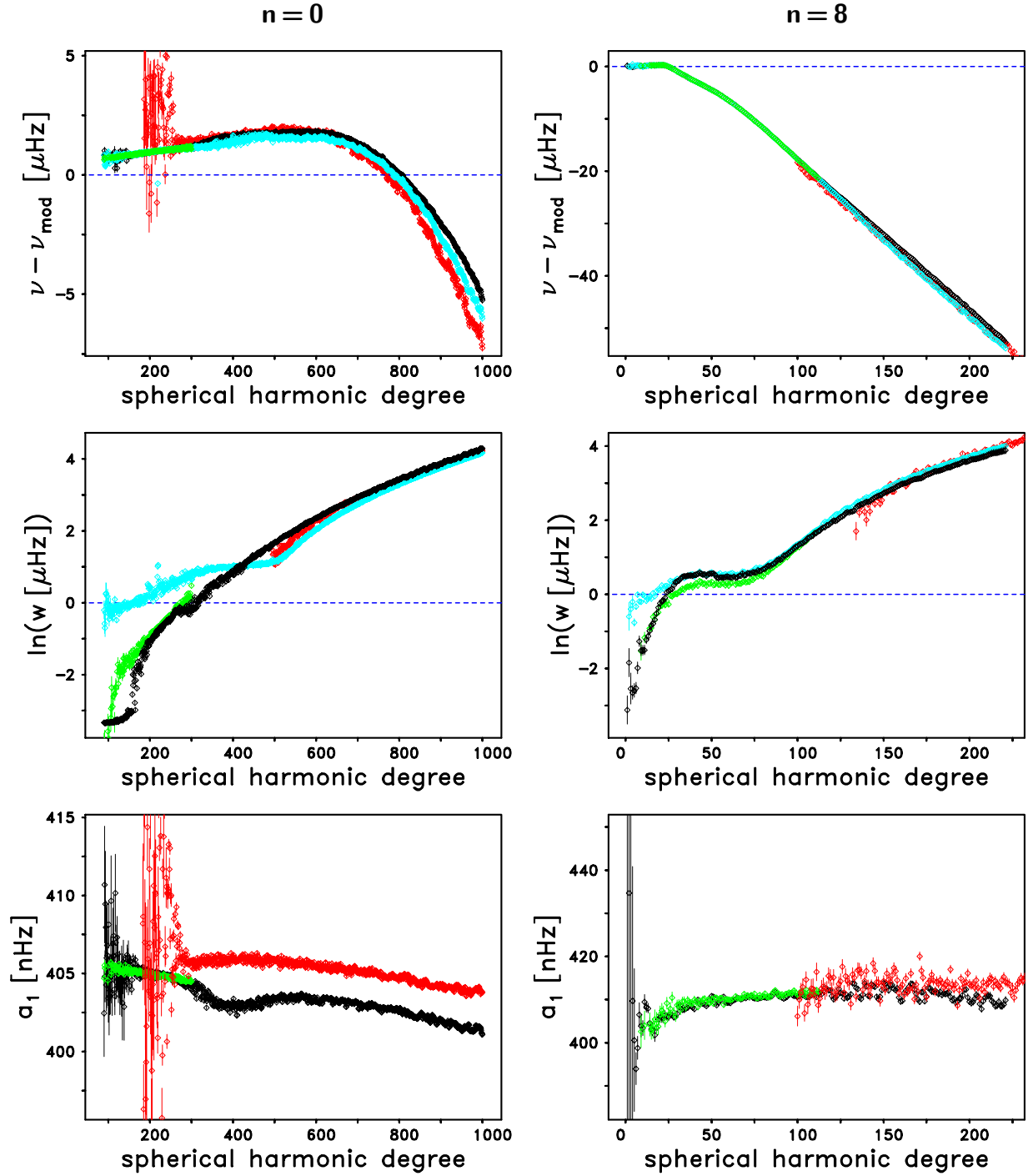
Figure 19. Comparison of the MPTS, WMLTP, JS, and SK methods in terms of the frequencies (upper panels), the natural logarithm of the line widths (middle panels), and the a_1-splitting coefficients (lower panels) for the $n = 0$ (left column) and $n = 8$ (right column) ridge. The color style is as follows: black is for the MPTS, turquoise is for the WMLTP, green is for the JS, and red is for the SK method. The error bars are for 1σ uncertainties. To get a better resolution, we have subtracted from the fitted frequencies ν the theoretical frequencies ν_{mod} computed from Model S of Christensen-Dalsgaard et al. (1996). The dashed blue lines are for an ordinate of zero. We note the different scales of the ordinates in the panels shown in the same row.

The middle-left panel of Figure 19 shows that for the $n = 0$ ridge, one major advantage of the MPTS, WMLTP, and JS methods is that they all produce line widths for $l < 496$ which is the lowest degree where the SK method produces line widths for this ridge. For lower degrees both the MPTS and JS methods produce line widths that are systematically smaller than the widths produced by the WMLTP method. The unphysical looking run of the MPTS line widths for $l < 180$ is an effect of the lower boundary that is applied to the line width. For $100 \leq l \leq 200$ the MPTS method produces line widths that are systematically smaller than does the JS method. Above $l = 700$ the MPTS, WMLTP, and SK methods all produce line widths that are very similar. The middle-right panel shows that for the $n = 8$ ridge the WMLTP method produces larger line widths than either the MPTS or JS methods for $l \leq 25$. For $26 \leq l \leq 90$ the JS method produces slightly smaller widths than either the MPTS or WMLTP methods. For $l \geq 134$ the MPTS, WMLTP, and SK methods all produce very similar line widths.

The first point to note about the two bottom panels of Figure 19 is that they do not include any WMLTP results since that method is only applicable to m-averaged spectra and does not produce any frequency-splitting coefficients. The second point to note is that for the degree ranges where both the MPTS and JS methods produced splitting coefficients (which were $90 \leq l \leq 300$ for the $n = 0$ ridge and $9 \leq l \leq 112$ for the $n = 8$ ridge), both sets of the a_1-splitting coefficient agreed quite well. On the other hand, for $183 \leq l \leq 300$ the SK method produced a_1-splitting coefficients that showed considerably more scatter than did either the MPTS or JS a_1-splitting coefficients, and for higher degrees the SK a_1-splitting coefficients were systematically higher than the MPTS coefficients. The SK a_1-splitting coefficients also did not include the narrow bump around $l \approx 400$ that the MPTS coefficients showed. The bottom-right panel of Figure 19 shows that the MPTS method produced for the $n = 8$ ridge a_1-splitting coefficients down to $l = 1$, and that both the MPTS and JS methods produced nearly identical a_1-splitting coefficients for this ridge for $9 \leq l \leq 112$. This panel also shows that the SK a_1 coefficients for this ridge showed more scatter and were offset above the a_1 coefficients from the MPTS method.

Before we discuss the comparisons listed in Table 6, we want to stress that, because of the different ranges of frequencies and degrees in which the various codes were operating, the comparisons shown in Table 6 are actually related to quite different areas of the l-ν plane. With this caveat in mind, the average frequency differences in Table 6 clearly show that the JS method agreed most closely with the MPTS frequencies, while the WMLTP and WMLTP_ac frequencies were effectively tied for the second-closest agreement with the MPTS frequencies, and the SK frequencies showed the largest disagreement with the MPTS frequencies. The excellent overall agreement between the WMLTP and WMLTP_ac frequencies that is shown in the last line of the second column of Table 6 is quite remarkable since, as we have already pointed out, the WMLTP frequencies were produced using frequency-splitting coefficients obtained from MDI observations acquired during the 1996 solar minimum, while the WMLTP_ac frequencies were generated using splitting coefficients obtained from MDI observations made during the rising phase of Cycle 24 in mid-2010. Even though the splitting coefficients used in the two cases were different, they obviously had an insignificant effect on the two sets of frequencies. This overall agreement also confirms the usefulness of the option that the WMLTP_ac method provides of computing the m-averaged spectra within the WMLTP code itself. On the other hand, because the same set of 2010 MDI frequency-splitting coefficients that was generated by the MPTS method was also used within the WMLTP_ac method, the MPTS-WMLTP_ac

frequency differences shown in the second line of Table 6 were solely caused by the two different fitting methods themselves.

In the case of the line widths, both the JS method and the SK method produced widths that were on average smaller than the widths that were produced by the MPTS method. Once again, the results from the JS method again agreed most closely with the MPTS results, while this time the SK results ranked second. On the other hand, both the WMLTP and WMLTP_ac methods produced line widths that were larger than the MPTS widths, with the WMLTP widths ranking third, and the WMLTP_ac results ranking fourth in terms of the absolute values of the average line-width differences. In contrast with the excellent agreement between the WMLTP and WMLTP_ac frequencies, the line-width differences between the WMLTP and WMLTP_ac methods that are shown in the last line of the fifth column of Table 6 indicate that the use of splitting coefficients from 1996 did result in significantly larger line widths in comparison with those computed using the 2010 splitting coefficients. For the a_1-splitting coefficients, the JS coefficients agreed more closely with the MPTS results than did the SK results.

5.4.2. *Normalized comparisons*

In the upper four panels of Figure 20 we compare the MPTS method with the WMLTP, the WMLPT_ac, the JS, and the SK methods in terms of the dependence of the normalized frequency differences on the inner turning-point radius of the corresponding modes. The normalizations were carried out by dividing the raw differences by the formal error of each difference. The first point to note is that there was excellent agreement between the frequencies that were produced by the MPTS and JS methods, as is shown in the middle-left panel. These two frequency tables agreed so closely that 97.6 percent of the differences were statistically insignificant, as shown in the second column of Table 7. Considerably worse than these frequency differences were the differences between the MPTS and SK methods, as shown in the middle-right panel, for which only 33.4 percent of those

Table 6. Comparison of the MPTS method with the WMLTP, WMLTP_ac, JS, and SK methods in terms of frequency differences, line-width differences, and a_1-splitting coefficient differences.

difference	frequency [μHz]			line width [μHz]			a_1 [nHz]		
	avg	std	n_c	avg	std	n_c	avg	std	n_c
MPTS - WMLTP	0.3921	0.0434	6663	-0.2915	0.2542	6663	$\cdots$	$\cdots$	$\cdots$
MPTS - WMLTP_ac	0.3938	0.0429	6663	-0.4176	0.2438	6663	$\cdots$	$\cdots$	$\cdots$
MPTS - JS	0.0092	0.0088	1945	0.0774	0.0433	1945	-0.2084	1.7726	1944
MPTS - SK	0.8483	0.0682	4719	0.2502	0.4496	3301	-1.8651	0.2845	4721
WMLTP_ac - WMLTP	0.0020	0.0038	6663	0.2420	0.0291	6663	$\cdots$	$\cdots$	$\cdots$

NOTE— The first column indicates which method is compared with which, and in which sense the differences are taken. For each comparison are listed the averages (avg), the standard deviations (std), and the number of common cases (n_c) of the frequency differences (measured in μHz), the line width differences (measured in μHz) and, if applicable, the a_1-splitting coefficient differences (measured in nHz). We note that the averages and the standard deviations are calculated in a weighted fashion according to Equations (30) through (32), using as weights the inverse of the formal error of the differences.
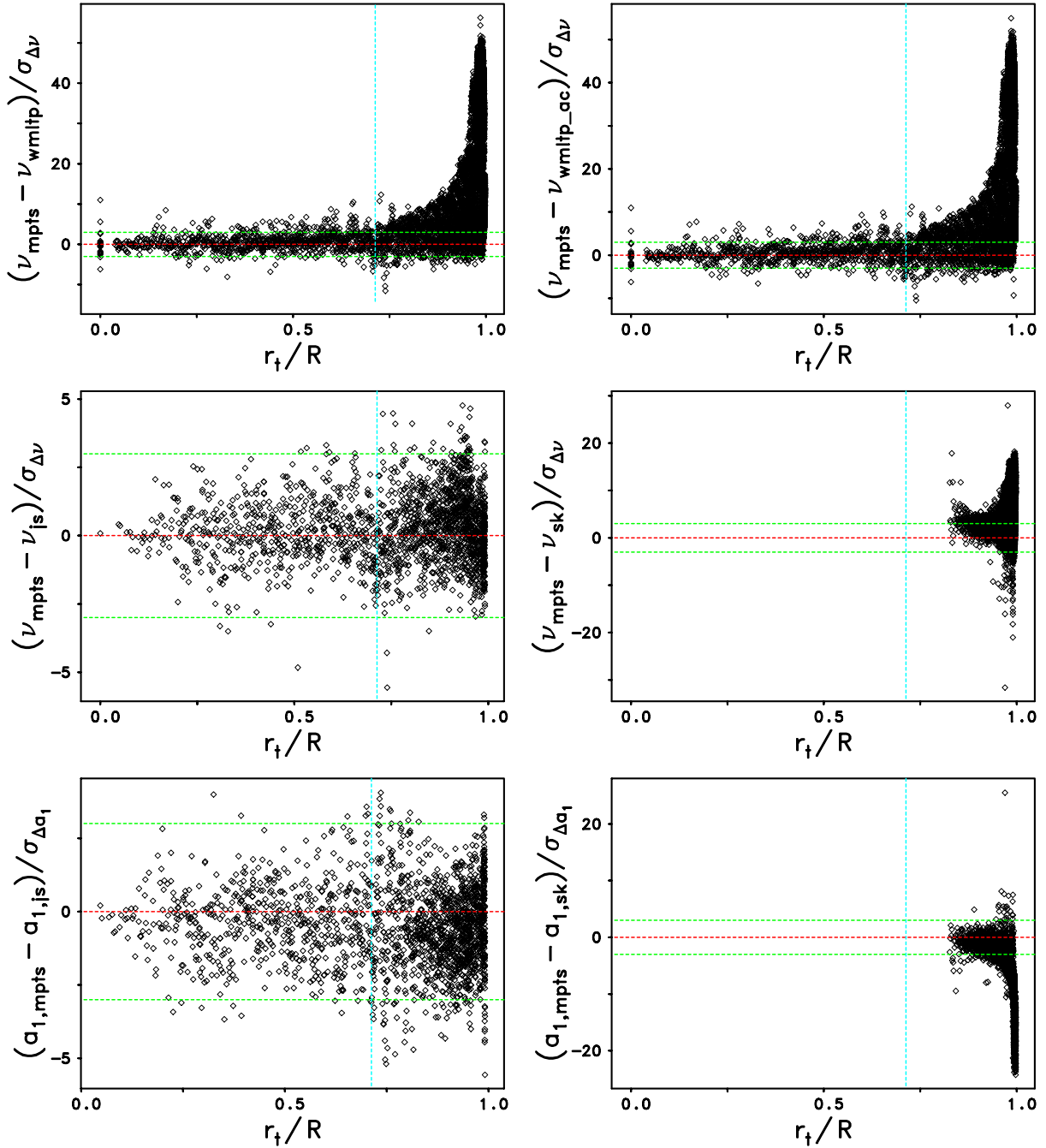
Figure 20. Dependence of normalized frequency differences (upper and middle panels) and normalized a_1-splitting coefficient differences (lower panels) on the fractional inner turning-point radius, r_t/R, of the corresponding f- and p-modes. Here, R is the radius of the Sun. The normalization was carried out by dividing the raw differences by the formal error of each difference. The subscripts mpts, wmltp, js, and sk in the axis labeling refer to the methods from which the measurements were obtained. The subscript wmltp_ac refers to the variant of the WMLTP method in which the segments of the raw spectra are collapsed into the m-averaged spectrum within the WMLTP code rather than collapsing them outside the code, using the frequency-splitting coefficients obtained from the MPTS method. The dashed red line in the panels is for a difference of zero, the dashed turquoise line in the panels marks the lower boundary of the convection zone, and the dashed green lines show the $\pm 3\sigma$ values. We note the different scales of the ordinates in the panels shown in the same row.

differences were statistically insignificant. In third place were the differences between the MPTS and WMLTP methods that are shown in the upper-left panel, for which 27.7 percent of the differences were statistically insignificant. In fourth place was the comparison of the frequencies in the MPTS and WMLTP_ac methods, as is shown in the upper-right panel. Here, 27.1 percent of the differences were statistically insignificant. The second point to note is that for all four of the other methods the vast majority of the significant frequency differences were positive rather than negative, as is shown in the third and fourth columns of Table 7.

Table 7. Comparison of the MPTS method with the WMLTP, WMLTP_ac, JS, and SK methods in terms of normalized frequency differences.

normalized difference	a	b	c	d	e
MPTS - WMLTP	27.69	97.94	2.06	96.97	14.809
MPTS - WMLTP_ac	27.06	97.86	2.14	96.75	14.973
MPTS - JS	97.58	85.12	14.88	80.85	0.301
MPTS - SK	33.44	95.87	4.13	100.00	5.989

NOTE— meaning of columns:
  a: percentage of insignificant differences (3σ level)
  b: percentage of significant differences that were positive
  c: percentage of significant differences that were negative
  d: percentage of significant differences that were located in the convection zone
  e: average normalized frequency differences

Turning to the radial dependence of the various sets of frequency differences, the fifth column of Table 7 shows that for all four methods the vast majority of the significant frequency differences corresponded to modes that had inner turning-points that were located within the convection zone. However, for both the WMLTP and WMLTP_ac methods there were small numbers of significant frequency differences that corresponded to modes having $l = 0$ (i.e., $r_t = 0$) as is shown in the two upper panels of Figure 20. These modes are important because they decisively determine the trend of the profile of a structural inversion in the solar core. In the sixth column of Table 7 the average values of the normalized frequency differences are listed.

Apart from the normalized differences themselves, the most obvious difference in the comparisons of the MPTS, WMLTP, WMLTP_ac, and JS results with those from the SK method is the fact that the first four of those methods produce fits that extend much more deeply into the solar interior than does the SK method.

In the two bottom panels of Figure 20 we compare the MPTS method with the JS and SK methods in terms of the normalized a_1-splitting coefficient differences. Once again, there are no WMLTP or WMLTP_ac frequency-splitting coefficients since the WMLTP method does not produce any. The agreement in the a_1-splitting coefficients between the MPTS and the JS method is excellent, as is shown in the left bottom-row panel. Only 4.5 percent of the differences were statistically significant, and there was no obvious radial trend in the few cases which were significantly different. On the

other hand, in the case of the normalized a_1-splitting coefficient differences between the MPTS and the SK method, as shown in the right bottom-row panel, three-fourths of them were statistically significant and, moreover, they showed a pronounced trend with increasing r_t/R in the layers with $r_t/R \gtrsim 0.95$ for which the SK splitting coefficients were as much as $24.2\,\sigma$ larger than the MPTS coefficients.

5.4.3. *Scatter comparisons*

The smoothness of the fitted mode parameters with respect to degree l along a given ridge is a crucial property of any fitting methodology. In Paper I we suggested to measure the smoothness of a modal parameter υ with respect to degree l along a ridge of radial order n by the point-to-point scatter $\Sigma(\upsilon)$, as defined in Equation (B1) of Paper I. To compare the scatters associated with the MPTS, WMLTP, JS, and SK fitting methods, we used the following approach. First, for a given mode parameter υ, we determine the ratio of the scatters obtained from the two fitting methods to be compared, using the overlapping degree range of a given ridge for which υ has been fitted by both methods. Here, υ can be frequency, line width, or the a_1-splitting coefficient, for example. We note that it is important to fill any gaps in an overlapping degree range, because the scatter Σ is rather sensitive to missing data. At this stage, we were able to compare the scatters of the two methods on a ridge-by-ridge basis. In addition, we also carried out an overall comparison of the scatter by calculating the ratios of scatters for all the ridges that had been fit by the two methods and by then calculating a weighted mean of the scatter ratios, using as weights the width of the degree range that was fit by both methods along each ridge.

Our results obtained with this approach for the frequency scatter are illustrated on a ridge-by-ridge basis for all five methods in the four panels of Figure 21, where the scatter values of the MPTS frequencies are shown as the points on the black curves. We note that the scatter of any quantity is very sensitive to the degree range over which it is computed; and, since as we indicated in Table 5, not all of the methods obtained the same set of fits for each ridge, the scatter values could in principle vary from panel to panel. However, since both the WMLTP and WMLTP_ac methods covered identical degree ranges for all 30 of the fitted ridges, the black curves in the two upper panels are identical. On the other hand, since both the JS and SK methods generally covered degree ranges for each fitted ridge that differed from those of the MPTS method, the black curves in the two bottom panels turned out to be different from the black curves in the two upper panels. The red curve in the upper-left panel shows the frequency scatter values for the WMLTP method, while the red curve in the upper-right panel shows those for the WMLTP_ac method. At the scale of the figure, both of these two red curves appear to be nearly identical, and with the exception of only four points in each of these two panels, the MPTS scatter values were smaller than those from either the WMLTP or WMLTP_ac methods. On the other hand, as is shown in the lower-left panel, the frequency scatter values computed for the JS method were substantially larger than their counterparts from the MPTS method for all but the two lowest and the two highest ridges shown. In the lower-right panel the frequency scatter values computed from the SK method are shown as the red curve, and here every single value is larger than the corresponding value from the MPTS method. Taken together, these four panels show that the MPTS method produced the smoothest frequencies of any of these five methods.

Our results obtained with the same approach for the line-width scatter are illustrated on a ridge-by-ridge basis for all five methods in the four panels of Figure 22, where the scatter values of the MPTS
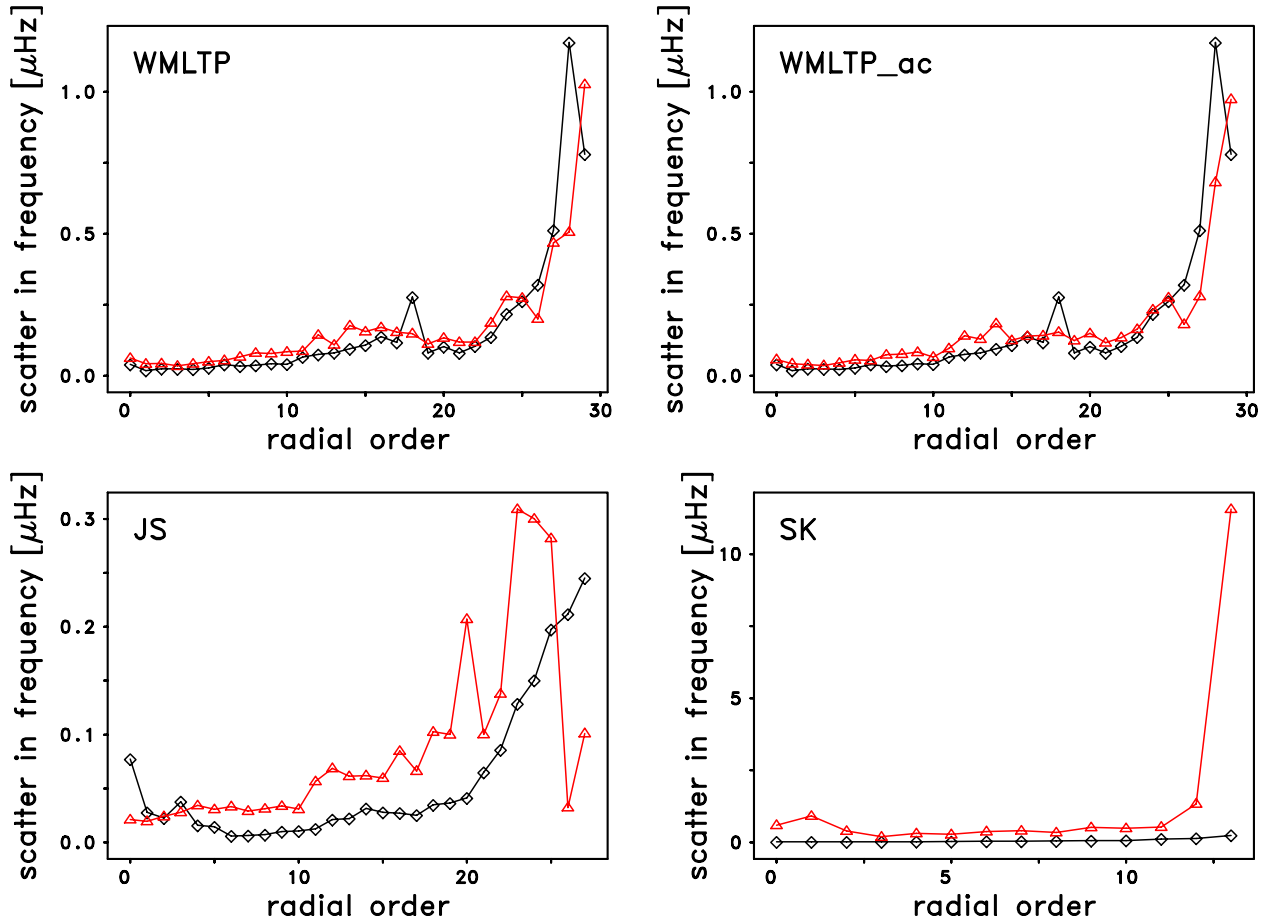
Figure 21. In each panel the black curve represents the frequency scatter for the MPTS method. The red curves represent the frequency scatter for the WMLTP method, the WMLTP_ac method, the JS method, and the SK method. We note that the black curves vary from panel to panel because the scatter is rather sensitive to the degree range over which it is computed. We also note the different x- and y-axis scales in the panels.

line widths are shown as the points on the black curves. The line-width scatter values computed from the WMLTP method are shown as the red curve in the upper-left panel, and the corresponding scatter values computed from the WMLTP_ac method are shown as the red curve in the upper-right panel. As was the case for the frequency scatter in Figure 21, the two black curves in the upper panels of Figure 22 are identical. In contrast with the upper panels in Figure 21, the MPTS line-width scatter values can be seen in these two panels to be substantially larger at high n than the line-width scatter for either the WMLTP or WMLTP_ac methods. The line-width scatter values from the JS method are shown as the red curve in the lower-left panel, while the line-width scatter values from the SK method are shown as the points on the red curve in the lower-right panel. For the $n = 0$ through $n = 17$ ridges, the MPTS line-width scatters were smaller than the corresponding JS scatter values, but for the higher-n ridges, the situation was reversed and the JS method produced smoother sets of line widths than did the MPTS method. For all but the $n = 0$ ridge, the SK method produced larger scatter values for the line widths than did the MPTS method.

While Figures 21 and 22 show the ridge-by-ridge scatter values for the frequencies and the line widths, respectively, for all five methods, columns 2 and 4 of Table 8 show our overall comparisons of
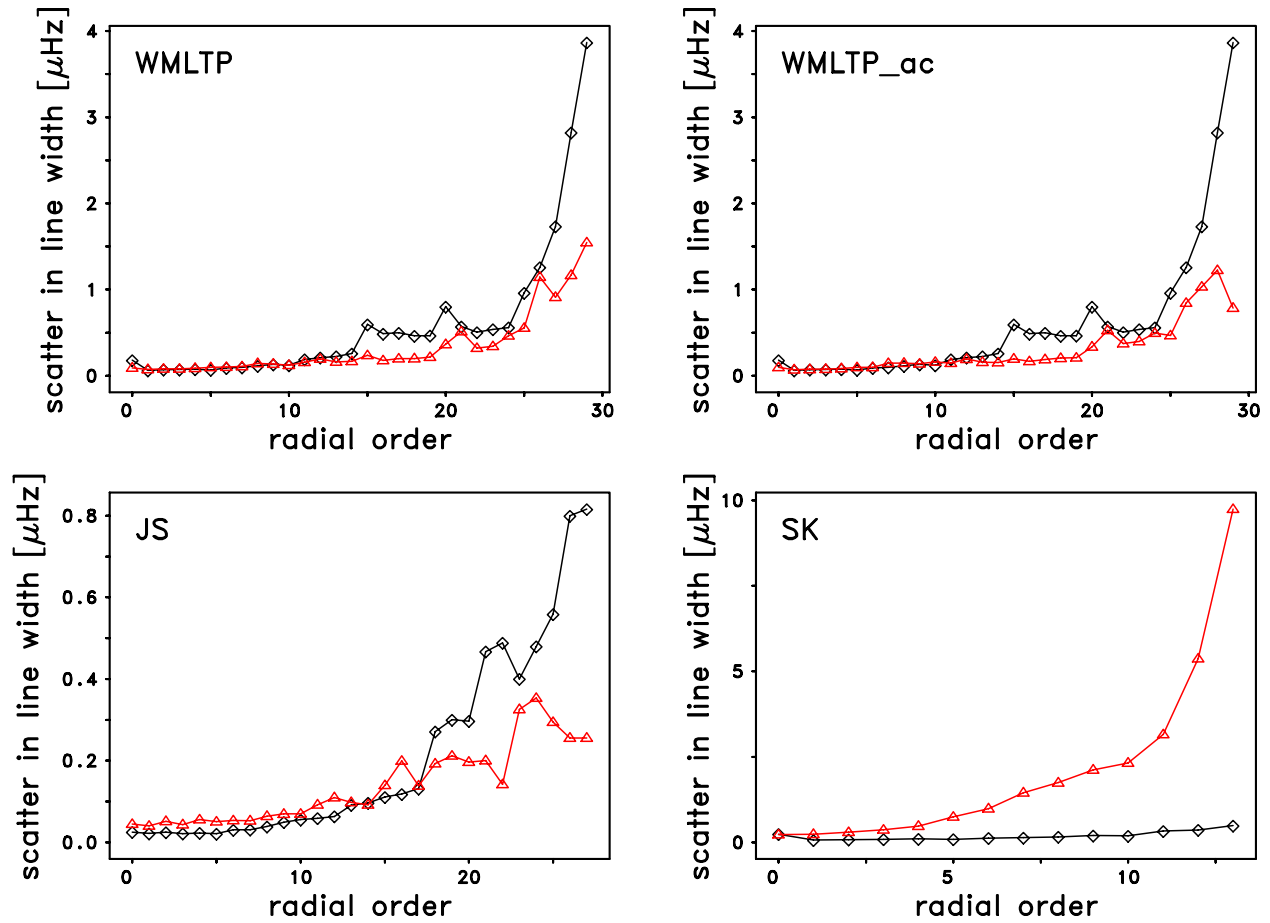
Figure 22. Same as Figure 21, but for the line width.

the frequency and line-width scatter values for the other four methods relative to the scatter values of the MPTS method. Specifically, columns 2 and 3 contain the average frequency scatter ratios and their standard deviations for each of these four methods relative to the MPTS method, while columns 4 and 5 contain the average line-width scatter ratios and their standard deviations for these other methods. The last line of columns 2 through 5 also shows the results of directly comparing the frequency and line-width scatter values of the WMLTP and WMLTP_ac methods. Columns 6 and 7 of this table show the average scatter ratios of the a_1-splitting coefficients and their standard deviations for both the JS and SK methods relative to the MPTS method. There are no entries in the sixth and seventh column of Table 8 for the WMLTP and WMLTP_ac methods since neither of those methods produces any splitting coefficients.

Inspection of the both columns 2 and 4 of Table 8 shows that, in terms of both the average frequency and line-width scatter ratios, the WMLTP and WMLTP_ac methods agreed most closely with the MPTS method, while the JS method ranked third, and the SK method ranked fourth. Inspection of the last row of both columns 2 and 4 confirms that the WMLTP and WMLTP_ac methods were indistinguishable in terms of the average scatter ratios of both the frequencies and the line widths. Inspection of column 6 of Table 8 shows that the JS method had slightly less scatter in the a_1-splitting coefficients than did the MPTS method and it also shows that the a_1-splitting coefficients computed

Table 8.   Comparison of the MPTS method with the WMLTP, WMLTP_ac, JS, and SK methods in terms of ratios of frequency scatters, ratios of line-width scatters, and ratios of a_1-splitting coefficient scatters.

scatter ratio	frequency		line width		a_1	
	avg	std	avg	std	avg	std
WMLTP / MPTS	1.735	0.542	0.988	0.372	$\cdots$	$\cdots$
WMLTP_ac / MPTS	1.736	0.582	0.989	0.422	$\cdots$	$\cdots$
JS / MPTS	2.470	1.355	1.660	0.598	0.655	0.420
SK / MPTS	26.617	29.158	4.756	8.606	23.708	35.450
WMLTP_ac / WMLTP	1.000	0.171	1.004	0.182	$\cdots$	$\cdots$

NOTE— The first column indicates which method is compared with which, and in which sense the ratios are taken. For each comparison are listed the averages (avg), and the standard deviations (std) of the ratios of the frequency scatters, the ratios of the line-width scatters and, if applicable, the ratios of the a_1-splitting coefficient scatters. For the details of the calculation of these averages and standard deviations we refer to the text.

by the SK method had an enormous amount of scatter in comparison with that of the a_1-splitting coefficients produced by either the JS or MPTS methods.

5.4.4. *Formal uncertainty comparisons*

Because the frequency uncertainties produced by the different methods are important input quantities in structural inversions, such as the two that we will be showing in Section 6, while the frequency-splitting coefficients are important input quantities for rotational inversions, such as those we will be showing in Section 7, we have compared the frequency uncertainties that were produced by all five methods and we have also compared the a_1 uncertainties produced by three of the methods in order to search for possible systematic differences in both types of uncertainties. For example, in the upper four panels of Figure 23 we show scatter plots in which the 1σ frequency uncertainties from the MPTS method are plotted as the abscissas, while the 1σ frequency uncertainties from the other four methods are plotted as the ordinates. Because of a few outlying uncertainties in three of these panels, the x- and y-axis scales are quite different, and hence we have included a dashed red line to indicate where equal frequency uncertainties would fall within each panel. While it is difficult to see the different numbers of points that fall above and below the dashed line in the upper two panels of Figure 23 because so many of them fall on top of each other, in both panels 87 percent of the points actually fall below the red line. Hence, these two panels make it clear that both the WMLTP and WMLTP_ac methods produced systematically smaller frequency uncertainties than did the MPTS method. In the middle-left panel the majority of the points lie above the dashed line, but there are four distinct sub-sets of the points for which the JS frequency uncertainties are much smaller than their MPTS counterparts. The green box in this panel shows that one of these groups of points comes from the low-degree portion of the $n = 0$ ridge. In the middle-right panel all 4719 of the points fall above the dashed line, which indicates clearly that the SK method produces systematically larger frequency uncertainties than does the MPTS method. Again in this panel we have placed a green
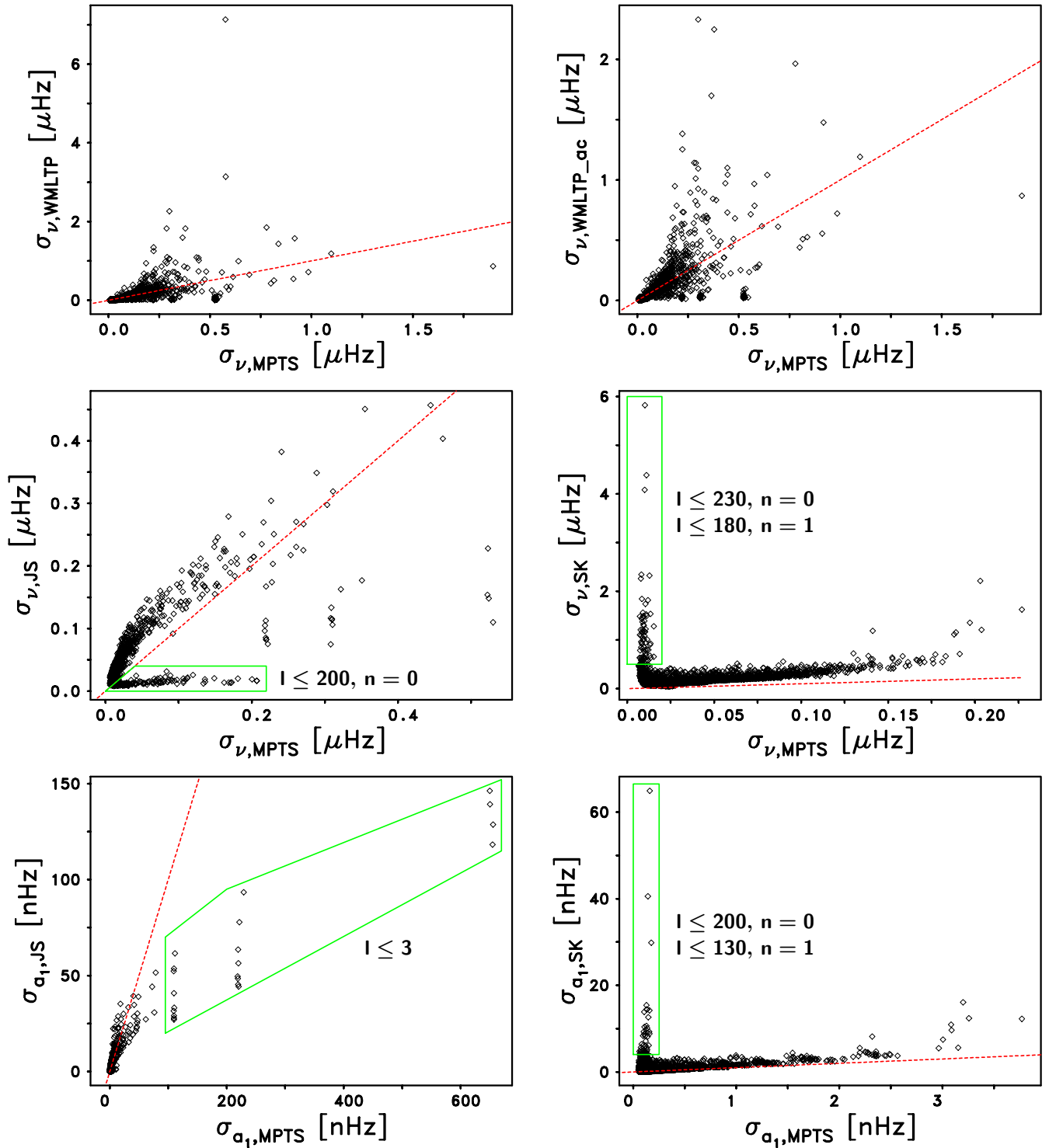
Figure 23. Comparison of 1σ frequency (upper and middle panels) and 1σ a_1-splitting coefficient uncertainties inferred from the methods as specified in the subscripts of the axis labeling. The subscript wmltp_ac refers to the variant of the WMLTP method in which the segments of the raw spectra are collapsed into the m-averaged spectrum within the WMLTP code rather than collapsing them outside the code, using the frequency-splitting coefficients obtained from the MPTS method. The modes predominantly contained in the green framed areas are specified in the panels. The red dashed line in the panels is for an equal uncertainty at the abscissa and the ordinate. We note the different scales of the axes.

Table 9.   Comparison of the MPTS method with the WMLTP, WMLTP_ac, JS, and SK methods in terms of ratios of frequency uncertainties, ratios of line-width uncertainties, and ratios of a_1-splitting coefficient uncertainties.

uncertainty ratio	frequency		line width		a_1	
	avg	std	avg	std	avg	std
WMLTP / MPTS	0.770	0.428	1.433	10.789	$\cdots$	$\cdots$
WMLTP_ac / MPTS	0.749	0.399	1.975	16.921	$\cdots$	$\cdots$
JS / MPTS	2.311	0.877	1.220	2.384	1.579	0.572
SK / MPTS	8.648	19.921	0.590	0.458	4.313	11.151
WMLTP_ac / WMLTP	0.989	0.212	0.991	0.215	$\cdots$	$\cdots$

NOTE— The first column indicates which method is compared with which, and in which sense the ratios are taken. For each comparison are listed the averages (avg), and the standard deviations (std) of the ratio of the frequency uncertainties, the ratio of the line-width uncertainties and, if applicable, the ratio of the a_1-splitting coefficient uncertainties.

box around the points that correspond to the low-degree portions of the $n = 0$ and $n = 1$ ridges. The points in this box correspond to extremely high ratios of the SK frequency uncertainties relative to the MPTS frequency uncertainties.

In the two bottom panels of Figure 23 we show scatter plots in which the $1\,\sigma\ a_1$ uncertainties from the MPTS method are plotted as the abscissas, while the $1\,\sigma\ a_1$ uncertainties are plotted as the ordinates for the JS and SK methods. With the exception of the group of low-degree points that are surrounded by the green box in the bottom-left panel, all of the other a_1 uncertainties from the JS method turned out to be very similar to the corresponding a_1 uncertainties from the MPTS method. On the other hand, as shown in the bottom-right panel, the vast majority of the a_1 uncertainties that were computed by the SK method were larger than their counterparts from the MPTS method. The points contained within the green box in this panel indicate that for low degrees, the SK method produced dramatically larger a_1 uncertainties than did the MPTS method.

While the panels of Figure 23 contained scatter plots, in Table 9 we present the average uncertainty ratios for the different methods. As can be seen in the second column of this table, both the WMLTP and the WMLTP_ac method deliver average frequency uncertainties which are only about three-fourths of the MPTS uncertainties. These average ratios confirm the comments we made above about the two upper panels of Figure 23. On the other hand, the third entry in the second column of Table 9 shows that the JS method provides frequency uncertainties which are on average roughly twice as large as those produced by the MPTS method, while the fourth entry in this column shows that the frequency uncertainties from the SK method are nearly nine times larger than those from the MPTS method. The bottom row of this column shows that the WMLTP and WMLTP_ac methods produce nearly-identical frequency uncertainties.

The fourth column of Table 9 shows that the WMLTP method delivers line-width uncertainties which are 43 percent larger than the MPTS method, while the WMLTP_ac method delivers line-

width uncertainties which are almost twice as large as those estimated by the MPTS method. The third row of this column shows that the line-width uncertainties from the JS method are 22 percent greater than those from the MPTS method. On the other hand, the fourth line of this column shows that the line-width uncertainties from the SK method are almost a factor of 2 times smaller than those obtained from the MPTS method. The rather large standard deviations of the WMLTP/MPTS and WMLTP_ac/MPTS line-width uncertainty ratios can be explained by the fact that for the low-n ridges ratios up to 500 and larger are to be observed. This is due to the circumstance that for lower degrees of the low-n ridges the line widths obtained from the MPTS method are systematically smaller than the line widths obtained from the WMLTP method, as was demonstrated in the middle panels of Figure 19. For those cases the MPTS code seems to deliver unrealistically small uncertainties of the line widths. The last row of this column shows that the WMLTP and WMLTP_ac methods produce nearly-identical line-width uncertainties.

The sixth column of Table 9 shows that the a_1 uncertainties from the JS method are comparable to those inferred by the MPTS method. As was shown in the left bottom-row panel of Figure 23, however, for low-degree modes the uncertainties from the MPTS method are much larger than those from the JS method. Also, as we just mentioned, in the bottom-right panel of Figure 23, some of the modes from the $n = 0$ and $n = 1$ ridges contribute to a large extent to the average ratio of 4.3 of the SK and the MPTS a_1 uncertainties that is shown in Table 9.

6. HELIOSEISMIC INVERSION FOR SOLAR STRUCTURE

Using the standard inversion procedure for the solar sound-speed profile of Kosovichev (1999), we inverted the 6,677 frequencies and their uncertainties to get the structural inversion shown in red in Figure 24. For comparison we overlaid in black the inversion profile that was obtained by a structural inversion of the 6,685 WMLTP frequencies and the uncertainties thereof. We note that both sets of frequencies covered the same frequency range from 965 to 4600 μHz. As can be seen, both inversion profiles agree extremely well for fractional radii between 0.55 and 0.975. In the shallow sub-surface layers, the two inverted sound-speed perturbation profiles differ significantly only for the outermost two mesh points. The magnitude of the near-surface dip at the next-to-the-last mesh point in the MPTS profile is roughly 29 percent deeper than the corresponding dip in the WMLTP profile. On the other hand, the turn-up that is shown between that dip in the WMLTP profile and the last mesh point of that profile is about 20 percent larger than is the corresponding rise in the MPTS profile. Both of these differences in the two perturbation profiles are likely due to the statistically-significant deviations of the MPTS and WMLTP frequencies in the outer layers of the Sun that we presented in the upper-left panel of Figure 20. Even though the sizes of the turn-ups in the MPTS and WMLTP profiles are not identical, we believe that these turn-ups do show the value of including frequencies above 4500 μHz in all future structural inversions since no such turn-up was seen in the inversion profile that we presented in Figure 26 of Paper I. That inversion was obtained with the rev6 version of the WMLTP method (cf. Appendix B) when applied to the $\mathcal{S}$2010_66a set of m-averaged spectra; however, the rev6 frequency table that was used to generate that inversion was limited to frequencies of 4500 μHz, while both of our MPTS and rev7 WMLTP inversions came from frequencies that extended up to 4600 μHz. We will demonstrate the absence of this near-surface turn-up in Figure 32 in the Appendix where we will show the profile from Paper I along with the rev7 profile and a newer rev6 profile that also came from frequencies that extended up to 4600 μHz.
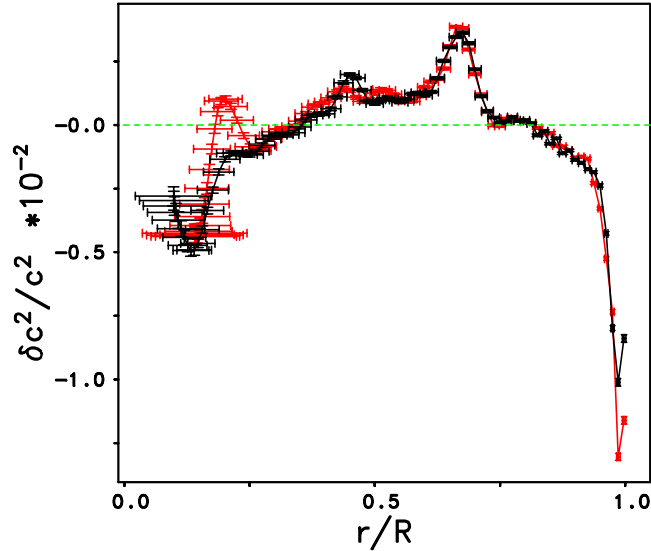
Figure 24. In red are shown the relative squared sound-speed deviations from the Standard Solar Model S of Christensen-Dalsgaard et al. (1996) in the sense "Sun minus Model" as a function of fractional radius, r/R, that we obtained by a structural inversion of the 6,677 MPTS frequencies and their uncertainties. The horizontal bars represent the width ("spread") of the localized averaging kernels, providing a characteristic of the spatial resolution, while the vertical bars are the 1σ formal error estimates. For comparison is overlaid in black the inversion profile that we obtained by a structural inversion of the 6,685 WMLTP frequencies and their uncertainties. Both sets of frequencies covered the same frequency range from 965 to 4600 μHz. The dashed green line is for a deviation of zero.

In the deep interior, below a fractional radius of about 0.25, the profiles show two major differences. First, the MPTS profile (i.e., the red curve) shows a large bump that extends above a deviation of zero that is not seen in the WMLTP profile. Second, while both profiles show a turn-up below the local minimum around fractional radius of 0.13, this turn-up is substantially smaller in magnitude in the MPTS profile than it is on the WMLTP profile even though only the larger turn-up is visible at the scale of the figure. Unfortunately, the 66-day observing run on which both profiles are based upon is too short for getting sufficiently accurate lower degree mode frequencies to identify either the bump and the decline of the MPTS profile or else the upward trend of the WMLTP profile as real features. We plan to investigate the sources of systematic errors that affect an inversion profile not only in the deeper interior but also close to the surface in an upcoming study. Such study requires, however, observing runs lasting longer than 66 days and which are, furthermore, from different epochs.

As we have already mentioned in Section 5.4.4, both the WMLTP and WMLTP_ac methods produced systematically smaller frequency uncertainties than did the MPTS method. We do not have an explanation for these systematically-smaller frequency uncertainties, but in Paper I we described a method for adjusting the frequency uncertainties produced by the WMLTP method that we employed prior to conducting the structural inversion that we showed in Figure 26 of that paper and which we have also included again in Figure 32 of this paper. Once many of the small frequency uncertainties that the WMLTP method produced were adjusted using this procedure, the inverted sound-speed radial profile that resulted was noticeably smoother than was the original profile that we obtained from the inversion that employed the un-adjusted uncertainties. We expressly emphasize

that no artificial correction was needed for the MPTS frequency errors to get the red inversion profile shown in Figure 24.

In spite of the differences between the MPTS and WMLTP profile, as shown in Figure 24, our conclusions drawn in Paper I remain still valid. First, there is a substantial deviation from Model S near the surface which coincides with the sub-surface rotational shear layer. Second, the stratification of the convection zone and heat transport properties may be significantly different from the predictions of the mixing length theory (see, for example, Vitense (1953)). Third, the sound speed in both the outer half of the convection zone and in the sub-surface shear layer is systematically lower than the sound speed in the standard solar model.

7. HELIOSEISMIC INVERSION FOR SOLAR ROTATION

If the Sun were spherically symmetric, its oscillation frequencies would depend on n and l but not on m. Hence, for each pair (n, l) there would be a $(2l + 1)$-fold degeneracy. However, the rotation of the Sun breaks the spherical symmetry and lifts the degeneracy. Moreover, advection causes modes that propagate in the direction of solar rotation to have higher frequencies than modes with the same (n, l) propagating in the opposite direction. The magnitude of this "rotational frequency splitting" is determined by the rotation rate in the region where a given mode is trapped. Since each mode of solar oscillation is trapped in a different region, it is possible to infer the rotation rate in the solar interior as functions of radial distance and heliographic latitude by studying the frequency-splitting coefficients (cf. Equation (25)) for all these modes (see, for example, Thompson et al. 1996, 2003). Here we have used a standard two-dimensional regularized least-squares (RLS) technique, which seeks to balance fitting the data with the smoothness of the solution (see, for example, Schou et al. 1992, 1994). To get the internal angular velocity distribution shown in the left-hand panel of Figure 25, we inverted the 6,655 frequency splittings and their uncertainties that were computed by employing the MPTS method on the power spectra obtained from the $\mathcal{R}2010\_66$ observing run. The trade-off parameters, which serve to suppress rapid variations in an RLS inversion, were assigned values of 10^{-4} and 10^{-2} for the radial and latitudinal regularization terms, respectively (see Equation (28) of Larson & Schou 2015). We note that the $\mathcal{R}2010\_66$ observing run extended over more than two consecutive solar rotations, so that short-lived dynamical structures associated with individual active regions would have been averaged out of the inversion. For comparison we show in the right-hand panel of Figure 25 the internal angular velocity distribution obtained from the same set of data, except that only modes with degrees $l \leq 300$ were taken into account in the inversion procedure. The most-notable differences between the two inversions appear between fractional radii of 0.95 and 1.0 at the middle-latitudes. It seems that the high-degree inversion (left panel) has smoother near-surface angular velocity gradients at latitudes between 45 and 60 degrees. In both panels the contours very near the surface clearly indicate that the rotation rate decreases outwards, at low and intermediate latitudes. This corresponds to the behaviour inferred from surface markers presumed to be anchored at different depths, and is reminiscent of the early results of Deubner et al. (1979).

To illustrate the improvement in the inversions from adding the higher degree modes, Figure 26 shows cuts in radius of selected averaging kernels. An averaging kernel determines how the inversion actually averages the rotation rate over the interior of the Sun. For the targets near the surface (bottom row) the kernels are substantially narrower and have a weaker tail toward the center. At the same time, the noise is decreased. For the deeper targets, the kernels have reduced contributions
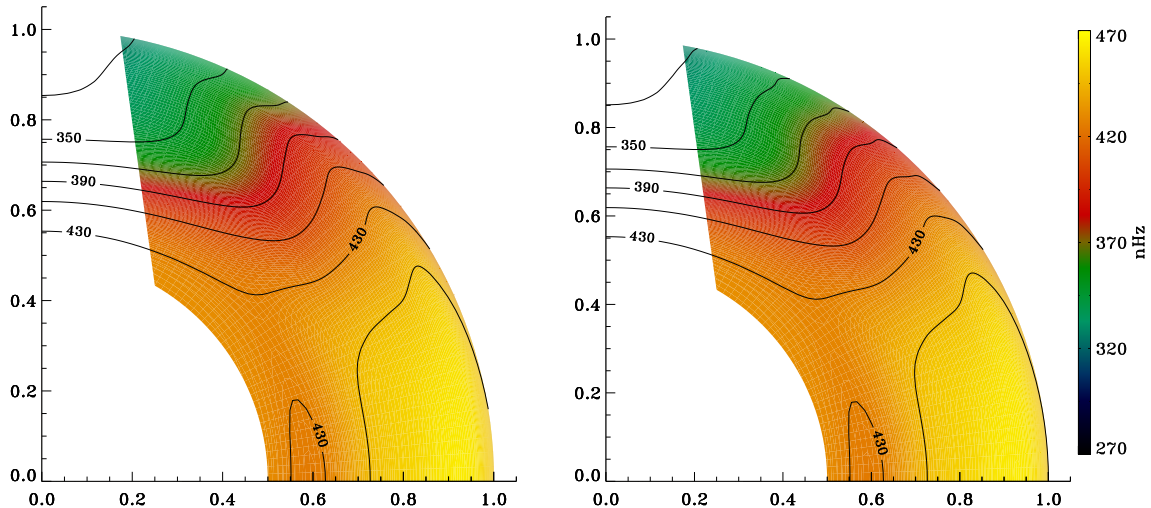
Figure 25. (Left) Inferred rotation rate in a quadrant of the Sun, obtained by means of inversion of the set of MPTS frequency-splitting coefficients derived from the $\mathcal{R}2010\_66$ observing run using modes with degrees up to $l = 1000$. The equator is at the horizontal axis, and the pole is at the vertical axis. Both axes are labelled by fractional radius. From regions where the estimates of the rotation are deemed unreliable we have erased color while retaining the contours for ease of labeling. The contour spacing is 20 nHz; the highest contour line is at 450 nHz. (Right) Same as left panel, except that from the table of the MPTS frequency-splitting coefficients only modes with degrees up to $l = 300$ were taken into account in the inversion procedure. The color key indicates the rotation rate in nHz.

near the surface and thus less contamination, while the errors are roughly the same. In other words, the inversion is substantially improved if higher degree modes are included.

In order to better highlight both the similarities and the differences between the two rotational inversions shown in Figure 25, we show in Figure 27 the radial profiles of the rotation rate along various latitudes. In the left-hand panel of Figure 27 the results from the high-degree inversion are shown, while we show those from the intermediate-degree inversion in the right-hand panel. The common features of both panels in Figure 27 include the Sub-surface Shear Layer (SSL, "leptocline") and the shear near the base of the convection zone ("tachocline") where the rotation rate shows a sharp transition from the differential rotation in the convection zone to a solid body like rotation in the radiative interior. The initial evidence of the SSL was presented by Rhodes et al. (1988) and by Korzennik et al. (1988). The results presented by Rhodes et al. (1990) suggested that the angular velocity increased with increasing depth beneath the photosphere in the SSL at low-, medium, and high-latitudes, which is consistent with the results shown in both panels of Figure 27. The most obvious differences to note between these two panels are the steeper near-surface radial gradients in the rotation rate of the intermediate-degree inversion (right panel) for latitudes greater than or equal to 45 degrees, as can also been seen in the left-hand panel of Figure 28.

It is generally believed that both shear layers play a crucial role for the solar dynamo (e.g., Charbonneau 2010). However, there is some controversy in the literature as to whether the near-surface shear changes sign at higher latitudes. Such change of sign in the range from 30° to 60° latitude has been found by, for example, Thompson et al. (1996), Kosovichev et al. (1997), and Corbard, & Thompson (2002). Barekat et al. (2014) found a change of sign as well, but at about 75° latitude. On the other hand, Rhodes et al. (1990), and Corbard et al. (2013) found no indication at
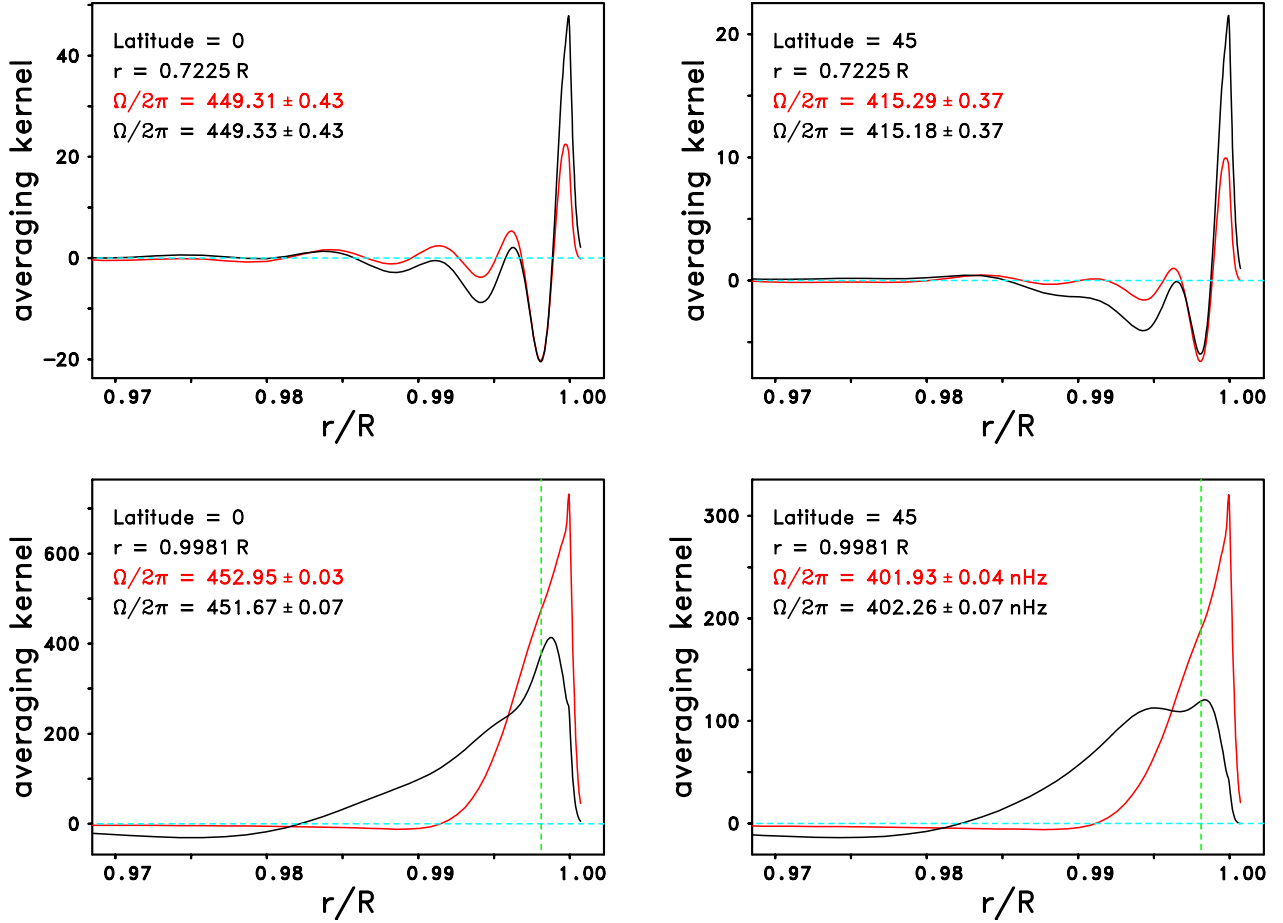
Figure 26. Averaging kernels as function of fractional radius, r/R, for two latitudes and two different target radii, r, where R is the radius of the Sun. The kernels shown in red were inferred from the set of MPTS frequency-splitting coefficients obtained from the $\mathcal{R}2010\_66$ observing run using modes with degrees up to $l = 1000$, while those shown in black include only modes with degrees up to $l = 300$. In each panel the rotation rate, $\Omega/2\pi$, and its associated uncertainty at approximately the target radius and latitude is shown in red when inferred from the mode set up to $l = 1000$, while it is shown in black when inferred from the mode set up to $l = 300$. The vertical dashed green lines in the bottom row represent the locations of the target radii of the averaging kernels. In the top row those lines are outside the plotting range. We note, however, that for the two cases shown in the top row the kernels are essentially identical near the target radius. The horizontal dashed turquoise lines represent the zero-line. The different scalings of the vertical axes in the panels are to be noted.

all of a reversal in the sign of the radial gradient, in agreement with our results shown in Figure 27 and the left-hand panel of Figure 28, respectively.

In their comparative study of GONG and MDI data, Schou et al. (2002) concluded that the most significant differences in the rotational inversions arise not from the observations themselves but from the different frequency estimation analyses used by the two projects. Specifically, they found that the GONG pipeline results in substantially fewer fitted modes in certain regions of the l-ν plane. The most serious systematic differences in the results regarding the rotational inversions appear to be an anomaly in the MDI odd-order splitting coefficients around a frequency of 3.5 mHz and an underestimation of the low-degree rotational splittings in the GONG algorithm. The results from this
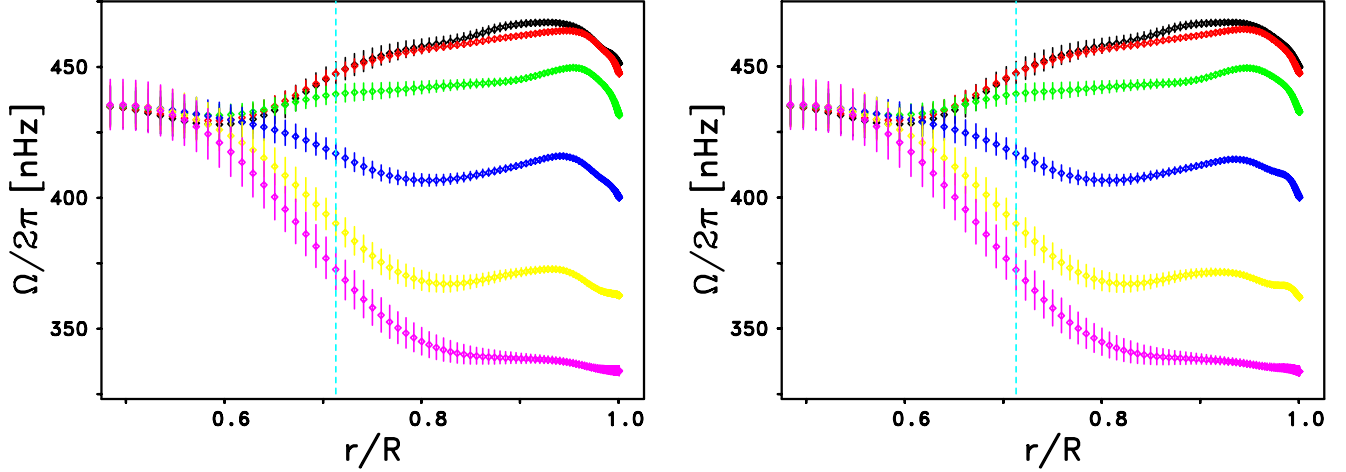
Figure 27. (Left) Rotation rate, $\Omega/2\pi$, measured in nHz, at latitudes of 0 (black), 15 (red), 30 (green), 45 (blue), 60 (yellow), and 75 (magenta) degrees as a function of fractional radius r/R, as inferred from the set of MPTS frequency-splitting coefficients obtained from the $\mathcal{R}2010\_66$ observing run using modes with degrees up to $l = 1000$. Here, r is the radial distance from the center, and R denotes the radius of the Sun. The vertical dashed turquoise line marks the lower boundary of the convection zone. The error bars along each rotation profile represent $1\,\sigma$ formal uncertainties that were enlarged by a factor of 10. (Right) Same as left panel, except that from the table of the MPTS frequency-splitting coefficients only modes with degrees up to $l = 300$ were taken into account in the inversion procedure.

comparative study may explain in some respects the different findings regarding the high-latitude reversal of the near-surface shear. However, it is to be noted that all previous studies of this shear did not include any high-degree splitting coefficients.

In order to quantify the differences in the shape of the radial gradient of the angular velocity that resulted from the two different rotational inversions that were shown in Figures 25 and 27, we computed the logarithmic radial gradient, $\mathrm{d}\ln\Omega/\mathrm{d}\ln r$, of the angular velocity at the solar surface as a function of heliographic latitude. The latitudinal dependence of the two different sets of radial gradients are shown in the left-hand panel of Figure 28, with the gradient that resulted from the high-degree inversion being shown in red and the gradient that resulted from intermediate-degree inversion being shown in black. It is apparent that these two curves are quite different in the magnitudes and locations of the peak gradients and in the widths of those peaks. The logarithmic radial gradient that was derived from the high-degree inversion peaks close to a value of -2.8 at a heliographic latitude of 28.1 degrees. This latitude is very similar to the latitude of the poleward side of the branch of the torsional oscillation that was approaching the solar equator during mid-2010. On the other hand, the logarithmic radial gradient from the intermediate-degree inversion peaks around -2.2 and that peak is much wider and farther away from the solar equator than the peak in the gradient from the high-degree inversion. To see how closely the location of the steepest radial gradient of the angular velocity at the top of the SSL corresponded to the locations of the sunspots that were visible on the sun during the 2010 Dynamics Run, we employed a set of hourly HMI continuum intensity images that were obtained during that 66-day time interval. We then located all of these sunspots in the HMI images and we converted their pixel coordinates into the heliographic latitudes and Carrington longitudes. The latitudes of these spots are shown as a function of time in the right-hand panel of Figure 28. Out of the 407 sunspots, 384 of them had absolute values of their latitudes that were
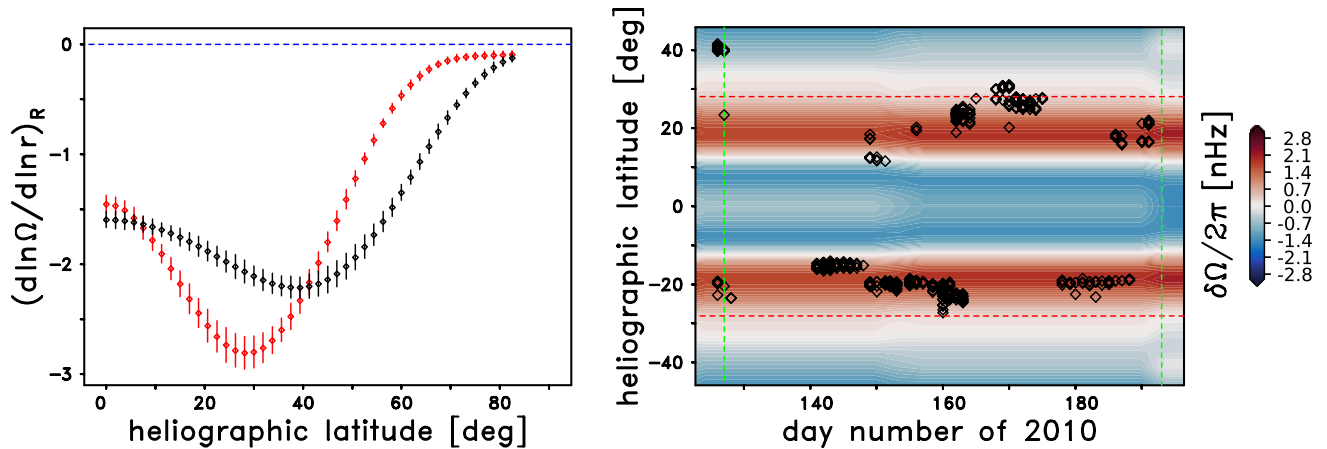
Figure 28. (Left) Logarithmic radial gradient of the rotation rate, $\mathrm{d}\ln\Omega/\mathrm{d}\ln r$, evaluated at the solar surface as a function of latitude. The high-degree inversion is shown in red, while the intermediate-degree inversion is shown in black. The error bars along each curve represent $1\,\sigma$ formal uncertainties that were enlarged by a factor of 100. The dashed horizontal blue line represents $\mathrm{d}\ln\Omega/\mathrm{d}\ln r = 0$. (Right) Heliographic latitude of individual sunspots as a function of the day of the year 2010, as inferred from HMI continuum intensity images. Color coded are superimposed the rotation-rate residuals, $\delta\Omega/2\pi$ measured in nHz, at a target depth of 0.99 fractional radii as a function of latitude and time, as inferred from RLS inversions of GONG, MDI, and HMI data. The mean to be subtracted was taken separately over the whole data set for GONG and for the combined MDI and HMI set. The horizontal dashed red lines delimit the range of heliographic latitudes between ± 28.1 degrees. The vertical dashed green lines mark the start and end of the 2010 MDI Dynamics Run on May 7th and July 11th, respectively.

less than or equal to 28.1 degrees, or 94.35 percent. Only 23 of these spots were located at higher latitudes than the location of the peak radial gradient from the high-degree inversion, and most of those spots were located within a single active region at the beginning of the time interval.

The different colored bands that underlie the locations of the sunspots in the right-hand panel of Figure 28 are a set of rotational residuals computed by R. Howe (2019, private communication). These residuals were computed by the subtraction of a temporal mean from a two-dimensional rotational inversion of a combination of GONG, MDI, and HMI frequency-splitting coefficients. The two red bands show the latitudes where the angular velocity at a sub-photospheric depth of $0.01\,R_{\mathrm{sun}}$ was faster than the average angular velocity at that depth. Both of these bands represent the branch of the solar torsional oscillation that was moving toward the solar equator during mid-2010. Both of these red bands can clearly be seen to agree closely with the locations of the overwhelming majority of the sunspots that we identified in the HMI images. In addition, both of these bands appear to be bounded on their poleward sides by the two dashed red lines that denote the ± 28.1 degree latitudes where the absolute value of radial gradient of the surface angular velocity (i.e., the black curve in the left-hand panel of Figure 28) reached its peak value in our high-degree rotational inversion. By contrast, the latitude of 39.4 degrees at which the radial gradient of the angular velocity went through its peak value in our intermediate-degree inversion (i.e., the red curve in the left-hand panel of Figure 28) shows no correlation with the locations of the majority of the sunspots.

8. CONCLUDING REMARKS AND OUTLOOK

Global helioseismology, that is the study of the Sun by means of its normal modes of oscillations, has revolutionized our knowledge of the Sun by revealing its large-scale structure and rate of rotation as functions of radial distance and heliographic latitude with unprecedented accuracy. However, what is still missing is an improved understanding of the near-surface layers of the Sun. These layers are believed to play a crucial role in the formation of the magnetic network, active regions, and sunspots, and thus are a key to the understanding of the mechanisms of solar activity and variability, at present possibly the most important unsolved problem in solar physics.

A straightforward approach to study the near-surface layers of the Sun is to employ precise frequencies of high-degree modes. Unfortunately, those modes do not appear as isolated, sharp peaks in the power spectra but rather as broad ridges of power. This is mainly for two reasons. First, any power spectrum computed for a specific target mode (l, m) contains contributions of power from modes with neighboring l and m because the spherical harmonic functions used in the spatial decomposition of the observed Dopplergrams are not orthogonal on that part of the Sun we observe. These so-called spatial leaks are quantified by the leakage matrices. Second, with increasing degree the mode line width increases with both frequency and degree, while the frequency separation of the spatial leaks decreases. As a result, individual modal peaks blend together to form ridges of power. Since the amplitudes of the spatial leaks are asymmetric with regard to the target mode, the central frequency of a ridge is significantly offset from the target mode frequency. Therefore, the distribution of power in a ridge cannot be simply represented by using just a single symmetrical or asymmetrical function of frequency.

In Section 3 we presented the mathematical details of how this issue can be overcome by employing a fitting profile that consists of the sum of numerous individual overlapping profiles whose relative amplitudes are determined by the leakage matrix appropriate to the targeted mode. We named the resulting fitting methodology the MPTS method. As we described in Paper I, we implemented a similar approach for the fitting of m-averaged spectra. We named that methodology the WMLTP method. A key aspect of both the MPTS and WMLTP methods is the fact that they are equally well-suited for the estimation of low-, medium-, and high-degree mode parameters since they both are able to provide modal characteristics for narrow modal peaks as well as for broad ridges of power. The major distinction between the two methods is the fact that the MPTS method is able to produce frequency-splitting coefficients along with its estimates of the modal parameters, while the WMLTP is not able to provide any such frequency-splitting coefficients. On the contrary, a table of frequency-splitting coefficients has to be supplied to the WMLTP code as part of the process of generating the m-averaged spectra that this method requires.

With the MPTS method a powerful tool for determining low-, intermediate-, and high-degree mode parameters including the frequency-splitting coefficients is available. We hope that this new method will lead to a renaissance of global helioseismology because it allows addressing the following important questions. First, investigation of temporal changes in the structure and the angular velocity of the solar interior in general and of the sub-surface layers in particular in dependence of the solar cycle using the extensive sets of observations by the HMI instrument on-board the SDO spacecraft. Second, investigation of the effects of magnetic fields on the convective energy transport and irradiance variations in the course of the solar cycle by comparing the properties of the solar internal structure, as obtained from inversions for the adiabatic exponent, density, and the parameter of

convective stability, with the results of realistic numerical 3D MHD simulations of the convective energy transport in the upper convection zone, carried out for different background magnetic field strengths, and by employing simultaneous irradiance measurements made by the SDO/EVE instrument. Third, measurement of large-scale flows in the solar interior. The recent development of the EigenFunction Perturbation Analysis (EFPA) by Schad et al. (2011) opens the path to probe flows in the solar interior which have only a tiny effect on global oscillation frequencies because of their symmetry (Roth, & Stix 2008). An example of such flow is the meridional circulation in the solar interior. The EFPA is based on the perturbation of the p-mode eigenfunctions of a solar model due to the presence of a flow. The distortion of the eigenfunctions is manifested in the mixing of p-modes, which may be measured by means of global helioseismic techniques (Schad et al. 2013). Fourth, determination of the solar heavy-element abundance. Recent analyses of spectroscopic data have suggested that the heavy-element abundance Z needs to be revised downward significantly, from Z=0.017 (Grevesse & Sauval 1998) to Z=0.012 (Grevesse et al. 2007). This new value of Z results from the use of a 3D hydrodynamic model of the solar lower atmosphere instead of the classical 1D hydrostatic models, accounting for departures from local thermodynamic equilibrium (LTE) in the line formation, and improved atomic and molecular data. However, solar models constructed with this low heavy-element abundance do not satisfy helioseismic constraints. Rather they are found to have an incorrect depth of the convection zone, an incorrect helium abundance Y, and the sound speed and density profiles of the models do not match that of the Sun. This discrepancy constitutes of what is known as the "solar abundance problem". This has led to attempts to determine the solar heavy-element abundance utilizing helioseismic techniques (Antia & Basu 2006; Buldgen et al. 2017; Vorontsov et al. 2013). Such determinations will be greatly helped by the access to reliable high-degree mode frequencies.

APPENDIX

A. DERIVATION OF THE VALUE OF THE CONSTRAINT TO BE APPLIED TO THE LINE ASYMMETRY PARAMETER

The model profile given in Equation (1) is based on the asymmetrical profile of Nigam & Kosovichev (1998) which can be written as

$$L(\nu) = \frac{(1 + Bx)^2 + B^2}{1 + x^2},$$ (A1a)

with

$$x = \frac{2(\nu - \nu_0)}{w_0}.$$ (A1b)

Here, ν is frequency, B is a measure of the line asymmetry, and ν_0 and w_0 are, respectively, the frequency and the line width of the targeted peak. Theoretically, the line asymmetry can be as high as one half of the line width itself. However, in the derivation of the profile $L(\nu)$ it has been assumed that the line asymmetry is much smaller than this.

The line width, w, of the profile $L(\nu)$ may be calculated as follows. First, solving the equation

$$L(x) = \frac{(1 + Bx)^2 + B^2}{1 + x^2} = \frac{1}{2}$$ (A2)

for x gives the two solutions

$$x_1 = \frac{2B + \sqrt{4B^2(1 - B^2) + 1}}{1 - 2B^2}, \quad x_2 = \frac{2B - \sqrt{4B^2(1 - B^2) + 1}}{1 - 2B^2},$$ (A3)

respectively. For $|B| \ll 1$, we get

$$x_1 = +1 + 2B + \mathcal{O}(B^2), \quad x_2 = -1 + 2B + \mathcal{O}(B^2),$$ (A4)

respectively. Second, solving equation (A1b) for ν we get

$$\nu = \nu_0 + x \frac{w_0}{2}.$$ (A5)

Hence, the line width, w, is given by

$$w = \nu_1 - \nu_2 = \nu_0 + x_1 \frac{w_0}{2} - (\nu_0 + x_2 \frac{w_0}{2}) = (x_1 - x_2) \frac{w_0}{2},$$ (A6)

presuming that $x_1 \geq x_2$. Inserting equation (A3) into equation (A6), we get

$$w = \lambda w_0,$$ (A7)

with

$$\lambda = \frac{\sqrt{4B^2(1-B^2)+1}}{1-2B^2}. \tag{A8}$$

Of course, for $B = 0$ we get $w = w_0$. It can be shown that

$$\lambda = 1.5 \quad \text{for} \quad |B| \approx 0.3283, \tag{A9}$$

i.e., for this value of B the line width is increased by one half of its genuine value due to asymmetry. To be safe, for the reason given above, we recommend that B should be kept within the following range:

$$|B| \leq 0.20. \tag{A10}$$

This restriction allows a maximum line broadening due to asymmetry by a factor of 1.167, as can be seen by inserting Equation (A10) into Equation (A8).

## B. MIGRATION OF WMLTP METHOD FROM VERSION REV6 TO VERSION REV7

The migration of the WMLTP method from version rev6 to version rev7 consists of the following three major changes. First, for ridges with radial order $n \leq 8$ the quadratic background model (cf. Section 4.2 of Paper I) is now enforced to significantly improve the quality of the fits. The range of degrees for which the quadratic background model is used depends on n. For example, the quadratic background model is enforced for $l \leq 350$ for $n = 0$, for $l \leq 50$ for $n = 3$, and for $l \leq 4$ for $n = 8$. For ridges $n > 8$ the linear background model is used throughout. We note that the degree cutoffs between the quadratic and the linear background models were made by visual inspection of the different segments of the power spectra themselves. The impact of the use of the quadratic instead of the linear background model on the fitted profile is shown here in Figure 29 for the $(n, l) = (1, 60)$ and $(9, 60)$ modes. Second, following the reasoning that we have made in Appendix A, the magnitude
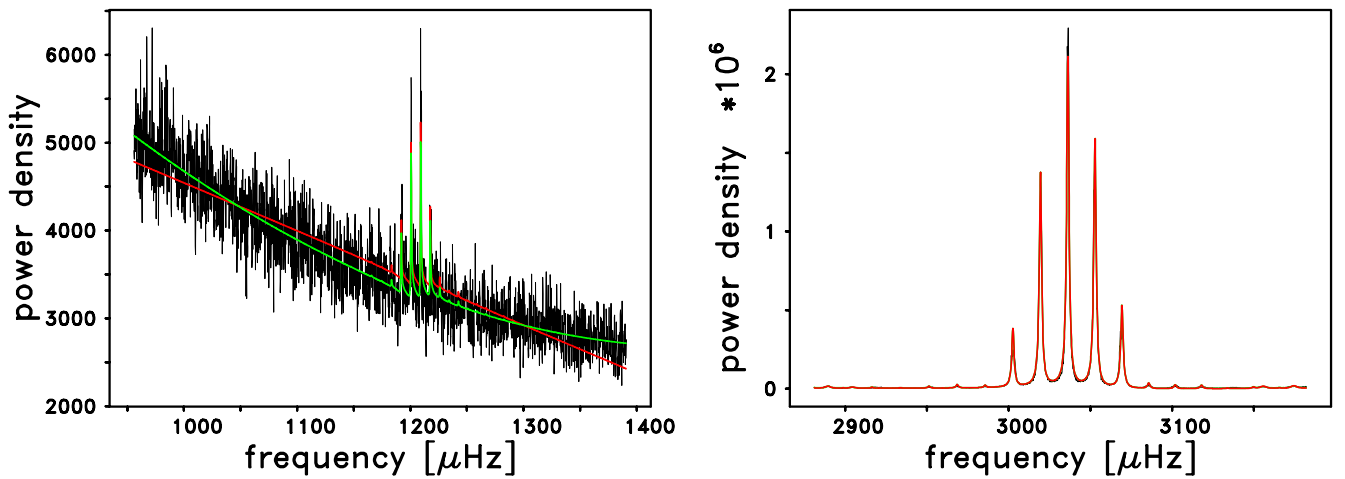

Figure 29. Fits to segments of two different m-averaged spectra that were centered around the frequency of the $(n, l) = (1, 60)$ (left) and the $(9, 60)$ (right) mode. In each panel the black line is for the m-averaged spectrum, the green line is for the fitted profile using the quadratic background model, and the red line is for the fitted profile using the default linear background model. The power density is measured in uncalibrated units. In the right-hand panel the green and the red line match within drawing accuracy, justifying the use of the linear background model. We note the different scales of the ordinates in the two panels.

of the line asymmetry of a fitted peak is now restricted to $|B| \leq 0.20$, instead of the constraint $|B| \leq 0.30$ which was used in the rev6 version. Third, in the rev6 version the m-averaged leakage matrix, $C_{n;l,l'}^{(\mathrm{mavg})}$, was approximated for a multiplet (n, l) by a Gaussian profile (cf. Section 4.1 of Paper I). As we have already pointed out in Paper I, this approximation can be improved upon. Therefore, we have replaced the Gaussian approximation to $C_{n;l,l'}^{(\mathrm{mavg})}$ by the following approach. As before, we first correct $C_{n;l,l'}^{(\mathrm{mavg})}$ for the latitudinal differential rotation (cf. Section 3.2.2 of Paper I). We then compute the m-averaged leakage matrix for a set of c_t values in the range $0 \leq c_t^{(n,l)} \leq 1$, for each multiplet (n, l). Here, c_t is the ratio of the horizontal and vertical components of the solar oscillation eigenfunctions, as shown in Equation (7) in Paper I. Instead of fitting Gaussians to them, as we have done in the rev6 version, we fit the individual elements of the leakage matrix as a function of c_t, using parabolæ. Because the leakage matrix covers the range $|l - l'| \leq 30$, we have a total of 61 such fits. For the $(2, 900)$ multiplet typical examples are shown here in Figure 30 for $l' = 886$ and $l' = 914$, respectively. As can be seen, the parabolic fits match well the run of the leakage matrix elements with respect to c_t. The resulting fit coefficients for each l' in the range $|l - l'| \leq 30$ are saved in a file. Then, during the fitting procedure of the multiplet (n, l) all elements of the corresponding leakage matrix can easily be recovered from these fit coefficients in the range $0 \leq c_t^{(n,l)} \leq 1$ for any degree l' in the range $|l - l'| \leq 30$.

In order to compare the frequencies computed by the two different versions of the WMLTP code, we employed the same limits of n, l, and ν that were listed in columns 2 through 4 of Table 5 for the rev7 WMLTP frequency table. With these limits, we were able to find a corresponding rev6 frequency for every rev7 frequency. We show the dependence of the 6,685 raw frequency differences on frequency, in the sense of $\nu(\mathrm{rev7}) - \nu(\mathrm{rev6})$, in the left-hand panel of Figure 31. This panel shows clearly that the vast majority of these frequency differences were quite small with only a small number of outlying differences. When we normalized the raw frequency differences by dividing them by their formal errors, we found that over 76 percent of them were statistically insignificant at the 3σ level. We show the dependence of the normalized rev7 $-$ rev6 frequency differences on the inner turning-point radii of those modes in the right-hand panel of Figure 31. This panel shows that a few of the largest
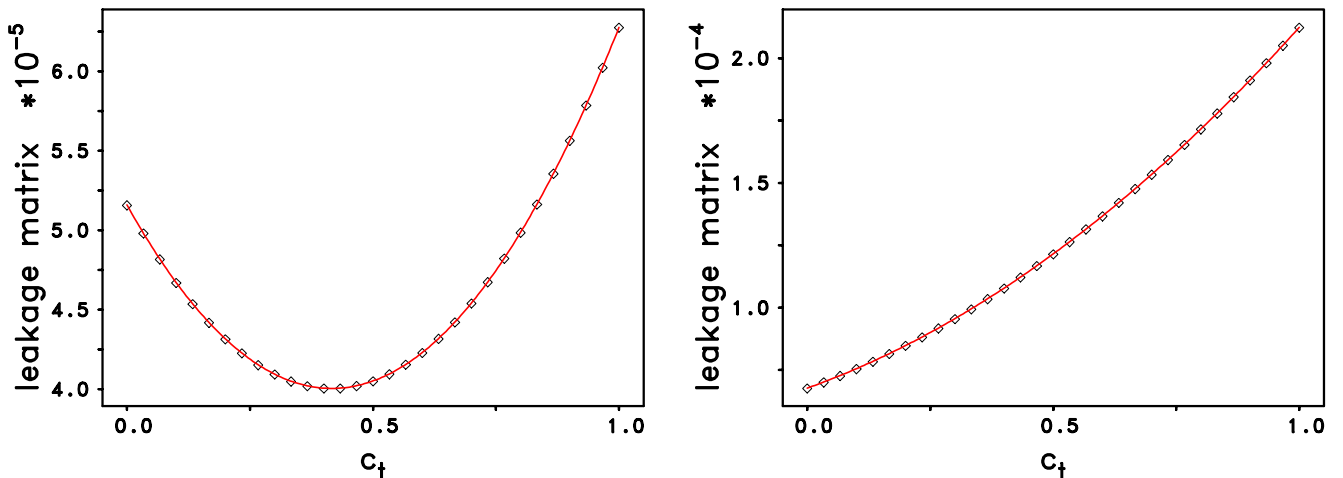
Figure 30. Fits of the leakage matrix elements for $l' = 886$ (left) and $l' = 914$ (right) as a function of c_t for the $(2, 900)$ multiplet. The diamonds are for the leakage matrix, while the red curve is for a parabolic fit. We note the different scales of the ordinates.
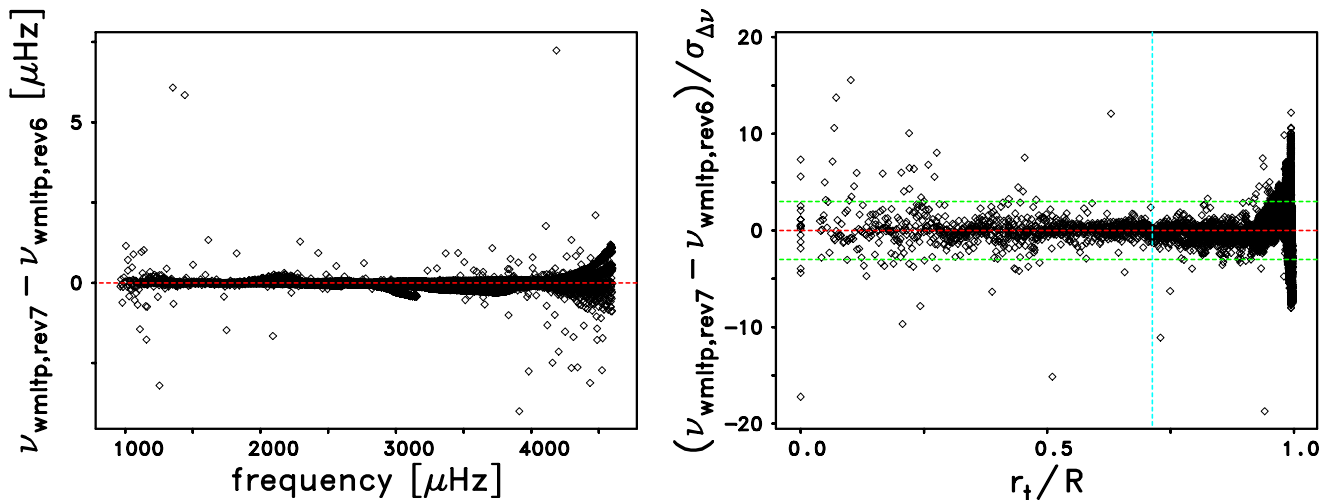
Figure 31. (Left) Frequency dependence of the raw differences between the WMLTP frequencies, $\nu_{\mathrm{wmltp,rev7}}$, and the frequencies, $\nu_{\mathrm{wmltp,rev6}}$, that were computed from the same m-averaged spectral set using the rev6 version of the WMLTP method. The dashed red line is for a difference of zero. (Right) Dependence of the normalized frequency differences on the inner turning-point radius, r_t/R, of the corresponding modes. Here, R is the radius of the Sun. The normalization was carried out by dividing the raw frequency differences, $\nu_{\mathrm{wmltp,rev7}} - \nu_{\mathrm{wmltp,rev6}}$, as shown in the left-hand panel, by the formal error, $\sigma_{\Delta\nu}$ of each difference. Not shown is the normalized frequency difference for the $(n, l) = (5, 12)$ mode which was $+57.2$ due to the fact that the rev6 frequency turned out to be an outlying case. The dashed red line is for a difference of zero, the dashed turquoise line marks the lower boundary of the convection zone, and the dashed green lines show the $\pm 3\,\sigma$ values.

normalized frequency differences corresponded to modes that extended into the deep solar interior. On the other hand, this panel also indicates that almost all of the other large normalized differences corresponded to modes that are confined within the convection zone. In addition to comparing the frequencies of the rev7 and rev6 versions of the WMLTP code, we also compared the two sets of frequency uncertainties. We found that the rev7 frequency uncertainties were only 3 percent larger than the rev6 uncertainties on the average.

Based upon the appearance of the right-hand panel of Figure 31, we had expected that the largest differences in the inverted sound-speed perturbations computed from the tables of rev7 and rev6 WMLTP frequencies would be located deeply within the solar interior, and that is precisely what the black and magenta profiles that are shown in the left-hand panel of Figure 32 indicate, with the largest differences occurring for the innermost mesh points. In particular, the magnitude of the dip in the magenta profile at a fractional radius of 0.13 is roughly one-half as deep as the dip in the black profile. On the other hand, the magnitude of the dip in the green profile, which came from the inversion of the older table of rev6 frequencies that we presented in Figure 26 of Paper I, is very similar to the magnitude of the same dip in the magenta profile. This similarity in the depth of this innermost dip in the sound-speed perturbation for the two rev6 profiles suggests that the deeper dip in the rev7 profile was due to the changes between the two different revisions of the WMLTP code.

While the scale of the left-hand panel of Figure 32 is adequate to show the differences in the deep-interior portions of all three inversions, this scale is not adequate to illustrate the differences in the near-surface profiles. Therefore, we show an enlargement of the outermost portions of these profiles in the right-hand panel of Figure 32. This panel shows that both the rev7 (black) and newer rev6
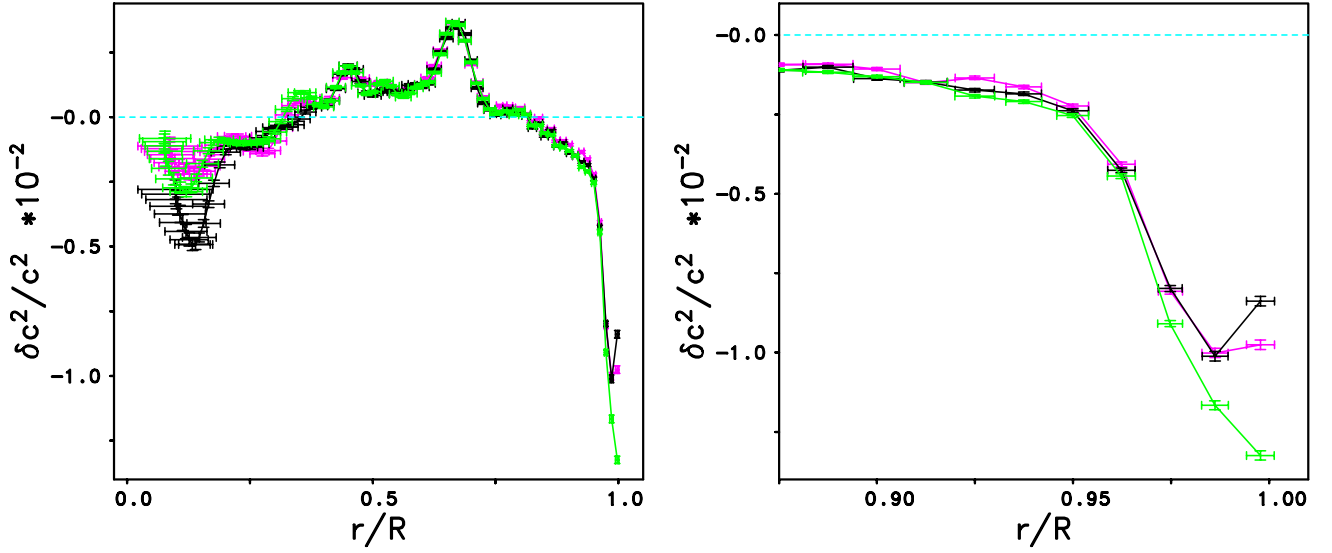
Figure 32. (Left) In black are shown the relative squared sound-speed deviations from the Standard Solar Model S of Christensen-Dalsgaard et al. (1996) in the sense "Sun minus Model" as a function of fractional radius that we obtained by a structural inversion of the 6,685 rev7 WMLTP frequencies and their uncertainties. This inversion profile is the same as that shown in black in Figure 24. The horizontal bars represent the width ("spread") of the localized averaging kernels, providing a characteristic of the spatial resolution, while the vertical bars are the 1σ formal error estimates. For comparison is overlaid in magenta the inversion profile that we obtained by a structural inversion of the 6,685 frequencies and their uncertainties that were computed from the same m-averaged spectral set using the rev6 version of the WMLTP method. We note that both sets of frequencies consisted of exactly the same mode set covering the frequency range from 965 to 4600 μHz. Also overlaid is in green the inversion profile that was shown in Figure 26 of Paper I. That profile was obtained by a structural inversion of the 6,366 frequencies and uncertainties thereof that were also computed from the same m-averaged spectral set using the rev6 version of the WMLTP method applying an upper frequency limit of 4500 μHz. (Right) Enlargement of the left-hand panel for fractional radii greater than 0.875 using the same color style. In both panels the dashed turquoise line is for a deviation of zero.

(magenta) profiles show a turn-up in the sound-speed perturbation between the outermost two mesh points just as we also saw in the inversion profile from our MPTS frequency table in Figure 24. On the other hand, the green profile in this panel does not show any change in the negative outward gradient in its profile. We mentioned this difference in the behavior of the profiles computed from the rev7 and the older rev6 inversions in our discussion of Figure 24, but now that we can see that the change in the sign of the radial gradient is a feature of all three inversions that included frequencies above 4500 μHz, it does appear that this feature is a signature of inversions that include frequencies that extend above that older limit.

In addition to comparing the frequencies and their uncertainties, we also compared the line widths that the two versions of the WMLTP code produced. We found that both the raw and normalized differences in the rev7 and rev6 line widths were insignificant on the average. Finally, when we computed the ratios of the rev7 line widths divided by the rev6 line widths, we found only a 6 percent difference from a ratio of 1.0, but the large standard deviation around that average makes it clear that this small deviation from a ratio of unity was not significant.

REFERENCES

Anderson, E. R., Duvall, T. L., Jr., & Jefferies, S. M. 1990, ApJ, 364, 699

Antia, H. M., & Basu, S. 2006, ApJ, 644, 1292

Bachmann, K. T., Duvall, T. L., Harvey, J. W., et al. 1995, ApJ, 443, 837

Barekat, A., Schou, J., & Gizon, L. 2014, A&A, 570, L12

Brown, T. M. 1985, Nature, 317, 591

Buldgen, G., Salmon, S. J. A. J., Noels, A., et al. 2017, MNRAS, 472, 7511

Charbonneau, P. 2010, Living Reviews in Solar Physics, 7, 3

Christensen-Dalsgaard, J., Dappen, W., Ajukov, S. V., et al. 1996, Science, 272, 1286

Corbard, T., & Thompson, M. J. 2002, SoPh, 205, 211

Corbard, T., Salabert, D., Boumier, P., et al. 2013, Fifty Years of Seismology of the Sun and Stars, 151

Deubner, F.-L., Ulrich, R. K., & Rhodes, E. J. 1979, A&A, 72, 177

Domingo, V., Fleck, B., & Poland, A. I. 1995, SoPh, 162, 1

Duvall, T. L., Jr., Harvey, J. W., & Pomerantz, M. A. 1986, Nature, 321, 500

Duvall, T. L., Jr., Harvey, J. W., Libbrecht, K. G., Popp, B. D., & Pomerantz, M. A. 1988, ApJ, 324, 1158

Frieden, B. R. 1983, Probability, Statistical Optics, and Data Testing: a Problem Solving Approach (Berlin: Springer)

Gough, D. O. 1977, IAU Colloq. 36: The Energy Balance and Hydrodynamics of the Solar Chromosphere and Corona, 3

Grevesse, N., & Sauval, A. J. 1998, SSRv, 85, 161

Grevesse, N., Asplund, M., & Sauval, A. J. 2007, SSRv, 130, 105

Harvey, J. W., Hill, F., Hubbard, R. P., et al. 1996, Science, 272, 1284

Hill, F., Stark, P. B., Stebbins, R. T., et al. 1996, Science, 272, 1292

Korzennik, S. G., Cacciani, A., Rhodes, E. J., et al. 1988, in Seismology of the Sun and Sun-like Stars, ed. E. J. Rolfe (ESA-SP 286; Noordwijk: ESA), 117

Korzennik, S. G. 1990, Ph.D. Thesis, California University, Los Angeles

Korzennik, S. G., Rabello-Soares, M. C., & Schou, J. 2004, ApJ, 602, 481

Korzennik, S. G., Rabello-Soares, M. C., Schou, J., & Larson, T. P. 2013, ApJ, 772, 87

Kosovichev, A. G., Schou, J., Scherrer, P. H., et al. 1997, SoPh, 170, 43

Kosovichev, A. G. 1999, Journal of Computational and Applied Mathematics, 109, 1

Larson, T. P., & Schou, J. 2015, SoPh, 290, 3221

Leighton, R. B., Noyes, R. W., & Simon, G. W. 1962, ApJ, 135, 474

Libbrecht, K. G., & Kaufman, J. M. 1988, ApJ, 324, 1172

Libbrecht, K. G., Woodard, M. F., & Kaufman, J. M. 1990, ApJS, 74, 1129

Menzel, D. H. 1960, Fundamental Formulas of Physics (New York: Dover)

Nigam, R., & Kosovichev, A. G. 1998, ApJL, 505, L51

Pesnell, W. D., Thompson, B. J., & Chamberlin, P. C. 2012, SoPh, 275, 3

Press, W. H., Teukolsky, S. A., Vetterling, W. T., & Flannery, B. P. 1992, Numerical Recipes in Fortran 77: The Art of Scientific Computing (New York: Cambridge Univ. Press)

Reiter, J., Rhodes, E. J., Jr., Kosovichev, A. G., Schou, J., & Scherrer, P. H. 2002, in SOHO11. From Solar Min to Max: Half a Solar Cycle with SOHO, ed. A. Wilson (ESA-SP 508; Noordwijk: ESA), 91

Reiter, J., Kosovichev, A. G., Rhodes, E. J., Jr., & Schou, J. 2003, in SOHO12/GONG+ 2002. Local and Global Helioseismology: the Present and Future, ed. H. Sawaya-Lacoste (ESA-SP 517; Noordwijk: ESA), 369

Reiter, J., Rhodes, E. J., Jr., Kosovichev, A. G., et al. 2015, ApJ, 803, 92 (Paper I)

Rhodes, E. J., Jr., Ulrich, R. K., & Simon, G. W. 1977, ApJ, 218, 901

Rhodes, E. J., Cacciani, A., Korzennik, S. G., et al. 1988, in Seismology of the Sun and Sun-like Stars, ed. E. J. Rolfe (ESA-SP 286; Noordwijk: ESA), 73

Rhodes, E. J., Cacciani, A., Korzennik, S., et al. 1990, ApJ, 351, 687

Rhodes, E. J., Jr., Reiter, J., Kosovichev, A. G., Schou, J., & Scherrer, P. H. 1998, in SOHO6/GONG98. Structure and Dynamics of the Interior of the Sun and Sun-like Stars, ed. S. Korzennik & A. Wilson (ESA-SP 418; Noordwijk: ESA), 73

Rhodes, E. J., Jr., Reiter, J., Schou, J., Kosovichev, A. G., & Scherrer, P. H. 2001, ApJ, 561, 1127

Ritzwoller, M. H., & Lavely, E. M. 1991, ApJ, 369, 557

Roth, M., & Stix, M. 2008, SoPh, 251, 77

Schad, A., Timmer, J., & Roth, M. 2011, ApJ, 734, 97

Schad, A., Timmer, J., & Roth, M. 2013, ApJL, 778, L38

Scherrer, P. H., Bogart, R. S., Bush, R. I., et al. 1995, SoPh, 162, 129

Scherrer, P. H., Schou, J., Bush, R. I., et al. 2012, SoPh, 275, 207

Schittkowski, K. 1986, Ann. Oper. Res., 5, 485

Schou, J. 1992, Ph.D. Thesis, Aarhus University

Schou, J., Christensen-Dalsgaard, J., & Thompson, M. J. 1992, ApJL, 385, L59

Schou, J., Christensen-Dalsgaard, J., & Thompson, M. J. 1994, ApJ, 433, 389

Schou, J., Howe, R., Basu, S., et al. 2002, ApJ, 567, 1234

Thompson, M. J., Toomre, J., Anderson, E. R., et al. 1996, Science, 272, 1300

Thompson, M. J., Christensen-Dalsgaard, J., Miesch, M. S., et al. 2003, ARA&A, 41, 599

Tomczyk, S. 1988, Ph.D. Thesis, California University, Los Angeles

Vitense, E. 1953, ZA, 32, 135

Vorontsov, S. V., Baturin, V. A., Ayukov, S. V., et al. 2013, Progress in Physics of the Sun and Stars: A New Era in Helio- and Asteroseismology, 19

Woodard, M. F. 1989, ApJ, 347, 1176